



Constraints on the spin-parity and anomalous HVV couplings of the Higgs boson in proton collisions at 7 and 8 TeV

The CMS Collaboration*

Abstract

The study of the spin-parity and tensor structure of the interactions of the recently discovered Higgs boson is performed using the $H \rightarrow ZZ, Z\gamma^*, \gamma^*\gamma^* \rightarrow 4\ell$, $H \rightarrow WW \rightarrow \ell\nu\ell\nu$, and $H \rightarrow \gamma\gamma$ decay modes. The full dataset recorded by the CMS experiment during the LHC Run 1 is used, corresponding to an integrated luminosity of up to 5.1 fb^{-1} at a center-of-mass energy of 7 TeV and up to 19.7 fb^{-1} at 8 TeV. A wide range of spin-two models is excluded at a 99% confidence level or higher, or at a 99.87% confidence level for the minimal gravity-like couplings, regardless of whether assumptions are made on the production mechanism. Any mixed-parity spin-one state is excluded in the ZZ and WW modes at a greater than 99.999% confidence level. Under the hypothesis that the resonance is a spin-zero boson, the tensor structure of the interactions of the Higgs boson with two vector bosons ZZ, Z γ , $\gamma\gamma$, and WW is investigated and limits on eleven anomalous contributions are set. Tighter constraints on anomalous HVV interactions are obtained by combining the HZZ and HWW measurements. All observations are consistent with the expectations for the standard model Higgs boson with the quantum numbers $J^{PC} = 0^{++}$.

Published in Physical Review D as doi:10.1103/PhysRevD.92.012004.

Contents

1	Introduction	2
2	Phenomenology of spin-parity and anomalous HVV interactions	3
2.1	Decay of a spin-zero resonance	3
2.2	Decay of a spin-one resonance	6
2.3	Decay of a spin-two resonance	7
2.4	Production of a resonance	8
3	The CMS detector, simulation, and reconstruction	11
3.1	Monte Carlo simulation	11
3.2	Event reconstruction	12
3.3	Four-lepton event selection	13
3.4	Two-lepton event selection	13
3.5	Two-photon event selection	14
4	Analysis techniques	15
4.1	Observables in the $H \rightarrow VV \rightarrow 4\ell$ analysis	16
4.2	Observables in the $H \rightarrow WW \rightarrow \ell\nu\ell\nu$ analysis	18
4.3	Observables in the matrix element likelihood approach	18
4.4	Maximum likelihood fit with the template method	21
4.5	Analysis validation and systematic uncertainties	25
4.6	Analysis validation with analytic parameterization of kinematic distributions	27
5	Study of exotic spin-one and spin-two scenarios	28
5.1	Exotic-spin study with the $H \rightarrow ZZ \rightarrow 4\ell$ channel	29
5.2	Exotic-spin study with the $H \rightarrow WW \rightarrow \ell\nu\ell\nu$ channel	32
5.3	Combined exotic-spin results with the $H \rightarrow ZZ$ and WW channels	36
5.4	Combined exotic-spin results with the $H \rightarrow ZZ, WW, \text{ and } \gamma\gamma$ channels	39
6	Study of spin-zero HVV couplings	42
6.1	Study of HZZ couplings with the $H \rightarrow ZZ \rightarrow 4\ell$ channel	44
6.2	Validation of the HZZ measurements	48
6.3	Study of $HZ\gamma$ and $H\gamma\gamma$ couplings with the $H \rightarrow VV \rightarrow 4\ell$ channel	49
6.4	Study of HWW couplings with the $H \rightarrow WW \rightarrow \ell\nu\ell\nu$ channel	52
6.5	Combination of HZZ and HWW results	52
7	Summary	56
A	The CMS Collaboration	67

1 Introduction

The observation of a new boson [1–3] with a mass around 125 GeV and properties consistent with the standard model (SM) Higgs boson [4–10] was reported by the ATLAS and CMS Collaborations in 2012. The discovery was followed by a comprehensive set of measurements [11–27] of its properties to determine if the new boson follows the SM predictions or if there are indications for physics beyond the SM (BSM).

The CMS experiment analyzed the full dataset collected during the CERN LHC Run 1 and measured the properties of the Higgs-like boson, H , using its decay modes to two electroweak gauge bosons $H \rightarrow ZZ \rightarrow 4\ell$ [11–13], $H \rightarrow WW \rightarrow \ell\nu\ell\nu$ [14], and $H \rightarrow \gamma\gamma$ [15], where ℓ denotes e^\pm or μ^\pm , and WW denotes W^+W^- . The results showed that the spin-parity properties of the new boson are consistent with the expectations for the scalar SM Higgs boson. In particular, the hypotheses of a pseudoscalar, vector, and pseudovector boson were excluded at a 99.95% confidence level (CL) or higher, and several spin-two boson hypotheses were excluded at a 98% CL or higher. The investigated spin-two models included two bosons with graviton-like interactions and two bosons with higher-dimension operators and opposite parity. The spin-zero results included the first constraint of the f_{a3} parameter, which probes the tensor structure of the HZZ interactions and is defined as the fractional pseudoscalar cross section, with $f_{a3} = 1$ corresponding to the pure pseudoscalar hypothesis. The ATLAS experiment has also excluded at a 98% CL or higher the hypotheses of a pseudoscalar, vector, pseudovector, and graviton-inspired spin-two boson with minimal couplings and several assumptions on the boson production mechanisms [22].

In this paper, an extended study of the spin-parity properties of the Higgs boson and of the tensor structure of its interactions with electroweak gauge bosons is presented using the $H \rightarrow ZZ, Z\gamma^*, \gamma^*\gamma^* \rightarrow 4\ell$, where the interference between the three intermediate states is included, and $H \rightarrow WW \rightarrow \ell\nu\ell\nu$ decay modes at the CMS experiment. The study focuses on testing for the presence of anomalous effects in HZZ and HWW interactions under spin-zero, -one, and -two hypotheses. The $HZ\gamma$ and $H\gamma\gamma$ interactions are probed for the first time using the 4ℓ final state. Constraints are set on eleven anomalous coupling contributions to the HVV interactions, where V is a gauge vector boson, under the spin-zero assumption of the Higgs boson, extending the original measurement of the f_{a3} parameter [11, 12]. The exotic-spin study is extended to the analysis of mixed spin-one states, beyond the pure parity states studied earlier [12, 14], and ten spin-two hypotheses of the boson under the assumption of production either via gluon fusion or quark-antiquark annihilation, or without such an assumption. This corresponds to thirty spin-two models, beyond the six production and decay models studied earlier [11, 12, 14]. The $H \rightarrow \gamma\gamma$ decay channel is also studied in the context of exotic spin-two scenarios, and the results presented in Ref. [15] are combined with those obtained in the $H \rightarrow ZZ$ and $H \rightarrow WW$ channels [12, 14].

The experimental approaches used here are similar to those used by CMS to study the spin-parity and other properties of the new resonance [11–15], and use the techniques developed for such measurements [28–33]. The analysis is based on theoretical and phenomenological studies that describe the couplings of a Higgs-like boson to two gauge bosons. They provide techniques and ideas for measuring the spin and CP properties of a particle interacting with vector bosons [28–57]. Historically, such techniques have been applied to the analysis of meson decays to four-body final states [58–62].

The paper is organized as follows. First, the phenomenology of spin-parity and anomalous HVV interactions is described in Section 2. The experimental apparatus, simulation, and reconstruction techniques are discussed in Section 3. The analysis techniques are introduced

in Section 4. The exclusion of exotic spin-one and spin-two scenarios is shown in Section 5. Finally, for the spin-zero scenario, comprehensive studies of the tensor structure of HVV interactions are presented in Section 6. The results are summarized in Section 7.

2 Phenomenology of spin-parity and anomalous HVV interactions

The production and decay of H is described by its interactions with a pair of vector bosons VV, such as ZZ, Z γ , $\gamma\gamma$, WW, and gg, or with a fermion-antifermion pair. The relevant phenomenology for the interactions of a spin-zero, -one, and -two boson, as motivated by earlier studies [28, 29, 31–33, 53], is presented below. In the following, the spin-parity state is generically denoted as J^P , with $J = 0, 1$, or 2 , while the quantum numbers of the SM Higgs boson are expected to be $J^{PC} = 0^{++}$. However, the interactions of the observed state do not necessarily conserve C-parity or CP-parity, and the general scattering amplitudes describe the spin-parity properties of the new boson and its anomalous couplings with a pair of vector bosons or fermions.

2.1 Decay of a spin-zero resonance

The scattering amplitude describing the interaction between a spin-zero H and two spin-one gauge bosons VV, such as ZZ, Z γ , $\gamma\gamma$, WW, or gg, includes only three independent invariant tensor structures with the coupling parameters a_i^{VV} that can have both real and imaginary parts and in general are form factors which can depend on the squared Lorentz invariant four-momenta of V_1 and V_2 , $q_{V_1}^2$ and $q_{V_2}^2$. In the following, the terms up to q_V^2 are kept in the expansion under the assumption of small contributions from anomalous couplings

$$A(\text{HVV}) \sim \left[a_1^{\text{VV}} + \frac{\kappa_1^{\text{VV}} q_{V_1}^2 + \kappa_2^{\text{VV}} q_{V_2}^2}{(\Lambda_1^{\text{VV}})^2} \right] m_{V_1}^2 \epsilon_{V_1}^* \epsilon_{V_2}^* + a_2^{\text{VV}} f_{\mu\nu}^{*(1)} f^{*(2),\mu\nu} + a_3^{\text{VV}} f_{\mu\nu}^{*(1)} \tilde{f}^{*(2),\mu\nu}, \quad (1)$$

where $f^{(i)\mu\nu} = \epsilon_{V_i}^\mu q_{V_i}^\nu - \epsilon_{V_i}^\nu q_{V_i}^\mu$ is the field strength tensor of a gauge boson with momentum q_{V_i} and polarization vector ϵ_{V_i} , $\tilde{f}_{\mu\nu}^{(i)} = \frac{1}{2} \epsilon_{\mu\nu\rho\sigma} f^{(i),\rho\sigma}$ is the dual field strength tensor, the superscript * designates a complex conjugate, m_{V_1} is the pole mass of the Z or W vector boson, while the cases with the massless vector bosons are discussed below, and Λ_1 is the scale of BSM physics and is a free parameter of the model [31]. A different coupling in the scattering amplitude in Eq. (1) typically leads to changes of both the observed rate and the kinematic distributions of the process. However, the analysis presented in this paper does not rely on any prediction of the overall rate and studies only the relative contributions of different tensor structures.

In Eq. (1), VV stands for ZZ, Z γ , $\gamma\gamma$, WW, and gg. The tree-level SM-like contribution corresponds to $a_1^{\text{ZZ}} \neq 0$ and $a_1^{\text{WW}} \neq 0$, while there is no tree-level coupling to massless gauge bosons, that is $a_1^{\text{VV}} = 0$ for Z γ , $\gamma\gamma$, and gg. Small values of the other couplings can be generated through loop effects in the SM, but their SM values are not accessible experimentally with the available data. Therefore, the other terms can be ascribed to anomalous couplings which are listed for HZZ, HWW, HZ γ , and H $\gamma\gamma$ in Table 1. Among those, considerations of symmetry and gauge invariance require $\kappa_1^{\text{ZZ}} = \kappa_2^{\text{ZZ}} = -\exp(i\phi_{\Lambda_1}^{\text{ZZ}})$, $\kappa_1^{\gamma\gamma} = \kappa_2^{\gamma\gamma} = 0$, $\kappa_1^{\text{gg}} = \kappa_2^{\text{gg}} = 0$, $\kappa_1^{\text{Z}\gamma} = 0$ and $\kappa_2^{\text{Z}\gamma} = -\exp(i\phi_{\Lambda_1}^{\text{Z}\gamma})$. While not strictly required, the same symmetry is considered in the WW case $\kappa_1^{\text{WW}} = \kappa_2^{\text{WW}} = -\exp(i\phi_{\Lambda_1}^{\text{WW}})$. In the above, $\phi_{\Lambda_1}^{\text{VV}}$ is the phase of the anomalous coupling with Λ_1^{VV} , which is either 0 or π for real couplings. In the following, the ZZ labels for the ZZ interactions will be omitted, and therefore the couplings a_1 , a_2 , a_3 , and Λ_1 are not labeled explicitly with a ZZ superscript, while the superscript is kept for the other VV states.

The parity-conserving interaction of a pseudoscalar (CP -odd state) corresponds to the a_3^{VV} terms, while the other terms describe the parity-conserving interaction of a scalar (CP -even state). The a_3^{VV} terms appear in the SM only at a three-loop level and receive a small contribution. The a_2^{VV} and Λ_1^{VV} terms appear in loop-induced processes and give small contributions $O(10^{-3}-10^{-2})$. The dominant contributions to the SM expectation of the $H \rightarrow Z\gamma$ and $\gamma\gamma$ decays are $a_2^{Z\gamma}$ and $a_2^{\gamma\gamma}$, which are predicted to be $a_2^{Z\gamma} \simeq -0.007$ and $a_2^{\gamma\gamma} \simeq 0.004$ [63]. The $a_i^{Z\gamma}$ and $a_i^{\gamma\gamma}$ coupling terms contribute to the $H \rightarrow 4\ell$ process through the $H \rightarrow Z\gamma^*$ and $\gamma^*\gamma^* \rightarrow 4\ell$ decays with off-shell intermediate photons. Anomalous couplings may be enhanced with BSM contributions and generally acquire a non-trivial dependence on Lorentz invariant quantities and become complex. The different contributions to the amplitude can therefore be tested without making assumptions about the complex phase between different contributions. When the particles in the loops responsible for these couplings are heavy in comparison to the Higgs boson mass parameters, the couplings are real.

Under the assumption that the couplings are constant and real, the above formulation is equivalent to an effective Lagrangian notation for the HZZ, HWW, HZ γ , and H $\gamma\gamma$ interactions

$$\begin{aligned}
L(\text{HVV}) \sim & a_1 \frac{m_Z^2}{2} \text{HZ}^\mu Z_\mu - \frac{\kappa_1}{(\Lambda_1)^2} m_Z^2 \text{HZ}_\mu \square Z^\mu - \frac{1}{2} a_2 \text{HZ}^{\mu\nu} Z_{\mu\nu} - \frac{1}{2} a_3 \text{HZ}^{\mu\nu} \tilde{Z}_{\mu\nu} \\
& + a_1^{\text{WW}} m_W^2 \text{HW}^{+\mu} W_\mu^- - \frac{1}{(\Lambda_1^{\text{WW}})^2} m_W^2 \text{H} \left(\kappa_1^{\text{WW}} W_\mu^- \square W^{+\mu} + \kappa_2^{\text{WW}} W_\mu^+ \square W^{-\mu} \right) \\
& - a_2^{\text{WW}} \text{HW}^{+\mu\nu} W_{\mu\nu}^- - a_3^{\text{WW}} \text{HW}^{+\mu\nu} \tilde{W}_{\mu\nu}^- \\
& + \frac{\kappa_2^{Z\gamma}}{(\Lambda_1^{Z\gamma})^2} m_Z^2 \text{HZ}_\mu \partial_\nu F^{\mu\nu} - a_2^{Z\gamma} \text{HF}^{\mu\nu} Z_{\mu\nu} - a_3^{Z\gamma} \text{HF}^{\mu\nu} \tilde{Z}_{\mu\nu} - \frac{1}{2} a_2^{\gamma\gamma} \text{HF}^{\mu\nu} F_{\mu\nu} - \frac{1}{2} a_3^{\gamma\gamma} \text{HF}^{\mu\nu} \tilde{F}_{\mu\nu}, \quad (2)
\end{aligned}$$

where the notations are the same as in Eq. (1) and H is the real Higgs field, Z_μ is the Z field, W_μ is the W field, F_μ is the γ^* field, $V_{\mu\nu} = \partial_\mu V_\nu - \partial_\nu V_\mu$ is the bosonic field strength, the dual field strengths are defined as $\tilde{V}_{\mu\nu} = \frac{1}{2} \epsilon_{\mu\nu\rho\sigma} V^{\rho\sigma}$, and \square is the D'Alembert operator. The SM-like terms with tree-level couplings a_1 and a_1^{WW} are associated with dimension-three operators, and the rest of the terms tested correspond to operators of dimension five. Operators of higher dimension are neglected in this study.

In the analysis, the physics effects of the eleven anomalous couplings listed in Table 1 are described, where the hypothesis of the Higgs boson mass $m_H = 125.6 \text{ GeV}$ is used, which is the best-fit value in the study of the $H \rightarrow VV \rightarrow 4\ell$ and $H \rightarrow WW \rightarrow \ell\nu\ell\nu$ channels [12, 14]. The scenarios are parameterized in terms of the effective fractional cross sections f_{ai} and their phases ϕ_{ai} with respect to the two dominant tree-level couplings a_1 and a_1^{WW} in the $H \rightarrow VV \rightarrow 4\ell$ and $H \rightarrow WW \rightarrow \ell\nu\ell\nu$ processes, respectively. In the $H \rightarrow VV$ decay the q_V^2 range does not exceed approximately 100 GeV due to the kinematic bound, supporting the expansion up to q_V^2 in Eq. (1). Even though the expansion with only three anomalous contributions in Eq. (1) may become formally incomplete when large values of $f_{ai} \sim 1$ are considered, this remains a valuable test of the consistency of the data with the SM. Moreover, certain models, such as models with a pseudoscalar Higgs boson state, do not require sizable contribution of higher terms in the q_V^2 expansion even for $f_{ai} \sim 1$. Therefore, the full range $0 \leq f_{ai} \leq 1$ is considered in this study.

Table 1: List of anomalous HVV couplings considered in the measurements assuming a spin-zero Higgs boson. The definition of the effective fractions is discussed in the text and the translation constant is given in each case. The effective cross sections correspond to the processes $H \rightarrow VV \rightarrow 2e2\mu$ and $H \rightarrow WW \rightarrow \ell\nu\ell\nu$ and the Higgs boson mass $m_H = 125.6$ GeV using the JHUGEN [28, 29, 31] calculation. The cross-section ratios for the $HZ\gamma$ and $H\gamma\gamma$ couplings include the requirement $\sqrt{q_{V_i}^2} \geq 4$ GeV.

Interaction	Anomalous Coupling	Coupling Phase	Effective Fraction	Translation Constant
HZZ	Λ_1	$\phi_{\Lambda 1}$	$f_{\Lambda 1}$	$\sigma_1 / \tilde{\sigma}_{\Lambda 1} = 1.45 \times 10^4 \text{ TeV}^{-4}$
	a_2	$\phi_{a 2}$	$f_{a 2}$	$\sigma_1 / \sigma_2 = 2.68$
	a_3	$\phi_{a 3}$	$f_{a 3}$	$\sigma_1 / \sigma_3 = 6.36$
HWW	Λ_1^{WW}	$\phi_{\Lambda 1}^{WW}$	$f_{\Lambda 1}^{WW}$	$\sigma_1^{WW} / \tilde{\sigma}_{\Lambda 1}^{WW} = 1.87 \times 10^4 \text{ TeV}^{-4}$
	a_2^{WW}	$\phi_{a 2}^{WW}$	$f_{a 2}^{WW}$	$\sigma_1^{WW} / \sigma_2^{WW} = 1.25$
	a_3^{WW}	$\phi_{a 3}^{WW}$	$f_{a 3}^{WW}$	$\sigma_1^{WW} / \sigma_3^{WW} = 3.01$
HZ γ	$\Lambda_1^{Z\gamma}$	$\phi_{\Lambda 1}^{Z\gamma}$	$f_{\Lambda 1}^{Z\gamma}$	$\sigma'_1 / \tilde{\sigma}_{\Lambda 1}^{Z\gamma} = 5.76 \times 10^3 \text{ TeV}^{-4}$
	$a_2^{Z\gamma}$	$\phi_{a 2}^{Z\gamma}$	$f_{a 2}^{Z\gamma}$	$\sigma'_1 / \sigma_2^{Z\gamma} = 2.24 \times 10^{-3}$
	$a_3^{Z\gamma}$	$\phi_{a 3}^{Z\gamma}$	$f_{a 3}^{Z\gamma}$	$\sigma'_1 / \sigma_3^{Z\gamma} = 2.72 \times 10^{-3}$
H $\gamma\gamma$	$a_2^{\gamma\gamma}$	$\phi_{a 2}^{\gamma\gamma}$	$f_{a 2}^{\gamma\gamma}$	$\sigma'_1 / \sigma_2^{\gamma\gamma} = 2.82 \times 10^{-3}$
	$a_3^{\gamma\gamma}$	$\phi_{a 3}^{\gamma\gamma}$	$f_{a 3}^{\gamma\gamma}$	$\sigma'_1 / \sigma_3^{\gamma\gamma} = 2.88 \times 10^{-3}$

The effective fractional ZZ cross sections f_{ai} and phases ϕ_{ai} are defined as follows

$$\begin{aligned}
 f_{\Lambda 1} &= \frac{\tilde{\sigma}_{\Lambda 1} / (\Lambda_1)^4}{|a_1|^2 \sigma_1 + |a_2|^2 \sigma_2 + |a_3|^2 \sigma_3 + \tilde{\sigma}_{\Lambda 1} / (\Lambda_1)^4 + \dots}, & \phi_{\Lambda 1}, \\
 f_{a 2} &= \frac{|a_2|^2 \sigma_2}{|a_1|^2 \sigma_1 + |a_2|^2 \sigma_2 + |a_3|^2 \sigma_3 + \tilde{\sigma}_{\Lambda 1} / (\Lambda_1)^4 + \dots}, & \phi_{a 2} = \arg \left(\frac{a_2}{a_1} \right), \\
 f_{a 3} &= \frac{|a_3|^2 \sigma_3}{|a_1|^2 \sigma_1 + |a_2|^2 \sigma_2 + |a_3|^2 \sigma_3 + \tilde{\sigma}_{\Lambda 1} / (\Lambda_1)^4 + \dots}, & \phi_{a 3} = \arg \left(\frac{a_3}{a_1} \right),
 \end{aligned} \tag{3}$$

where σ_i is the cross section of the process corresponding to $a_i = 1, a_{j \neq i} = 0$, while $\tilde{\sigma}_{\Lambda 1}$ is the effective cross section of the process corresponding to $\Lambda_1 = 1$ TeV, given in units of $\text{fb} \cdot \text{TeV}^4$. The effective fractional WW cross sections are defined in complete analogy with the definitions for ZZ as shown in Eq. (3). The definition in Eq. (3) is independent of the collider energy because only the decay rates of the processes $H \rightarrow VV \rightarrow 4\ell$ and $H \rightarrow WW \rightarrow \ell\nu\ell\nu$ affect the ratio. It also has the advantage of the f_{ai} parameters being bounded between 0 and 1, and being uniquely defined, regardless of the convention used for the coupling constants. In the four-lepton final state, the cross section of the $H \rightarrow VV \rightarrow 2e2\mu$ final state is used, as this final state is not affected by the interference between same-flavor leptons in the final state.

In an analogous way, the effective fractional cross sections and phases of $Z\gamma$ and $\gamma\gamma$, generically denoted as $V\gamma$ below, in the $H \rightarrow VV \rightarrow 2e2\mu$ process are defined as

$$f_{ai}^{V\gamma} = \frac{|a_i^{V\gamma}|^2 \sigma_i^{V\gamma}}{|a_1|^2 \sigma_1' + |a_i^{V\gamma}|^2 \sigma_i^{V\gamma} + \dots}, \quad \phi_{ai}^{V\gamma} = \arg \left(\frac{a_{ai}^{V\gamma}}{a_1} \right), \tag{4}$$

where the requirement $\sqrt{q_{V_i}^2} \geq 4$ GeV is used in the cross-section calculations for all processes,

including the ZZ tree-level process with a_1 as indicated with σ_1' . This requirement on $q_{V_i}^2$ is introduced to restrict the definition to a region without infrared divergence and to define the fractions within the empirically relevant range. The ellipsis (...) in Eqs. (3) and (4) indicates any other contribution not listed explicitly.

Given the measured values of the effective fractions, it is possible to extract the ratios of the coupling constants a_i/a_1 , the scale of BSM physics Λ_1 , or the ratios of the $Z\gamma^*$ ($\gamma^*\gamma^*$) cross sections with respect to the SM predictions in any parameterization. Following Eq. (1) the translation of the f_{ai} measurements can be performed as

$$\frac{|a_i|}{|a_1|} = \sqrt{f_{ai}/f_{a1}} \times \sqrt{\sigma_1/\sigma_i}, \quad \Lambda_1 \sqrt{|a_1|} = \sqrt[4]{f_{a1}/f_{\Lambda 1}} \times \sqrt[4]{\tilde{\sigma}_{\Lambda 1}/\sigma_1}, \quad (5)$$

where the cross-section ratios for a 125.6 GeV Higgs boson are given in Table 1, and the fraction $f_{a1} = (1 - f_{\Lambda 1} - f_{a2} - f_{a3} - \dots)$ corresponds to the effective SM tree-level contribution, which is expected to dominate. The ellipsis in the f_{a1} definition indicates any other contribution, such as $Z\gamma^*$ and $\gamma^*\gamma^*$, where relevant.

The couplings of the Higgs boson to $Z\gamma$ and $\gamma\gamma$ are generally much better measured in the decays with the on-shell gauge bosons $H \rightarrow Z\gamma$ and $\gamma\gamma$ [15, 19, 23, 25]. Therefore, the measurements of the $HZ\gamma$ and $H\gamma\gamma$ anomalous couplings are provided mostly as a feasibility study without going into detailed measurements of correlations of parameters. Once a sufficient number of events is accumulated for the discovery of these modes in the $H \rightarrow VV \rightarrow 4\ell$ channel with a high-luminosity LHC, the study of CP properties can be performed with the $HZ\gamma$ and $H\gamma\gamma$ couplings [56, 64].

The couplings of a spin-zero particle to W and Z bosons can be related given the assumption of certain symmetries. For example, in the case of the custodial singlet Higgs boson, the relation is $a_1^{WW} = a_1$ [65, 66]. Generally, these couplings could have a different relationship and the HVV couplings are controlled by two free parameters. When one parameter is expressed as the f_{ai} fraction in the HZZ coupling, the other parameter can be chosen as a ratio of anomalous couplings in the $H \rightarrow ZZ$ and $H \rightarrow WW$ channels

$$r_{ai} = \frac{a_i^{WW}/a_1^{WW}}{a_i/a_1}, \quad \text{or } R_{ai} = \frac{r_{ai}|r_{ai}|}{1 + r_{ai}^2}. \quad (6)$$

Using Eq. (5) the effective fractions f_{ai}^{WW} and f_{ai} can be related as

$$f_{ai} = \left[1 + r_{ai}^2 (1/f_{ai}^{WW} - 1) \sigma_i^{WW} \sigma_1 / (\sigma_1^{WW} \sigma_i) \right]^{-1}. \quad (7)$$

In this way, the measurement of f_{ai}^{WW} can be converted to f_{ai} and vice versa, and the combination of the results in the ZZ and WW channels can be achieved.

2.2 Decay of a spin-one resonance

In the case of a spin-one resonance, the amplitude of its interaction with a pair of massive gauge bosons, ZZ or WW, consists of two independent terms, which can be written as

$$A(X_{J=1}VV) \sim b_1^{VV} [(\epsilon_{V1}^* q) (\epsilon_{V2}^* \epsilon_X) + (\epsilon_{V2}^* q) (\epsilon_{V1}^* \epsilon_X)] + b_2^{VV} \epsilon_{\alpha\mu\nu\beta} \epsilon_X^\alpha \epsilon_{V1}^{*\mu} \epsilon_{V2}^{*\nu} \tilde{q}^\beta, \quad (8)$$

where ϵ_X is the polarization vector of the boson X with spin one, $q = q_{V1} + q_{V2}$ and $\tilde{q} = q_{V1} - q_{V2}$ [28, 29]. Here the $b_1^{VV} \neq 0$ coupling corresponds to a vector particle, while the $b_2^{VV} \neq 0$ coupling corresponds to a pseudovector. The $Z\gamma$ interactions of the spin-one particle are not

considered, while the $\gamma\gamma$ and gg interactions are forbidden by the Landau-Yang theorem [67, 68], where the gg case is justified by the assumption that the state X is color-neutral. Here, and throughout this paper, a boson with an exotic spin is denoted as X to distinguish it from a spin-zero Higgs boson H .

Similarly, the lowest order terms in the scattering amplitudes can be mapped to the corresponding terms in the effective Lagrangian

$$L(X_{J=1}VV) \sim b_1 \partial_\mu X_\nu Z^\mu Z^\nu + b_2 \epsilon_{\alpha\mu\nu\beta} X^\alpha Z^\mu \partial^\beta Z^\nu + b_1^{WW} \partial_\mu X_\nu (W^{+\mu} W^{-\nu} + W^{-\mu} W^{+\nu}) + b_2^{WW} \epsilon_{\alpha\mu\nu\beta} X^\alpha (W^{-\mu} \partial^\beta W^{+\nu} + W^{+\mu} \partial^\beta W^{-\nu}). \quad (9)$$

Despite the fact that the experimental observation [1–3] of the $H \rightarrow \gamma\gamma$ decay channel prevents the observed boson from being a spin-one particle, it is still important to experimentally study the spin-one models in the decay to massive vector bosons in case that the observed state is a different one. The CMS and ATLAS experiments have already tested the compatibility of the observed boson with the $J^P = 1^+$ and 1^- hypotheses [12, 22], where CMS has tested this using both production-independent and production-dependent methods. The compatibility of the data with the hypothesis of the boson being a mixture of the 1^+ and 1^- states is now tested allowing for the presence of each of the terms in the scattering amplitude in Eq. (8). A continuous parameter that uniquely describes the presence of the corresponding terms b_1^{VV} and b_2^{VV} is defined as an effective fractional cross section

$$f_{b_2}^{VV} = \frac{|b_2^{VV}|^2 \sigma_{b_2}}{|b_1^{VV}|^2 \sigma_{b_1} + |b_2^{VV}|^2 \sigma_{b_2}}, \quad (10)$$

where σ_{b_i} is the cross section of the process corresponding to $b_i^{VV} = 1, b_{j \neq i}^{VV} = 0$ in the $X \rightarrow ZZ \rightarrow 2e2\mu$ or $WW \rightarrow \ell\nu\ell\nu$ final state and $\sigma_{b_1} = \sigma_{b_2}$. This effective fraction is used in the analysis to test if the data favor the SM Higgs boson scalar hypothesis or some particular mixture of the vector and pseudovector states.

2.3 Decay of a spin-two resonance

In the case of a general spin-two resonance, its decay to a pair of massive vector bosons, ZZ or WW , is considered in their sequential decay to four leptons, but not with $Z\gamma^*$ and $\gamma^*\gamma^*$, as those are generally suppressed by the $\gamma^* \rightarrow \ell^+\ell^-$ selection. The decay to two on-shell photons $X \rightarrow \gamma\gamma$ is also considered. The corresponding XVV amplitude is used to describe the $X \rightarrow ZZ$ and WW , as well as $gg \rightarrow X$, processes

$$A(X_{J=2}VV) \sim \Lambda^{-1} \left[2c_1^{VV} t_{\mu\nu} f^{*1,\mu\alpha} f^{*2,\nu}_\alpha + 2c_2^{VV} t_{\mu\nu} \frac{q_\alpha q_\beta}{\Lambda^2} f^{*1,\mu\alpha} f^{*2,\nu\beta} + c_3^{VV} t_{\beta\nu} \frac{\tilde{q}^\beta \tilde{q}^\alpha}{\Lambda^2} (f^{*1,\mu\nu} f_{\mu\alpha}^{*2} + f^{*2,\mu\nu} f_{\mu\alpha}^{*1}) + c_4^{VV} t_{\mu\nu} \frac{\tilde{q}^\nu \tilde{q}^\mu}{\Lambda^2} f^{*1,\alpha\beta} f_{\alpha\beta}^{*2} + m_V^2 \left(2c_5^{VV} t_{\mu\nu} \epsilon_{V1}^{*\mu} \epsilon_{V2}^{*\nu} + 2c_6^{VV} t_{\mu\nu} \frac{\tilde{q}^\mu q_\alpha}{\Lambda^2} (\epsilon_{V1}^{*\nu} \epsilon_{V2}^{*\alpha} - \epsilon_{V1}^{*\alpha} \epsilon_{V2}^{*\nu}) + c_7^{VV} t_{\mu\nu} \frac{\tilde{q}^\mu \tilde{q}^\nu}{\Lambda^2} \epsilon_{V1}^{*\mu} \epsilon_{V2}^{*\nu} \right) + c_8^{VV} t_{\mu\nu} \frac{\tilde{q}^\mu \tilde{q}^\nu}{\Lambda^2} f^{*1,\alpha\beta} \tilde{f}_{\alpha\beta}^{*2} + m_V^2 \left(c_9^{VV} t^{\mu\alpha} \frac{\tilde{q}_\alpha \epsilon_{\mu\nu\rho\sigma} \epsilon_{V1}^{*\nu} \epsilon_{V2}^{*\rho} q^\sigma}{\Lambda^2} + c_{10}^{VV} t^{\mu\alpha} \frac{\tilde{q}_\alpha \epsilon_{\mu\nu\rho\sigma} q^\rho \tilde{q}^\sigma}{\Lambda^4} (\epsilon_{V1}^{*\nu} (q \epsilon_{V2}^{*\nu}) + \epsilon_{V2}^{*\nu} (q \epsilon_{V1}^{*\nu})) \right) \right], \quad (11)$$

where $t^{\mu\nu}$ is the wavefunction of a spin-two particle X given by a symmetric traceless tensor, m_V is the mass of the considered gauge boson, and Λ is the scale of BSM physics [28, 29]. The couplings c_1^{VV} and c_5^{VV} correspond to the parity-conserving interaction of a spin-two tensor with minimal gravity-like couplings. As in the spin-zero case, the couplings c_i^{VV} are in general momentum-dependent form factors. In this analysis it is assumed that the form factors are momentum-independent constants and, thus, only the lowest q_i^2 order terms in the scattering amplitude are considered.

The terms in Eq. (11) can be mapped to the corresponding terms (operators up to dimension seven) in the effective Lagrangian

$$\begin{aligned}
L(X_{J=2}ZZ) \sim \Lambda^{-1} & \left(-c_1 X_{\mu\nu} Z^{\mu\alpha} Z^\nu{}_\alpha + \frac{c_2}{\Lambda^2} (\partial_\alpha \partial_\beta X_{\mu\nu}) Z^{\mu\alpha} Z^{\nu\beta} + \frac{c_3}{\Lambda^2} X_{\beta\nu} [\partial^\alpha, [\partial^\beta, Z^{\mu\nu}]] Z_{\mu\alpha} \right. \\
& + \frac{c_4}{2\Lambda^2} X_{\mu\nu} [\partial^\mu, [\partial^\nu, Z^{\alpha\beta}]] Z_{\alpha\beta} + c_5 m_Z^2 X_{\mu\nu} Z^\mu Z^\nu + \frac{2c_6 m_Z^2}{\Lambda^2} \partial_\alpha X_{\mu\nu} [\partial^\mu, Z^\nu] Z^\alpha \\
& - \frac{c_7 m_Z^2}{2\Lambda^2} X_{\mu\nu} [\partial^\mu, [\partial^\nu, Z_\alpha]] Z^\alpha + \frac{c_8}{2\Lambda^2} X_{\mu\nu} [\partial^\mu, [\partial^\nu, Z^{\alpha\beta}]] \tilde{Z}_{\alpha\beta} \\
& \left. - \frac{c_9 m_Z^2}{\Lambda^2} \epsilon_{\mu\nu\rho\sigma} \partial^\sigma X^{\mu\alpha} Z_\nu \partial_\alpha Z^\rho + \frac{c_{10} m_Z^2}{\Lambda^4} \epsilon_{\mu\nu\rho\sigma} \partial^\rho \partial^\beta X^{\mu\alpha} [\partial^\sigma, [\partial_\alpha, Z^\nu]] Z_\beta \right). \quad (12)
\end{aligned}$$

The study of a subset of these ten terms in $X \rightarrow ZZ$, WW , and $\gamma\gamma$ decays and $gg \rightarrow X$ production has already been performed by the CMS and ATLAS experiments [11, 12, 14, 15, 22]. In this analysis the study of spin-two hypotheses is completed by considering the remaining terms in the spin-two VV scattering amplitude in Eq. (11) and different production scenarios. Ten spin-two scenarios are listed in Table 2. Both $q\bar{q}$ production, discussed in Section 2.4, and gluon fusion, described by Eq. (11), of a spin-two state are considered. In the $X \rightarrow \gamma\gamma$ decay channel, the full list of models is not analyzed.

The spin-two model with minimal couplings, which is common to $X \rightarrow ZZ$, WW , and $\gamma\gamma$, represents a massive graviton-like boson as suggested in models with warped extra dimensions (ED) [69, 70]. The individual results for the 2_m^+ model were presented for the $X \rightarrow ZZ$, WW , and $\gamma\gamma$ decays earlier [12, 14, 15]. A combination is reported here.

A modified minimal coupling model 2_b^+ is also considered, where the SM fields are allowed to propagate in the bulk of the ED [71], corresponding to $c_1^{\text{VV}} \ll c_5^{\text{VV}}$ in the XZZ or XWW couplings only. Moreover, eight spin-two models with higher-dimension operators are considered for the XZZ and XWW couplings. The above list of ten spin-two decay models and several production mechanisms does not exhaust all the possible scenarios with mixed amplitudes, but it does provide a comprehensive sample of spin-two alternatives to test the validity of the SM-like $J^P = 0^+$ hypothesis.

2.4 Production of a resonance

While the above discussion of Eqs. (1), (8), and (11) is focussed on the decay $H \rightarrow VV$, these amplitudes also describe production of a resonance via gluon fusion, weak vector boson fusion (VBF) with associated jets, or associated production with a weak vector boson VH. All these mechanisms, along with the $t\bar{t}H$ production, are considered in the analysis of the spin-zero hypothesis of the H boson, where the gluon fusion production dominates. It is possible to study HVV interactions using the kinematics of particles produced in association with the Higgs boson, such as VBF jets or vector boson daughters in VH production. While the q_V^2 range in the $H \rightarrow VV$ process does not exceed approximately 100 GeV due to the kinematic bound, in the associated production no such bound exists, and therefore consideration of more restricted

Table 2: List of spin-two models with the production and decay couplings of an exotic X particle. The subscripts m (minimal couplings), h (couplings with higher-dimension operators), and b (bulk) distinguish different scenarios.

J^P Model	$gg \rightarrow X$ Couplings	$q\bar{q} \rightarrow X$ Couplings	$X \rightarrow VV$ Couplings
2_m^+	$c_1^{gg} \neq 0$	$\rho_1 \neq 0$	$c_1^{VV} = c_5^{VV} \neq 0$
2_{h2}^+	$c_2^{gg} \neq 0$	$\rho_1 \neq 0$	$c_2^{VV} \neq 0$
2_{h3}^+	$c_3^{gg} \neq 0$	$\rho_1 \neq 0$	$c_3^{VV} \neq 0$
2_h^+	$c_4^{gg} \neq 0$	$\rho_1 \neq 0$	$c_4^{VV} \neq 0$
2_b^+	$c_1^{gg} \neq 0$	$\rho_1 \neq 0$	$c_1^{VV} \ll c_5^{VV} \neq 0$
2_{h6}^+	$c_1^{gg} \neq 0$	$\rho_1 \neq 0$	$c_6^{VV} \neq 0$
2_{h7}^+	$c_1^{gg} \neq 0$	$\rho_1 \neq 0$	$c_7^{VV} \neq 0$
2_h^-	$c_8^{gg} \neq 0$	$\rho_2 \neq 0$	$c_8^{VV} \neq 0$
2_{h9}^-	$c_8^{gg} \neq 0$	$\rho_2 \neq 0$	$c_9^{VV} \neq 0$
2_{h10}^-	$c_8^{gg} \neq 0$	$\rho_2 \neq 0$	$c_{10}^{VV} \neq 0$

ranges of q_V^2 might be required [31], bringing an additional uncertainty to such a study. Instead, the analysis presented here is designed to minimize the dependence on the production mechanism focusing on the study of the $H \rightarrow VV$ decay kinematics. In the case of a spin-zero particle, there is no spin correlation between the production process and decay, which allows for production-independent studies. In the case of a non-zero spin particle, it is possible to study decay information only without dependence on the polarization of the resonance, and therefore without dependence on the production mechanism.

The production of on-shell Higgs boson is considered in this analysis. In gluon fusion, about 10% of $H \rightarrow ZZ$ and $H \rightarrow WW$ events are produced off-shell, with a Higgs boson invariant mass above 150 GeV [72]. A similar effect appears in VBF production [13], while it is further suppressed for other production mechanisms. However, this off-shell contribution depends on the width of the Higgs boson [73]. A relative enhancement of the off-shell with respect to the on-shell production is expected in models with anomalous HVV couplings [13, 57]. Therefore, it is possible to study anomalous HVV interactions using the kinematics of the Higgs boson produced off-shell, including relative off-shell enhancement. However, such a study requires additional assumptions about the width of the Higgs boson, its production mechanisms, and the extrapolation of the coupling constants in Eqs. (1), (8), and (11) to q_H^2 values significantly larger than 100 GeV. Therefore, the study of anomalous HVV couplings with the off-shell Higgs boson is left for a future work. Instead, the $H \rightarrow ZZ$ events with an invariant ZZ mass above 140 GeV are not considered, effectively removing off-shell effects and associated model dependence. In the $H \rightarrow WW$ analysis, the event selection discussed below reduces the off-shell contribution to less than 2%. Even though this contribution may increase with anomalous HVV couplings, no such enhancement has been observed in the $H \rightarrow ZZ$ study [13], which limits it to be less than five times the SM expectation at a 95% CL. This constraint is expected to be further improved with more data and additional final states studied. In the present analysis, any off-shell contribution in the study of the on-shell production and $H \rightarrow WW$ decay is neglected.

Since the production of a color-neutral spin-one resonance is forbidden in gluon fusion, its dominant production mechanism is expected to be quark-antiquark annihilation. The production mechanisms of a spin-two boson are expected to be gluon fusion and quark-antiquark annihilation, as for example in the ED models in Refs. [69–71]. While gluon fusion is expected to dominate over the $q\bar{q}$ production of a spin-two state, the latter is a possibility in the effective scattering amplitude with form factors. Therefore, the $q\bar{q} \rightarrow X$ production of both spin-one and

spin-two resonances and the $gg \rightarrow X$ production of a spin-two resonance are considered. The fractional contribution of the $q\bar{q}$ process to the production of a spin-two resonance is denoted as $f(q\bar{q})$, and can be interpreted as the fraction of events produced with $J_z = \pm 1$. For both spin-one and spin-two states, the analysis of the $X \rightarrow ZZ \rightarrow 4\ell$ decay mode is also performed without dependence on the production mechanism, allowing coverage of other mechanisms including associated production.

For the analysis of the $q\bar{q} \rightarrow X$ production, the general scattering amplitudes are considered for the interaction of the spin-one and spin-two bosons with fermions

$$A(X_{J=1}f\bar{f}) = \epsilon_X^\mu \bar{u}_2 \left(\gamma_\mu (\rho_1 + \rho_2 \gamma_5) + \frac{m_f \tilde{q}_\mu}{\Lambda^2} (\rho_3 + \rho_4 \gamma_5) \right) u_1, \quad (13)$$

$$A(X_{J=2}f\bar{f}) = \frac{1}{\Lambda} t^{\mu\nu} \bar{u}_2 \left(\gamma_\mu \tilde{q}_\nu (\rho_1 + \rho_2 \gamma_5) + \frac{m_f \tilde{q}_\mu \tilde{q}_\nu}{\Lambda^2} (\rho_3 + \rho_4 \gamma_5) \right) u_1, \quad (14)$$

where m_f is the fermion mass, u_i is the Dirac spinor, and Λ is the scale of BSM physics [28, 29]. The couplings ρ_i are assumed to be the same for all quark flavors. This assumption, along with the choice of ρ_i couplings in general, has little effect on the analysis since this affects only the expected longitudinal boost of the resonance from different mixtures of parton production processes without affecting its polarization, whose projection on the parton collision axis is always $J_z = \pm 1$, since the ρ_3 and ρ_4 terms are suppressed in the annihilation of light quarks. Therefore, $q\bar{q}$ production leads to a resonance with polarization $J_z = \pm 1$ along the parton collision axis, while gluon fusion leads to $J_z = 0$ or ± 2 . In the case of minimal c_1^{gg} coupling, only $J_z = \pm 2$ is possible. The terms proportional to m_V^2 in Eq. (11) are absent for couplings to massless vector bosons, either $gg \rightarrow X$ in production or $X \rightarrow \gamma\gamma$ in decay. Therefore, the list of models in Table 2 covers ten decay couplings to massive vector bosons but only five couplings for the massless gluons.

The presence of an additional resonance can be inferred from the kinematics of the decay products when separation in invariant mass alone is not sufficient. For example, composite particles can have multiple narrow states with different spin-parity quantum numbers and nearly degenerate masses. Some examples of this phenomenon include ortho/para-positronia, χ_b and χ_c particles where the mass splitting between the different J^P states is orders of magnitude smaller than their mass [74–76].

In an approach common to both the spin-one and spin-two scenarios, the production of a second resonance with different J^P quantum numbers but close in mass to the SM Higgs-like state can be probed. The two states are assumed to be sufficiently separated in mass or produced by different mechanisms, so that they do not interfere, but still to be closer than the experimental mass resolution

$$\Gamma_{J^P} \text{ and } \Gamma_{0^+} \ll |m_{J^P} - m_{0^+}| \ll \delta_m \sim 1 \text{ GeV}. \quad (15)$$

The fractional cross section $f(J^P)$ is defined as follows

$$f(J^P) = \frac{\sigma_{J^P}}{\sigma_{0^+} + \sigma_{J^P}}, \quad (16)$$

where σ_{J^P} (σ_{0^+}) is the cross section of the process corresponding to the J^P (0^+) model defined at the LHC energy of 8 TeV and, in the case of the ZZ channel, for the $X \rightarrow ZZ \rightarrow 2e2\mu$ decay mode. In this case the notation J^P refers to a model name and in practice should reflect all relevant model properties, including spin, parity, production, and decay modes. It should be

noted that the effective fractions f_{ai} and $f(J^P)$ have a distinct nature. The fractions f_{ai} denote the effective fractions related to the corresponding a_i terms within the scattering amplitude of a given state, and are used in measurements that consider interference effects between different parts of the amplitude.

3 The CMS detector, simulation, and reconstruction

The central feature of the CMS apparatus is a superconducting solenoid of 6 m internal diameter, providing a magnetic field of 3.8 T. Within the superconducting solenoid volume are a silicon pixel and strip tracker, a lead tungstate crystal electromagnetic calorimeter (ECAL), and a brass/scintillator hadron calorimeter, each composed of a barrel and two endcap sections. Muons are measured in gas-ionization detectors embedded in the steel flux-return yoke outside the solenoid. Extensive forward calorimetry complements the coverage provided by the barrel and endcap detectors. A more detailed description of the CMS detector, together with a definition of the coordinate system used and the relevant kinematic variables, can be found in Ref. [77].

The data samples used in this analysis are the same as those described in Refs. [12–15], corresponding to an integrated luminosity of 5.1,(4.9) fb⁻¹ collected in 2011 at a center-of-mass energy of 7 TeV and 19.7(19.4) fb⁻¹ in 2012 at 8 TeV in the case of the $H \rightarrow VV \rightarrow 4\ell$ and $H \rightarrow \gamma\gamma$ ($H \rightarrow WW \rightarrow \ell\nu\ell\nu$) channels. The integrated luminosity is measured using data from the CMS hadron forward calorimeter system and the pixel detector [78, 79]. The uncertainties in the integrated luminosity measurement are 2.2% and 2.6% in the 2011 and 2012 datasets, respectively.

3.1 Monte Carlo simulation

The simulation of the signal process is essential for the study of anomalous couplings in HVV interactions, and all the relevant Monte Carlo (MC) samples are generated following the description in Section 2. A dedicated simulation program, JHUGEN 4.8.1 [28, 29, 31], is used to describe anomalous couplings in the production and decay to two vector bosons of spin-zero, spin-one, and spin-two resonances in hadron-hadron collisions, including all the models listed in Tables 1 and 2. For the spin-zero and spin-one studies, interference effects are included by generating mixed samples produced with either of the different tensor structures shown in Eqs. (1) and (8).

For gluon fusion production of a spin-zero state, the kinematics of the Higgs boson decay products and of an associated jet are not affected by the anomalous Hgg interactions, and therefore the next-to-leading-order (NLO) QCD effects are introduced in production with the SM couplings through the POWHEG [80–82] event generator. It is also found that the NLO QCD effects that are relevant for the analysis of a spin-zero state are well approximated with the combination of leading-order (LO) QCD matrix elements and parton showering [31]. Therefore, JHUGEN at LO QCD is adopted for the simulation of anomalous interactions in all the other production processes where it is important to model the correlations between production and the kinematics of the final-state particles, such as in VBF and VH production of a spin-zero state, $q\bar{q} \rightarrow X$ production of a spin-one state, and $q\bar{q}$ and $gg \rightarrow X$ production of a spin-two state. In the case of a spin-two X boson, the LO QCD modeling of production avoids potentially problematic p_T spectrum of the X boson appearing at NLO with non-universal $Xq\bar{q}$ and Xgg couplings [54] allowed in this study. In all cases, the decays $H/X \rightarrow ZZ / Z\gamma^* / \gamma^*\gamma^* \rightarrow 4\ell$, $H/X \rightarrow WW \rightarrow \ell\nu\ell\nu$, and $H/X \rightarrow \gamma\gamma$ are simulated with JHUGEN, including all spin corre-

lations in the production and decay processes and interference effects between all contributing amplitudes.

To increase the number of events in the simulated samples for each hypothesis studied, the MELA package [2, 28, 29, 31] is adopted to apply weights to events in any $H \rightarrow VV \rightarrow 4\ell$ or $H \rightarrow WW \rightarrow \ell\nu\ell\nu$ spin-zero sample to model any other spin-zero sample. The same reweighting technique has also been used in the study of the $q\bar{q}$ and $gg \rightarrow ZZ/Z\gamma^*$ backgrounds.

All MC samples are interfaced with PYTHIA 6.4.24 [83] for parton showering and further processing through a dedicated simulation of the CMS detector based on GEANT4 [84]. The simulation includes overlapping pp interactions (pileup) matching the distribution of the number of interactions per LHC beam crossing observed in data.

Most of the background event simulation is unchanged since Refs. [12–15]. In the $H \rightarrow VV \rightarrow 4\ell$ analysis, the $q\bar{q} \rightarrow ZZ/Z\gamma^*$ process is simulated with POWHEG. The $gg \rightarrow ZZ/Z\gamma^*$ process is simulated with both GG2ZZ 3.1.5 [85] and MCFM 6.7 [86–88], where the Higgs boson production K-factor is applied to the LO cross section [13]. In the $H \rightarrow WW \rightarrow \ell\nu\ell\nu$ analysis, the WZ, ZZ, VVV, Drell–Yan (DY) production of Z/γ^* , W+jets, $W\gamma^*$, and $q\bar{q} \rightarrow WW$ processes are generated using the MADGRAPH 5.1 event generator [89], the $gg \rightarrow WW$ process using the GG2WW 3.1 generator [90], and the $t\bar{t}$ and tW processes are generated with POWHEG. The electroweak production of the non-resonant $WW + 2$ jets process, which is not part of the inclusive $WW +$ jets sample, has been generated using the PHANTOM 1.1 event generator [91] including terms of order (α_{EM}^6) . The TAUOLA package [92] is used in the simulation of τ -lepton decays to account for τ -polarization effects.

3.2 Event reconstruction

The analysis uses the same event reconstruction and selection as in the previous measurements of the properties of the Higgs boson in the $H \rightarrow VV \rightarrow 4\ell$ [12, 13], $H \rightarrow WW \rightarrow \ell\nu\ell\nu$ [14], and $H \rightarrow \gamma\gamma$ [15] channels. The data from the CMS detector and the simulated samples are reconstructed using the same algorithms.

For the $H \rightarrow VV \rightarrow 4\ell$ and $H \rightarrow WW \rightarrow \ell\nu\ell\nu$ analyses described in this paper, events are triggered by requiring the presence of two leptons, electrons or muons, with asymmetric requirements on their transverse momenta, p_T . Several single-lepton triggers with relatively tight lepton identification are used for the $H \rightarrow WW$ analysis. A triple-electron trigger is also used for the $H \rightarrow VV \rightarrow 4\ell$ analysis. For the $H \rightarrow \gamma\gamma$ analysis, the events are selected by diphoton triggers with asymmetric transverse energy thresholds and complementary photon selections. The particle-flow (PF) algorithm [93, 94] is used to reconstruct the observable particles in the event. The PF event reconstruction consists of reconstructing and identifying each single particle with an optimized combination of all sub-detector information.

The $H \rightarrow VV \rightarrow 4\ell$ and $H \rightarrow WW \rightarrow \ell\nu\ell\nu$ analyses require four and two lepton candidates (electrons or muons), respectively, originating from a vertex with the largest $\sum p_T^2$ of all tracks associated with it. Electron candidates are defined by a reconstructed charged-particle track in the tracking detector pointing to an energy deposition in the ECAL. The electron energy is measured primarily from the ECAL cluster energy. Muon candidates are identified by signals of charged-particle tracks in the muon system that are compatible with a track reconstructed in the central tracking system. Electrons and muons are required to be isolated. Electrons are reconstructed within the geometrical acceptance, $|\eta| < 2.5$, and for $p_T > 7$ GeV. Muons are reconstructed within $|\eta| < 2.4$ and $p_T > 5$ GeV [95].

Photons, used in the $H \rightarrow \gamma\gamma$ analysis, are identified as ECAL energy clusters not linked to

the extrapolation of any charged-particle trajectory to the ECAL. Jets, used in the $H \rightarrow WW$ analysis, are reconstructed from the PF candidates, clustered with the anti- k_t algorithm [96, 97] with a size parameter of 0.5. The jet momentum is determined as the vector sum of all particle momenta in the jet. Identification of b-quark decays is used to reject backgrounds containing top quarks that subsequently decay to a b quark and a W boson in the $H \rightarrow WW$ analysis. The missing transverse energy vector \vec{E}_T^{miss} is defined as the negative vector sum of the transverse momenta of all reconstructed particles (charged or neutral) in the event, with $E_T^{\text{miss}} = |\vec{E}_T^{\text{miss}}|$.

3.3 Four-lepton event selection

To study the $H \rightarrow VV \rightarrow 4\ell$ decay, events are selected with at least four identified and isolated electrons or muons. A $V \rightarrow \ell^+\ell^-$ candidate originating from a pair of leptons of the same flavor and opposite charge is required. The $\ell^+\ell^-$ pair with an invariant mass, m_1 , nearest to the nominal Z boson mass is retained and is denoted Z_1 if it is in the range $40 \leq m_1 \leq 120$ GeV. A second $\ell^+\ell^-$ pair, denoted Z_2 , is required to have $12 \leq m_2 \leq 120$ GeV. If more than one Z_2 candidate satisfies all criteria, the pair of leptons with the highest scalar p_T sum is chosen. At least one lepton should have $p_T \geq 20$ GeV, another one $p_T \geq 10$ GeV and any oppositely charged pair of leptons among the four selected must satisfy $m_{\ell\ell} \geq 4$ GeV. Events are restricted to a window around the observed 125.6 GeV resonance, $105.6 \leq m_{4\ell} \leq 140.6$ GeV.

After the selection, the dominant background for $H \rightarrow VV \rightarrow 4\ell$ originates from the $q\bar{q} \rightarrow ZZ/Z\gamma^*$ and $gg \rightarrow ZZ/Z\gamma^*$ processes and is evaluated from simulation, following Refs. [12, 13]. The other backgrounds come from the production of Z and WZ bosons in association with jets, as well as $t\bar{t}$, with one or two jets misidentified as an electron or a muon. The $Z + X$ background is evaluated using a tight-to-loose misidentification rate method [12]. The number of estimated background and signal events, and the number of observed candidates after the final selection in data in the narrow mass region around 125.6 GeV is given in Table 3.

Table 3: Number of background (Bkg.) and signal events expected in the SM, and number of observed candidates, for the $H \rightarrow VV \rightarrow 4\ell$ analysis after the final selection in the mass region $105.6 < m_{4\ell} < 140.6$ GeV. The signal and ZZ background are estimated from MC simulation, while the $Z + X$ background is estimated from data. Only systematic uncertainties are quoted.

Channel	4e		4 μ		2e2 μ	
	7 TeV	8 TeV	7 TeV	8 TeV	7 TeV	8 TeV
$q\bar{q} \rightarrow ZZ$	0.84 ± 0.10	2.94 ± 0.33	1.80 ± 0.11	7.65 ± 0.49	2.24 ± 0.28	8.86 ± 0.68
$gg \rightarrow ZZ$	0.03 ± 0.01	0.20 ± 0.05	0.06 ± 0.02	0.41 ± 0.10	0.07 ± 0.02	0.50 ± 0.13
$Z + X$	0.62 ± 0.14	2.77 ± 0.62	0.22 ± 0.09	1.19 ± 0.48	1.06 ± 0.29	4.29 ± 1.10
Bkg.	1.49 ± 0.17	5.91 ± 0.71	2.08 ± 0.14	9.25 ± 0.69	3.37 ± 0.40	13.65 ± 1.30
Signal	0.70 ± 0.11	3.09 ± 0.47	1.24 ± 0.14	5.95 ± 0.71	1.67 ± 0.26	7.68 ± 0.98
Observed	1	9	3	15	6	16

3.4 Two-lepton event selection

In the case of the $H \rightarrow WW \rightarrow \ell\nu\ell\nu$ analysis, events with exactly one electron and one muon are selected. The leptons must have opposite charge and pass the full identification and isolation criteria presented in detail in Ref. [14]. The highest- p_T (leading) lepton should have $p_T > 20$ GeV, and the second one $p_T > 10$ GeV. Events are classified according to the number of selected jets that satisfy $E_T > 30$ GeV and $|\eta| < 4.7$. Two categories of events with exactly zero and exactly one jet are selected, in which the signal is produced mostly by the gluon

fusion process. The $e\mu$ pair is required to have an invariant mass above 12 GeV, and a p_T above 30 GeV. Events are also required to have *projected* E_T^{miss} above 20 GeV, as defined in Ref. [14].

The main background processes from non-resonant WW production and from top-quark production, including top-quark pair ($t\bar{t}$) and single-top-quark (mainly tW) processes, are estimated using data. Instrumental backgrounds arising from misidentified (“nonprompt”) leptons in W+jets production and mismeasurement of \vec{E}_T^{miss} in Z/γ^* +jets events are also estimated from data. The contributions from other sub-dominant diboson (WZ and ZZ) and triboson (VVV) production processes are estimated from simulation. The $W\gamma^*$ cross section is measured from data. The shapes of the discriminant variables used in the signal extraction for the $W\gamma$ process are also obtained from data. The $Z/\gamma^* \rightarrow \tau^+\tau^-$ background process is estimated using $Z/\gamma^* \rightarrow \mu^+\mu^-$ events selected in data where the muons are replaced with simulated τ -lepton decays. To suppress the background from top-quark production, events that are identified as coming from top decays are rejected based on soft-muon and b-jet identification. The number of estimated background and signal events, and number of observed candidates after the final selection are given in Table 4. After all selection criteria are applied, the contribution from other Higgs boson decay channels is negligible.

Table 4: Number of background and signal events expected in the SM, and number of observed candidates, for the $H \rightarrow WW$ analysis after final selection. The signal and background are estimated from MC simulation and from data control regions, as discussed in the text. Only systematic uncertainties are quoted.

Channel Energy	0-jet		1-jet	
	7 TeV	8 TeV	7 TeV	8 TeV
WW	861 ± 12	4185 ± 63	249.9 ± 4.0	1268 ± 21
WZ + ZZ + Z/γ^*	22.7 ± 1.2	178.3 ± 9.5	26.4 ± 1.4	193 ± 11
$t\bar{t}$ + tW	91 ± 20	500 ± 96	226 ± 14	1443 ± 46
W+jets	150 ± 39	620 ± 160	60 ± 16	283 ± 72
$W\gamma^{(*)}$	68 ± 20	282 ± 76	10.1 ± 2.8	55 ± 14
Background	1193 ± 50	5760 ± 210	573 ± 22	3242 ± 90
Signal $gg \rightarrow H$	50 ± 10	227 ± 46	17.1 ± 5.5	88 ± 28
Signal VBF+VH	0.44 ± 0.03	10.27 ± 0.41	2.09 ± 0.12	19.83 ± 0.81
Observed	1207	5747	589	3281

3.5 Two-photon event selection

In the $H \rightarrow \gamma\gamma$ analysis, the energy of photons used in the global event reconstruction is directly obtained from the ECAL measurement. The selection requires a loose calorimetric identification based on the shape of the electromagnetic shower and loose isolation requirements on the photon candidates. For the spin-parity studies, the “cut-based” analysis described in Ref. [15] is used. This analysis does not use multivariate techniques for selection or classification of events, which allows for a categorization better suited for the study of the Higgs boson decay kinematics. The cosine of the scattering angle in the Collins–Soper frame, $\cos\theta^*$, is used to discriminate between the spin hypotheses. The angle is defined in the diphoton rest frame as that between the collinear photons and the line that bisects the acute angle between the colliding protons. To increase the sensitivity, the events are categorized using the same four diphoton event classes used in the cut-based analysis but without the additional classification based on p_T used there. Within each diphoton class, the events are binned in $|\cos\theta^*|$ to discriminate between the different spin hypotheses. The events are thus split into 20 event classes, four (η, R_9) [15] diphoton classes with five $|\cos\theta^*|$ bins each, for both the 7 and 8 TeV datasets,

giving a total of 40 event classes. In Table 5, the number of estimated background and signal events, and number of observed candidates are given after the final selection in an $m_{\gamma\gamma}$ range centered at $m_H = 125$ GeV and corresponding to the full width at half maximum for the signal distribution for each of the four (η, R_9) categories. The total expected number of selected signal events, summed over all categories and integrated over the full signal distribution, is 421 (94) at 8 TeV (7 TeV).

Table 5: Number of background and signal events expected in the SM, and number of observed candidates, for the $H \rightarrow \gamma\gamma$ analysis after final selection. The four categories are defined as follows [15]: low $|\eta|$ indicates that both photons are in the barrel with $|\eta| < 1.5$ and high $|\eta|$ otherwise, high R_9 indicates that both photons have $R_9 > 0.94$ and low R_9 otherwise. The $m_{\gamma\gamma}$ range (GeV) centered at $m_H = 125$ GeV corresponds to the full width at half maximum for the signal distribution in each category. Only systematic uncertainties are quoted, which include uncertainty from the background $m_{\gamma\gamma}$ parameterization in the background estimates.

Channel	(low $ \eta $, high R_9)		(low $ \eta $, low R_9)		(high $ \eta $, high R_9)		(high $ \eta $, low R_9)	
Energy	7 TeV	8 TeV	7 TeV	8 TeV	7 TeV	8 TeV	7 TeV	8 TeV
Range $m_{\gamma\gamma}$	2.44	2.30	3.34	2.94	4.72	4.58	5.48	5.57
Background	230.1±2.5	875±5	604±4	2210±8	456±8	1685±9	911±6	2045±11
Signal	18.6±2.3	74±9	23.5±3.0	103±13	9.3±1.3	38±5	12.0±1.6	57±8
Observed	263	11047	647	1963	459	1638	913	1988

4 Analysis techniques

The kinematics of the Higgs boson decay to four charged leptons, two charged leptons and two neutrinos, or two photons, and their application to the study of the properties of the Higgs boson have been extensively studied in the literature [28–31, 36, 38, 42, 43, 45–49, 51, 53]. The schematic view of the production and decay information can be seen in Fig. 1 [28, 59].

If the resonance has a non-zero spin, its polarization depends on the production mechanism. As a result, a non-trivial correlation of the kinematic distributions of production and sequential decay is observed for a resonance with non-zero spin, while there is no such direct correlation due to polarization for a spin-zero resonance. Furthermore, the kinematics and polarization of the vector bosons in the $H \rightarrow VV$ process depend on the initial polarization of the resonance and the tensor structure of the HVV interactions and this affects the kinematics of the leptons in the $VV \rightarrow 4\ell$ or $\ell\nu\ell\nu$ decay.

The analysis of the HVV interactions requires the study of the kinematic distributions of the Higgs boson decay products comparing to the prediction of the corresponding models. In the case of the $H \rightarrow VV \rightarrow 4\ell$ decay, the full kinematic information can be reconstructed with small experimental uncertainties. In the case of the $H \rightarrow WW \rightarrow \ell\nu\ell\nu$ decay, the two missing neutrinos lead to a loss of kinematic information, but in some cases the V-A nature of the $W \rightarrow \ell\nu$ coupling, compared to a different V-A coupling in the $Z \rightarrow \ell\ell$ decay, leads to more pronounced kinematic effects. In the following, the partial kinematic information used in the analysis of this decay mode is also introduced.

The spin-parity analysis of the $H \rightarrow \gamma\gamma$ decay is also possible and this channel is studied in the context of the exotic spin-two hypothesis tested with respect to the SM hypothesis. However, only one angle θ^* out of the five identified in Fig. 1 is observable in this case. Its distribution is isotropic in the boson frame for any spin-zero model, and therefore such models cannot be distinguished in this way. Details of the reconstruction and analysis of the $\cos\theta^*$ distribution

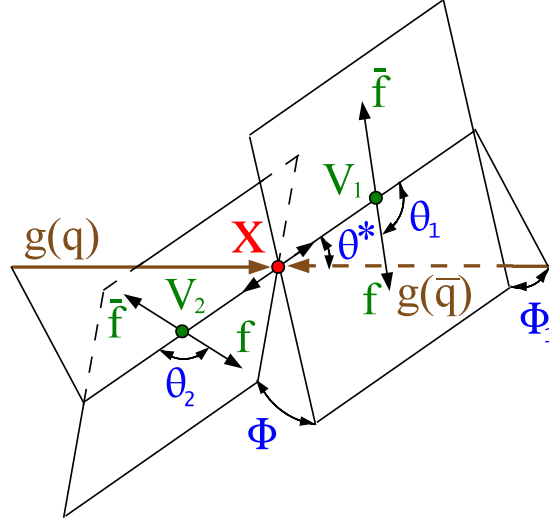


Figure 1: Illustration of the production of a system X in a parton collision and its decay to two vector bosons gg or $q\bar{q} \rightarrow X \rightarrow ZZ, WW, Z\gamma$, and $\gamma\gamma$ either with or without sequential decay of each vector boson to a fermion-antifermion pair [28, 59]. The two production angles θ^* and Φ_1 are shown in the X rest frame and the three decay angles θ_1 , θ_2 , and Φ are shown in the V rest frames. Here X stands either for a Higgs boson, an exotic particle, or, in general, the genuine or misidentified VV system, including background.

in the $H \rightarrow \gamma\gamma$ channel are discussed in Ref. [15].

The rest of this section is organized as follows. The kinematic observables reconstructed in the $H \rightarrow VV \rightarrow 4\ell$ and $H \rightarrow WW \rightarrow \ell\nu\ell\nu$ channels are discussed first. A matrix element likelihood approach is introduced next. Its goal is to reduce the number of observables to be manageable in the following analysis, while retaining full information for the measurements of interest. A maximum likelihood fit employs the template parameterization of the probability distribution of the kinematic observables using full simulation of the processes in the detector. This method is validated with the analytic parameterization of some of the multidimensional distributions using a simplified modeling of the detector response in the $H \rightarrow ZZ \rightarrow 4\ell$ channel. Systematic uncertainties and validation tests are also discussed.

4.1 Observables in the $H \rightarrow VV \rightarrow 4\ell$ analysis

The four-momenta of the $H \rightarrow 4\ell$ decay products carry eight independent degrees of freedom, which fully describe the kinematic configuration of a four-lepton system in its center-of-mass frame, except for an arbitrary rotation around the beam axis. These can be conveniently expressed in terms of the five angles $\vec{\Omega} \equiv (\theta^*, \Phi_1, \theta_1, \theta_2, \Phi)$ defined in Fig. 1, the invariant masses of the dilepton pairs, m_1 and m_2 , and of the four-lepton system, $m_{4\ell}$. The boost of the H boson system in the laboratory frame, expressed as p_T and rapidity, depends on the production mechanism and generally carries some but limited discrimination power between either signal or background hypotheses originating from different production processes. These observables are not used in the analysis to remove the dependence of the results on the production model. For the same reason, information about particles produced in association with H boson is not used either. This approach differs from the study reported in Ref. [12] where such observables were used to investigate the production mechanisms of the Higgs boson.

The distributions of the eight kinematic observables $(m_1, m_2, m_{4\ell}, \vec{\Omega})$ in data, as well as the expectations for the SM background, the Higgs boson signal, and some characteristic alternative

spin-zero scenarios are shown in Fig. 2. All distributions in Fig. 2, with the exception of the $m_{4\ell}$ distribution, are presented using events in the $m_{4\ell}$ range of 121.5 – 130.5 GeV to enhance the signal purity. The observables with their correlations are used in the analysis to establish the consistency of the spin and parity quantum numbers and tensor structure of interactions with respect to the SM predictions. These observables also permit a further discrimination of signal from background, increasing the signal sensitivity and reducing the statistical uncertainty in the measurements.

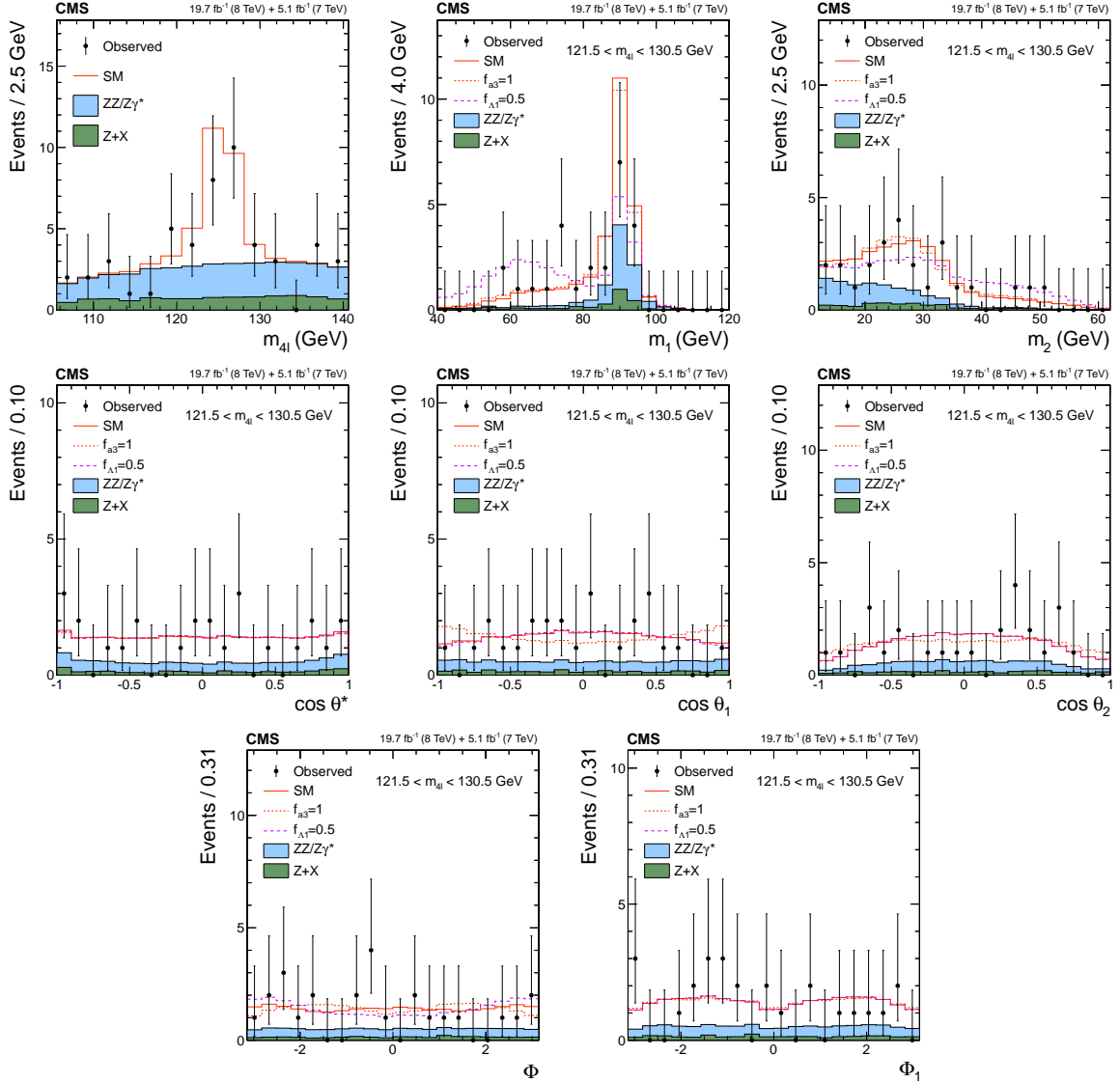


Figure 2: Distributions of the eight kinematic observables used in the $H \rightarrow VV \rightarrow 4\ell$ analysis: $m_{4\ell}$, m_1 , m_2 , $\cos \theta^*$, $\cos \theta_1$, $\cos \theta_2$, Φ , and Φ_1 . The observed data (points with error bars), the expectations for the SM background (shaded areas), the SM Higgs boson signal (open areas under the solid histogram), and the alternative spin-zero resonances (open areas under the dashed histograms) are shown, as indicated in the legend. The mass of the resonance is taken to be 125.6 GeV and the SM cross section is used. All distributions, with the exception of $m_{4\ell}$, are presented with the requirement $121.5 < m_{4\ell} < 130.5$ GeV.

4.2 Observables in the $H \rightarrow WW \rightarrow \ell\nu\ell\nu$ analysis

Only partial reconstruction is possible in the $H \rightarrow WW \rightarrow \ell\nu\ell\nu$ decay. This channel features two isolated, high- p_T , charged leptons and E_T^{miss} due to the presence of neutrinos in the final state. The kinematic distributions of the decay products exhibit the characteristic properties of the parent boson. There are three main observables in this channel: the azimuthal opening angle between the two leptons ($\Delta\phi_{\ell\ell}$), which is correlated with the spin of the Higgs boson; the dilepton mass ($m_{\ell\ell}$), which is one of the most discriminating kinematic variables for a Higgs boson with low mass, and it is also correlated to the spin and to $\Delta\phi_{\ell\ell}$; and the transverse mass (m_T) of the final state objects, which scales with the Higgs boson mass. The transverse mass is defined as $m_T^2 = 2p_T^{\ell\ell} E_T^{\text{miss}} (1 - \cos \Delta\phi(\ell\ell, \vec{E}_T^{\text{miss}}))$, where $p_T^{\ell\ell}$ is the dilepton transverse momentum and $\Delta\phi(\ell\ell, \vec{E}_T^{\text{miss}})$ is the azimuthal angle between the dilepton momentum and \vec{E}_T^{miss} .

Two observables are used in the final analysis, $m_{\ell\ell}$ and m_T . These two kinematic observables are independent quantities that effectively discriminate the signal against most of the backgrounds and between different signal models in the dilepton analysis in the 0-jet and 1-jet categories and have already been used in Ref. [14]. The signal region is defined by $m_{\ell\ell} < 200$ GeV, and $60 \leq m_T \leq 280$ GeV. The distributions of these observables for data, an expected SM Higgs signal, an alternative signal model with $f_{a3}^{WW} = -0.4$, and backgrounds are presented in Fig. 3.

4.3 Observables in the matrix element likelihood approach

A comprehensive analysis of the kinematics of the decay of a Higgs boson would include up to eight observables, as discussed above. In such an analysis, it is required to have a parameterization of the multidimensional distributions as a function of the parameters of interest. However, it becomes challenging to describe all the correlations of the observables and detector effects. It is possible to reduce the number of observables and keep the necessary information using the matrix element likelihood approach. In this approach, the kinematic information is stored in a discriminant designed for the separation of either background, the alternative signal components, or interference between those components. The parameterization of up to three observables can be performed with full simulation or data from the control regions. This approach is adopted in the $H \rightarrow VV \rightarrow 4\ell$ analysis. A similar approach is also possible in the $H \rightarrow WW \rightarrow \ell\nu\ell\nu$ channel, but the construction of the discriminants is more challenging because of the presence of unobserved neutrinos. Therefore, a simpler approach with the two observables defined above is used in this case.

The use of kinematic discriminants in Higgs boson studies was introduced in previous CMS analyses [2, 11–13] and feasibility studies [29, 31], and here it is extended both to a number of new models and to new techniques. The construction of the kinematic discriminants follows the matrix element likelihood approach, where the probabilities for an event are calculated using the LO matrix elements as a function of angular and mass observables. In this way, the kinematic information, which fully characterizes the 4ℓ event topology of a certain process in its center-of-mass frame, is condensed to a reduced number of observables.

The kinematic discriminants used in this study are computed using the MELA package [2, 28, 29, 31], which provides the full set of processes studied in this paper and uses JHUGEN matrix elements for the signal, gg or $q\bar{q} \rightarrow X \rightarrow ZZ / Z\gamma^* / \gamma^*\gamma^* \rightarrow 4\ell$, and MCFM matrix elements for the background, gg or $q\bar{q} \rightarrow ZZ / Z\gamma^* / \gamma^*\gamma^* / Z \rightarrow 4\ell$. This library of processes is also consistent with the MC simulation used, as discussed in Section 3, and also includes other production and decay mechanisms. Within the MELA framework, an analytic parameterization of the matrix elements for signal [28, 29] and background [30] was adopted in the previous CMS analyses, reported in Refs. [2, 3, 11]. The above matrix element calculations are

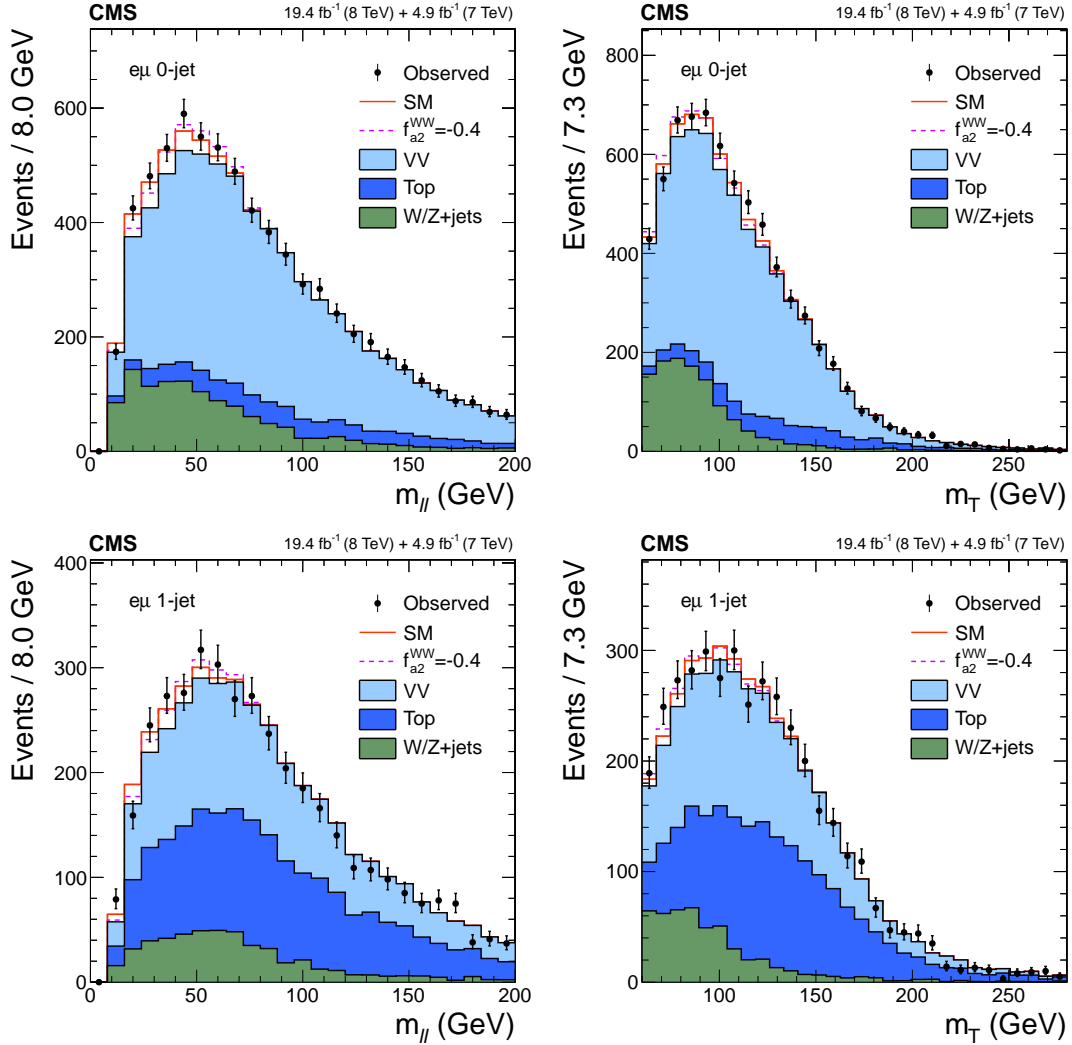


Figure 3: Distributions of $m_{\ell\ell}$ (left) and m_T (right) for events with 0 jets (upper row) and 1 jet (lower row) in the $H \rightarrow WW \rightarrow l\nu l\nu$ analysis. The observed data (points with error bars), the expectations for the SM background (shaded areas), the SM Higgs boson signal (open areas under the solid histogram), and the alternative spin-zero resonance (open areas under the dashed histograms) are shown, as indicated in the legend. The mass of the resonance is taken to be 125.6 GeV and the SM cross section is used.

validated against each other and tested with the MEKD package [98], which is based on MADGRAPH and FEYNRULES [99], for a subset of processes implemented in common. The analytic parameterizations of the spin-zero signal and $q\bar{q} \rightarrow ZZ / Z\gamma^* \rightarrow 4\ell$ background processes are available from an independent implementation [30, 33, 56] and are used in a multidimensional distribution parameterization without the calculation of discriminants.

Given several signal hypotheses defined for gg or $q\bar{q} \rightarrow X \rightarrow ZZ / Z\gamma^* / \gamma^*\gamma^* \rightarrow 4\ell$, and the main background hypotheses gg or $q\bar{q} \rightarrow ZZ / Z\gamma^* / \gamma^*\gamma^* / Z \rightarrow 4\ell$, the effective probabilities are defined for each event using a set of kinematic observables $(m_1, m_2, m_{4\ell}, \vec{\Omega})$

$$\begin{aligned}
\mathcal{P}_{\text{SM}} &= \mathcal{P}_{\text{SM}}^{\text{kin}}(m_1, m_2, \vec{\Omega}|m_{4\ell}) \times \mathcal{P}_{\text{sig}}^{\text{mass}}(m_{4\ell}|m_{\text{H}}), \\
\mathcal{P}_{J^P} &= \mathcal{P}_{J^P}^{\text{kin}}(m_1, m_2, \vec{\Omega}|m_{4\ell}) \times \mathcal{P}_{\text{sig}}^{\text{mass}}(m_{4\ell}|m_{\text{H}}), \\
\mathcal{P}_{J^P}^{\text{int}} &= \left(\mathcal{P}_{\text{SM}+J^P}^{\text{kin}}(m_1, m_2, \vec{\Omega}|m_{4\ell}) - \mathcal{P}_{J^P}^{\text{kin}}(m_1, m_2, \vec{\Omega}|m_{4\ell}) - \mathcal{P}_{\text{SM}}^{\text{kin}}(m_1, m_2, \vec{\Omega}|m_{4\ell}) \right), \\
\mathcal{P}_{J^P}^{\text{int}\perp} &= \left(\mathcal{P}_{\text{SM}+J^P\perp}^{\text{kin}}(m_1, m_2, \vec{\Omega}|m_{4\ell}) - \mathcal{P}_{J^P}^{\text{kin}}(m_1, m_2, \vec{\Omega}|m_{4\ell}) - \mathcal{P}_{\text{SM}}^{\text{kin}}(m_1, m_2, \vec{\Omega}|m_{4\ell}) \right), \\
\mathcal{P}_{q\bar{q}ZZ} &= \mathcal{P}_{q\bar{q}ZZ}^{\text{kin}}(m_1, m_2, \vec{\Omega}|m_{4\ell}) \times \mathcal{P}_{q\bar{q}ZZ}^{\text{mass}}(m_{4\ell}), \\
\mathcal{P}_{ggZZ} &= \mathcal{P}_{ggZZ}^{\text{kin}}(m_1, m_2, \vec{\Omega}|m_{4\ell}) \times \mathcal{P}_{ggZZ}^{\text{mass}}(m_{4\ell}),
\end{aligned} \tag{17}$$

where $\mathcal{P}^{\text{kin}}(m_1, m_2, \vec{\Omega}|m_{\text{H}}) = |A(m_1, m_2, \vec{\Omega}|m_{\text{H}})|^2$ are the probabilities computed from the LO matrix elements and generally are not normalized. The variable $\mathcal{P}^{\text{mass}}(m_{4\ell}|m_{\text{H}})$ is the probability as a function of the four-lepton reconstructed mass and is calculated using the $m_{4\ell}$ parameterization described in Refs. [11, 12] including the $m_{\text{H}} = 125.6$ GeV hypothesis for signal. The probabilities $\mathcal{P}_{J^P}^{\text{int}}$ parameterize interference between contributions from the SM and anomalous couplings, where J^P refers to a spin-zero tensor structure of interest, and are allowed to have both positive and negative values. In the calculation of the mixed amplitude used for $\mathcal{P}_{\text{SM}+J^P}^{\text{kin}}$, the same coupling strengths are used as in the individual probabilities $\mathcal{P}_{\text{SM}}^{\text{kin}}$ and $\mathcal{P}_{J^P}^{\text{kin}}$, and these couplings are required to provide equal cross sections for the two individual processes. The quantity $\mathcal{P}_{J^P}^{\text{int}\perp}$ is constructed in the same way as $\mathcal{P}_{J^P}^{\text{int}}$ except that the phase of the J^P amplitude is changed by $\pi/2$. The matrix element calculations in Eq. (17) are also used for the re-weighting of simulated samples, as discussed in Section 3.

Several kinematic discriminants are constructed for the main signal and background processes from the set of probabilities described above

$$\begin{aligned}
\mathcal{D}_{\text{bkg}} &= \frac{\mathcal{P}_{\text{SM}}}{\mathcal{P}_{\text{SM}} + c \times \mathcal{P}_{q\bar{q}ZZ}} = \left[1 + c(m_{4\ell}) \times \frac{\mathcal{P}_{q\bar{q}ZZ}^{\text{kin}}(m_1, m_2, \vec{\Omega}|m_{4\ell}) \times \mathcal{P}_{q\bar{q}ZZ}^{\text{mass}}(m_{4\ell})}{\mathcal{P}_{\text{SM}}^{\text{kin}}(m_1, m_2, \vec{\Omega}|m_{4\ell}) \times \mathcal{P}_{\text{sig}}^{\text{mass}}(m_{4\ell}|m_{\text{H}})} \right]^{-1}, \\
\mathcal{D}_{J^P} &= \frac{\mathcal{P}_{\text{SM}}}{\mathcal{P}_{\text{SM}} + \mathcal{P}_{J^P}} = \left[1 + \frac{\mathcal{P}_{J^P}^{\text{kin}}(m_1, m_2, \vec{\Omega}|m_{4\ell})}{\mathcal{P}_{\text{SM}}^{\text{kin}}(m_1, m_2, \vec{\Omega}|m_{4\ell})} \right]^{-1}, \\
\mathcal{D}_{\text{int}} &= \frac{\mathcal{P}_{J^P}^{\text{int}}(m_1, m_2, \vec{\Omega}|m_{4\ell})}{\mathcal{P}_{\text{SM}}^{\text{kin}} + \mathcal{P}_{J^P}^{\text{kin}}}.
\end{aligned} \tag{18}$$

Here, the coefficient $c(m_{4\ell})$ is tuned to adjust the relative normalization of the signal and background probabilities for a given value of $m_{4\ell}$. The observable \mathcal{D}_{bkg} is used to separate signal from $q\bar{q} \rightarrow ZZ$, $gg \rightarrow ZZ$, and $Z + X$ backgrounds, using the $m_{4\ell}$ probability in addition to \mathcal{P}^{kin} . The discriminant \mathcal{D}_{J^P} is created to separate the SM signal from an alternative J^P state. The discriminant \mathcal{D}_{int} is created to isolate interference between the SM and anomalous coupling

contributions. Since the analysis is designed to probe small anomalous couplings, interference between different anomalous contributions is a negligible effect and dedicated discriminants for those contributions are not considered. The variable \mathcal{D}_{int} is denoted as \mathcal{D}_{CP} for interference between the a_1 and a_3 contributions because it is sensitive to CP violation [31].

To remove the dependence of the spin-one and spin-two discriminants on the production model, the probability \mathcal{P}^{kin} is averaged over the two production angles $\cos\theta^*$ and Φ_1 , defined in Fig. 1, or equivalently the signal matrix element squared is averaged over the polarization of the resonance [31]. The production independent discriminants are defined as

$$\begin{aligned} \mathcal{D}_{\text{bkg}}^{\text{dec}} &= \left[1 + c(m_{4\ell}) \times \frac{\frac{1}{4\pi} \int d\Phi_1 d\cos\theta^* \mathcal{P}_{\text{q}\bar{\text{q}}\text{ZZ}}^{\text{kin}}(m_1, m_2, \vec{\Omega}|m_{4\ell}) \times \mathcal{P}_{\text{q}\bar{\text{q}}\text{ZZ}}^{\text{mass}}(m_{4\ell})}{\mathcal{P}_{\text{SM}}^{\text{kin}}(m_1, m_2, \vec{\Omega}|m_{4\ell}) \times \mathcal{P}_{\text{sig}}^{\text{mass}}(m_{4\ell}|m_{\text{H}})} \right]^{-1}, \\ \mathcal{D}_{\text{JP}}^{\text{dec}} &= \left[1 + \frac{\frac{1}{4\pi} \int d\Phi_1 d\cos\theta^* \mathcal{P}_{\text{JP}}^{\text{kin}}(m_1, m_2, \vec{\Omega}|m_{4\ell})}{\mathcal{P}_{\text{SM}}^{\text{kin}}(m_1, m_2, \vec{\Omega}|m_{4\ell})} \right]^{-1}. \end{aligned} \quad (19)$$

The decay kinematics of a spin-zero resonance are already independent of the production mechanism, due to the lack of spin correlations for any spin-zero particle. The small differences in the distributions of the production-independent discriminants with the different production mechanisms are due to detector acceptance effects and are treated as systematic uncertainties.

A complete list of all the discriminants used in the analysis is presented in Table 6. Some examples of the distributions as expected from simulation and as observed in data can be seen in Fig. 4 for all the discriminants used in the study of the spin-zero HZZ couplings. A complete list of the measurements performed and observables used is discussed in Sections 5 and 6.

4.4 Maximum likelihood fit with the template method

The goal of the analysis is to determine if a set of anomalous coupling parameters $\vec{\zeta}$, defined both for the production and decay of a resonance with either spin zero, one, or two is consistent, for a given set of observables \vec{x} , with the data. The coupling parameters $\vec{\zeta}$ are discussed in detail in Section 2. They are summarized in Eqs. (1), (3), (4) and Table 1 for spin-zero, in Eqs. (8) and (10) for spin-one, and in Eqs. (11), (14) and Table 2 for spin-two. The observables \vec{x}_i are defined for each event i , listed in Table 6, and discussed above. The extended likelihood function is defined for N candidate events as

$$\mathcal{L} = \exp\left(-n_{\text{sig}} - \sum_k n_{\text{bkg}}^k\right) \prod_i^N \left(n_{\text{sig}} \times \mathcal{P}_{\text{sig}}(\vec{x}_i; \vec{\zeta}) + \sum_k n_{\text{bkg}}^k \times \mathcal{P}_{\text{bkg}}^k(\vec{x}_i) \right), \quad (20)$$

where n_{sig} is the number of signal events and n_{bkg}^k is the number of background events of type k . The probability density functions $\mathcal{P}_{\text{sig}}(\vec{x}_i; \vec{\zeta})$ and $\mathcal{P}_{\text{bkg}}^k(\vec{x}_i)$ are defined for the signal and background, respectively.

There are several event categories, such as $4e$, 4μ , and $2e2\mu$ in the $\text{H} \rightarrow \text{VV} \rightarrow 4\ell$ analysis, 0 and 1-jet in the $\text{H} \rightarrow \text{WW} \rightarrow \ell\nu\ell\nu$ analysis, or the 7 TeV and 8 TeV categories, and several types of background. The total signal yield n_{sig} is a free parameter to avoid using the overall signal event yield as a part of the discrimination between alternative hypotheses. However, when several channels are used in the same decay, such as $\text{H} \rightarrow \text{VV} \rightarrow 4e$, $2e2\mu$, and 4μ , the relative yields between the channels depend on the terms considered in the tensor structure due to interference effects in the presence of identical leptons, and this information is exploited in the analysis.

Table 6: List of observables \vec{x} used in the analysis of the HVV couplings. The J^P notation for spin-two refers to the ten scenarios defined in Table 2. The $H \rightarrow \gamma\gamma$ channel is illustrated with two main observables, where $\cos\theta^*$ represents categories constructed from the angular and other observables, and more details are given in Section 3.5 and Ref. [15].

Measurement	Observables \vec{x}		
$f_{\Delta 1}$	\mathcal{D}_{bkg}	$\mathcal{D}_{\Delta 1}$	
f_{a2}	\mathcal{D}_{bkg}	\mathcal{D}_{0h+}	\mathcal{D}_{int}
f_{a3}	\mathcal{D}_{bkg}	\mathcal{D}_{0-}	\mathcal{D}_{CP}
$f_{\Delta 1}^{\text{WW}}$	m_{T}	$m_{\ell\ell}$	
f_{a2}^{WW}	m_{T}	$m_{\ell\ell}$	
f_{a3}^{WW}	m_{T}	$m_{\ell\ell}$	
$f_{\Delta 1}^{Z\gamma}$	\mathcal{D}_{bkg}	$\mathcal{D}_{\Delta 1}^{Z\gamma}$	$\mathcal{D}_{\text{int}}^{Z\gamma, \Delta 1}$
$f_{a2}^{Z\gamma}$	\mathcal{D}_{bkg}	$\mathcal{D}_{a2}^{Z\gamma}$	$\mathcal{D}_{\text{int}}^{Z\gamma}$
$f_{a3}^{Z\gamma}$	\mathcal{D}_{bkg}	$\mathcal{D}_{a3}^{Z\gamma}$	$\mathcal{D}_{\text{CP}}^{Z\gamma}$
$f_{a2}^{\gamma\gamma}$	\mathcal{D}_{bkg}	$\mathcal{D}_{a2}^{\gamma\gamma}$	$\mathcal{D}_{\text{int}}^{\gamma\gamma}$
$f_{a3}^{\gamma\gamma}$	\mathcal{D}_{bkg}	$\mathcal{D}_{a3}^{\gamma\gamma}$	$\mathcal{D}_{\text{CP}}^{\gamma\gamma}$
spin-one $q\bar{q} \rightarrow X(f_{b2}) \rightarrow ZZ$	\mathcal{D}_{bkg}	\mathcal{D}_{1-}	\mathcal{D}_{1+}
spin-one decay $X(f_{b2}) \rightarrow ZZ$	$\mathcal{D}_{\text{bkg}}^{\text{dec}}$	$\mathcal{D}_{1-}^{\text{dec}}$	$\mathcal{D}_{1+}^{\text{dec}}$
spin-two $q\bar{q} \rightarrow X(J^P) \rightarrow ZZ$	\mathcal{D}_{bkg}	$\mathcal{D}_{J^P}^{q\bar{q}}$	
spin-two $gg \rightarrow X(J^P) \rightarrow ZZ$	\mathcal{D}_{bkg}	$\mathcal{D}_{J^P}^{gg}$	
spin-two decay $X(J^P) \rightarrow ZZ$	$\mathcal{D}_{\text{bkg}}^{\text{dec}}$	$\mathcal{D}_{J^P}^{\text{dec}}$	
spin-one $q\bar{q} \rightarrow X(f_{b2}^{\text{WW}}) \rightarrow WW$	m_{T}	$m_{\ell\ell}$	
spin-two gg or $q\bar{q} \rightarrow X(J^P) \rightarrow WW$	m_{T}	$m_{\ell\ell}$	
spin-two gg or $q\bar{q} \rightarrow X(2_m^+) \rightarrow \gamma\gamma$	$m_{\gamma\gamma}$	$\cos\theta^*$	

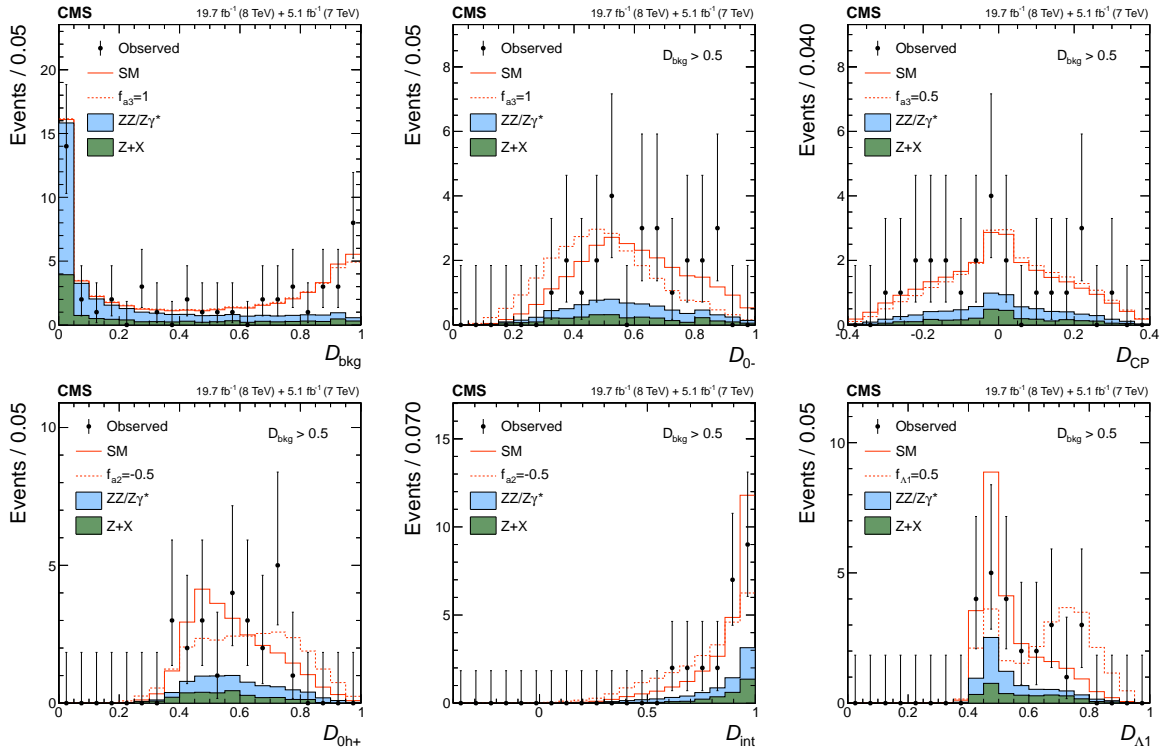


Figure 4: Distributions of the kinematic discriminants for the observed data (points with error bars), the expectations for the SM background (shaded areas), the SM Higgs boson signal (open areas under the solid histogram), and the alternative spin-zero resonances (open areas under the dashed histograms) are shown, as indicated in the legend. The mass of the resonance is taken to be 125.6 GeV and the SM cross section is used. Top row from left to right: D_{bkg} , D_{0-} , D_{CP} ; bottom row from left to right: D_{0h+} , D_{int} , $D_{\Delta 1}$. All distributions, with the exception of D_{bkg} , are shown with the requirement $D_{\text{bkg}} > 0.5$ to enhance signal purity.

The method adopted for all the measurements presented in this paper is a template method. The probability density functions \mathcal{P}_{sig} and $\mathcal{P}_{\text{bkg}}^k$ are described as histograms (templates) with two or three dimensions, see observables in Table 6, and with up to 50 bins in each dimension. The number of dimensions used is limited by the number of simulated events that can be generated or the number of events in the control regions in data. However, an optimal construction of observables allows for the retention of all the necessary information for the measurement with up to three observables. The templates are built for signal and background from histograms of fully simulated events, or from control regions in data. In the $H \rightarrow VV \rightarrow 4\ell$ analyses, where the number of bins is larger than in the $H \rightarrow WW \rightarrow \ell\nu\ell\nu$ analysis, statistical fluctuations are removed using a smoothing algorithm [100, 101].

The signal probability density functions \mathcal{P}_{sig} depend on the coupling parameters $\vec{\zeta}$. For spin-zero, these functions can be parameterized as a linear combination of the terms originating from the SM-like and anomalous amplitudes and their interference [31]

$$\begin{aligned} \mathcal{P}_{\text{sig}}(\vec{x}; \vec{\zeta} = \{f_{ai}, \phi_{ai}\}) &= \left(1 - \sum_{ai} f_{ai}\right) \mathcal{P}_{0^+}(\vec{x}) + \sum_{ai} f_{ai} \mathcal{P}_{ai}(\vec{x}) \\ &+ \sum_{ai} \sqrt{f_{ai} \left(1 - \sum_{aj} f_{aj}\right)} \mathcal{P}_{ai,0^+}^{\text{int}}(\vec{x}; \phi_{ai}) \\ &+ \sum_{ai < aj} \sqrt{f_{ai} f_{aj}} \mathcal{P}_{ai,aj}^{\text{int}}(\vec{x}; \phi_{ai} - \phi_{aj}), \quad (21) \end{aligned}$$

where \mathcal{P}_{ai} is the probability of a pure a_i term and $\mathcal{P}_{ai,aj}^{\text{int}}$ describes the interference between the two terms, each parameterized as a template. Each term in Eq. (21) is extracted from the dedicated simulation and includes proper normalization. For spin-one or spin-two, in the case of a study of non-interfering states there is only one fraction $f(J^P)$ and no interference contribution.

The likelihood in Eq. (20) can be used in two different ways. In both approaches, the likelihood is maximized with respect to the nuisance parameters which include the signal yield and constrained parameters describing the systematic uncertainties discussed in Section 4.5. In one approach the likelihood is maximized to estimate the values of anomalous couplings, and the confidence intervals are determined from profile likelihood scans of the respective parameters. This is used for the measurement of anomalous couplings under the spin-zero hypothesis, as well as for the $f(J^P)$ measurements of the spin-one and spin-two hypotheses. The allowed 68% and 95% CL intervals are defined using the profile likelihood function, $-2 \Delta \ln \mathcal{L} = 1.00$ and 3.84, for which exact coverage is expected in the asymptotic limit [102]. The approximate coverage has been tested with generated samples for several true parameter values and the quoted results have been found to be conservative.

The other approach is used to distinguish an alternative spin-one or spin-two signal hypothesis from the SM Higgs boson. In this case, the test statistic $q = -2 \ln(\mathcal{L}_{J^P} / \mathcal{L}_{0^+})$ is defined using the ratio of signal plus background likelihoods for two signal hypotheses. To quantify the consistency of the observed test statistic q_{obs} with respect to the SM Higgs boson hypothesis (0^+), the probability $p = P(q \leq q_{\text{obs}} | 0^+ + \text{bkg})$ is assessed and converted into a number of standard deviations via the Gaussian one-sided tail integral. The consistency of the observed data with the alternative signal hypothesis (J^P) is assessed from $P(q \geq q_{\text{obs}} | J^P + \text{bkg})$. The CL_s criterion [103, 104], defined as $CL_s = P(q \geq q_{\text{obs}} | J^P + \text{bkg}) / P(q \geq q_{\text{obs}} | 0^+ + \text{bkg}) < \alpha$, is used for the final inference of whether a particular alternative signal hypothesis is excluded or not at a given confidence level $(1 - \alpha)$. The following quantities are used to characterize

the expected and observed results: (i) separation, defined as the tail area A_{tail} calculated at the value of q where the tails of the two distributions have identical area, (ii) the probability of each hypothesis to fluctuate beyond q_{obs} , and (iii) the expected and observed CL_s value. Option (i) is used to characterize the expected results as this quantity is symmetric between the two hypotheses, and it is expressed as the number of standard deviations multiplied by two. Options (ii) and (iii) are used to characterize the observed results for exclusion of a particular hypothesis. The observed separation (ii) is also expressed as the number of standard deviations, and the sign is positive if the tail extends away or negative if it extends towards the median of the other hypothesis.

4.5 Analysis validation and systematic uncertainties

The validation of this analysis and the assignment of systematic uncertainties follows various aspects of the parameterization in Eq. (20). Estimates of the expected background yields and shapes of the probability distributions for signal and background are investigated. The performance of the fit has been tested using events from full simulation discussed in Section 3.1 and using events generated directly from probability distributions. Both approaches are found to give consistent expected results and unbiased parameter estimates in the fit for anomalous couplings for the full spectrum of measurements listed in Table 6. These tests rely on the proper simulation of the signal and background processes and further studies propagate any systematic uncertainties in the simulation to the final results, which are specific to each final state. The overall signal yield is left unconstrained in the fit and therefore the associated theoretical uncertainties do not affect the constraints on anomalous couplings.

The statistical uncertainties dominate over the systematic ones for all the results quoted in this paper. The systematic uncertainties in the $H \rightarrow VV \rightarrow 4\ell$ channel are generally the same as the ones investigated in Ref. [12]. Among the yield uncertainties, experimental systematic uncertainties are evaluated from data for the lepton trigger efficiency and combined object reconstruction, identification, and isolation efficiencies. The theoretical uncertainties on the ZZ background are described in Ref. [12], but the calculations have been updated using the recommendations in Ref. [105] and the treatment of the $gg \rightarrow ZZ/Z\gamma^*$ process follows Ref. [13]. The $Z + X$ uncertainties include the effects on both the expected yields and on the shape. The yield uncertainties are estimated to be 20%, 25%, and 40% for the $4e$, $2e2\mu$, and 4μ decay channels, respectively. The shape uncertainty is taken into account by considering the difference between the $Z + X$ and $q\bar{q} \rightarrow ZZ$ distributions for a particular final state, which was found to cover any potential biases in $Z + X$ parameterization. To account for the lepton momentum scale and resolution uncertainty in the $m_{4\ell}$ distribution, the alternative signal shapes are taken from the variations of both of these contributions, following Ref. [12].

In the $H \rightarrow WW \rightarrow \ell\nu\ell\nu$ analysis, the same treatment of the systematic uncertainties as in Ref. [14] has been performed. The uncertainty related to the size of the simulated samples is such that it is at least a factor of two smaller than the rest of the systematic uncertainties and varies from 1.0% for Higgs boson signal to 20% for some of the backgrounds ($Z/\gamma^* \rightarrow \ell^+\ell^-$, $W+\text{jets}$, and $V\gamma^{(*)}$). Systematic uncertainties are represented by individual nuisance parameters with log-normal distributions. An exception is applied to the $q\bar{q} \rightarrow WW$ normalization, which is an unconstrained parameter in the fit.

The analysis is optimized for the $gg \rightarrow H$ production mode, which has the largest cross section, as verified experimentally [12, 14, 15], and is characterized by low hadronic activity in the final state. Other production modes such as VBF, VH, and $t\bar{t}H$ are considered in the analysis, representing a small or negligible fraction of the signal. In the $H \rightarrow VV \rightarrow 4\ell$ analysis, only the

exclusive four-lepton final state is reconstructed and it has been verified that all observables are similar for all production mechanisms of a spin-zero particle. For the spin-one and spin-two models using decay-only observables, any residual dependence on the production mechanism is small and enters only through the difference in detector acceptance effects. Uncertainties in this approach are accounted for with alternative parameterization of the observable distributions, covering the difference between the gluon fusion and $q\bar{q}$ production mechanisms of a spin-two particle, or an equivalent variation for a spin-one particle production which reflects the difference in the boost of the resonance.

In the $H \rightarrow WW \rightarrow \ell\nu\ell\nu$ analysis, the VBF contribution, which has similar kinematics as $gg \rightarrow H$, represents 5% of the total Higgs boson signal in the 1-jet category, where it is the second-largest mode in terms of rate after $gg \rightarrow H$, and less than 0.5% in the 0-jet bin, where it is highly suppressed. The associated production VH , and in particular ZH , shows some differences in the observables compared to $gg \rightarrow H$ because of the additional vector bosons present in the final state, but contributes less than 1% to the total signal yield in the 0- and 1-jet categories. There is no expected $t\bar{t}H$ contribution in the signal region after all selection requirements. For the measurements presented in Section 5.2, a full combination of all Higgs boson production mechanisms is considered in the parameterization, while the alternative exotic-spin hypotheses are produced via gg , $q\bar{q}$, or a combination of the two. For the measurements presented in Section 6.4, the $gg \rightarrow H$ model is used to create the templates and the full variation of the distributions after the inclusion of all the production mechanisms according to the SM expectation is used for the evaluation of the systematic uncertainties. This approach is taken because a priori the fraction of various production mechanisms is not known for an arbitrary BSM model. However, those fractions have been experimentally constrained to be consistent with the SM expectations [12, 14, 15, 21].

The correlations between the systematic uncertainties in the different categories and final states are taken into account. In particular, the main sources of correlated systematic uncertainties are those related to the experimental measurements such as the integrated luminosity, lepton and trigger selection efficiencies, lepton momentum scale, and the theoretical uncertainties affecting the background processes. Uncertainties in the background normalization or background model parameters from control regions and uncertainties of a statistical nature are uncorrelated.

It is instructive to validate the matrix element method with the study of spin-parity and anomalous interactions of the Z boson, which has already established SM properties [74]. An earlier CMS analysis tested the Z boson couplings to fermions in the two-body decay $q\bar{q} \rightarrow Z/\gamma^* \rightarrow \ell^+\ell^-$ [106], using a matrix element formalism similar to the one used in the Higgs boson studies [28] and established consistency with the SM. Here the study is extended to the four-lepton decay of the Z boson in the topology $q\bar{q} \rightarrow Z/\gamma^* \rightarrow \ell^+\ell^-\gamma^* \rightarrow 4\ell$ [107]. A hypothesis test is performed between the SM Z boson and an exotic Higgs-like resonance $gg \rightarrow H(91.2) \rightarrow ZZ \rightarrow 4\ell$ with the same mass and width as the Z boson. The mass window $80 < m_{4\ell} < 100$ GeV is used, just below the mass range used in the Higgs boson analysis. In addition, the non-resonant $q\bar{q} \rightarrow ZZ/Z\gamma^*/\gamma^*\gamma^* \rightarrow 4\ell$ contribution is parameterized including interference with $q\bar{q} \rightarrow Z/\gamma^* \rightarrow \ell^+\ell^-\gamma^* \rightarrow 4\ell$ following the formalism of Eq. (21) and its effective fractional cross section is fitted in data in analogy with the f_{ai} parameters. The results show that the SM Z boson hypothesis is highly preferred in the data and the small contribution of the production $q\bar{q} \rightarrow ZZ/Z\gamma^*/\gamma^*\gamma^* \rightarrow 4\ell$, including its phase, is consistent with the SM expectation. The alternative Higgs-like hypothesis $H(91.2)$ has been excluded with a $CL > 99.99\%$.

4.6 Analysis validation with analytic parameterization of kinematic distributions

In the $H \rightarrow VV \rightarrow 4\ell$ channel, the template method discussed above can be extended to the complete set of eight kinematic observables $\vec{x} = (m_1, m_2, m_{4\ell}, \vec{\Omega})$ described in Section 4.1 and shown in Fig. 2. Such an approach would allow us to parameterize the data distributions directly without constructing the dedicated discriminants. However, the parameterization of templates in eight dimensions using full simulation is nearly impossible to perform because of the large number of events required. Therefore, a simplified approach is performed with parametrization of eight-dimensional distributions to cross-check a subset of results, specifically measurements of the f_{a2} and f_{a3} parameters in the spin-zero studies (see Section 6). The signal and the dominant $q\bar{q} \rightarrow ZZ/Z\gamma^*$ background are parameterized analytically and reconstruction effects are incorporated in the probability function numerically. About one third of the background events coming from the $Z + X$ and $gg \rightarrow ZZ/Z\gamma^*$ processes is parameterized with the template approach in eight dimensions using generated events with detector effects incorporated using the same approximate numerical parameterization.

The likelihood construction follows Eq. (20) and the probability distribution is equivalent to Eq. (21). The normalization of the probability distributions in eight dimensions is one of the main computational challenges in this approach and is performed with MC integration. The final state with $2e$ and 2μ is split into $2e2\mu$ and $2\mu2e$ sub-categories where the distinction between them is determined by the flavor of the leptons from the Z_1 decay. Additionally, a narrower mass window ($115 - 135$ GeV) is used compared to the template method.

The analytic parameterization is the product of the differential decay cross section, $d\sigma_{4\ell}$, and the production spectrum, W_{prod} , written as

$$\mathcal{P}(\vec{p}_T, Y, \Phi^*, \vec{x}|\vec{\zeta}) = W_{\text{prod}}(\vec{p}_T, Y, \Phi^*, \hat{s}) \times \frac{d\sigma_{4\ell}(m_{4\ell}, m_1, m_2, \vec{\Omega}|\vec{\zeta})}{dm_1^2 dm_2^2 d\vec{\Omega}}, \quad (22)$$

where \vec{p}_T , Y , and Φ^* are the transverse momentum, rapidity, and azimuthal orientation of the four-lepton system illustrated in Fig. 1, and $\hat{s} = m_{4\ell}^2$ is the center-of-mass energy of the parton-parton system. In order to convert the above probability to an expression in terms of detector-level reconstructed observables, it is convoluted with a transfer function $T(\vec{x}^{\text{R}}|\vec{x}^{\text{G}})$ describing the detector response to produced leptons

$$\mathcal{P}(\vec{x}^{\text{R}}|\vec{\zeta}) = \int \mathcal{P}(\vec{x}^{\text{G}}|\vec{\zeta}) T(\vec{x}^{\text{R}}|\vec{x}^{\text{G}}) d\vec{x}^{\text{G}}, \quad (23)$$

where $\vec{x}' = (\vec{p}_T, Y, \Phi^*, m_1, m_2, m_{4\ell}, \vec{\Omega})$ and the superscripts R and G denote reconstruction and generator level, respectively.

It is important to model accurately the lepton momentum response and the dependence of the efficiency on p_T and η , which can all significantly affect the shape of the distributions of the eight observables used in the likelihood function. The transfer functions are constructed from the fully simulated samples for both signal and background. Because of the excellent angular resolution of the CMS tracker, for the purpose of this measurement, the effect of the resolution on the direction of each lepton is negligible compared with the effect of the momentum resolution. As a result, the effect of the direction is neglected, and only the p_T response of the leptons is modeled. It is also assumed that the detector response for each lepton is independent of the other leptons so that the transfer function can be written as a product of the transfer functions for each individual lepton. Furthermore, an overall efficiency factor to account for inefficiencies in the lepton selection requirements is applied. The transfer functions are validated by comparing the full detector simulation with the generator-level samples, where track parameters are convoluted with these functions.

The production spectrum W_{prod} in Eq. (22) is obtained empirically using simulation. The observables (\vec{p}_T, Y, Φ^*) are found to be uncorrelated to a good approximation, and their distribution is modeled as a product of three one-dimensional distributions. Then these observables are integrated out to keep the parameterization with the eight main kinematic observables \vec{x}^R . For the main background, $q\bar{q} \rightarrow ZZ/Z\gamma^*$, the four-lepton mass spectrum $m_{4\ell}$ is also modeled empirically. To construct the $m_{4\ell}$ model, the mass spectrum is parameterized with an empirical exponential function in several bins of rapidity using MC simulation. These distributions are interpolated between different bins in rapidity. The reconstructed $m_{4\ell}$ spectrum is parameterized between 115 and 135 GeV, while the generator-level spectrum is wider to model smearing into and out of this region.

There is no explicit analytic form for the differential cross section for the $Z + X$ and $gg \rightarrow ZZ/Z\gamma^*$ backgrounds. Instead, the likelihood is calculated by filling a multidimensional template histogram using very large samples of generator-level PYTHIA and MCFM events, respectively, with parton showering modeled by PYTHIA. These samples are smeared with transfer functions to account for detector effects. This approach is validated using the $q\bar{q} \rightarrow ZZ/Z\gamma^*$ analytic description and the corresponding templates, which have been confirmed to have a sufficient accuracy for the description of these backgrounds. The remaining discrepancies observed between the $Z + X$ background templates and the control regions used in the template analysis [12] are covered by assigning a corresponding systematic uncertainty. The systematic uncertainties in the lepton momentum scale and resolution are propagated using alternative parameterizations generated through variations of the transfer function for both signal and background. The sizes of these variations were determined to be consistent with the size of the lepton momentum and resolution systematic uncertainty in Ref. [12]. A systematic uncertainty in the production spectrum of the signal is included using variation of the p_T spectrum of the four-lepton system when averaging over the production spectrum. The parameterization of the $gg \rightarrow ZZ/Z\gamma^*$ and $Z + X$ background shape is varied using the alternative parameterization from the $q\bar{q} \rightarrow ZZ/Z\gamma^*$ background process.

5 Study of exotic spin-one and spin-two scenarios

The study of the exotic-spin J^P hypotheses of the observed boson with mass around 125 GeV using the $X \rightarrow ZZ$ and WW channels that have not been presented in previous publications [12, 14], is summarized in this Section. Mixed spin-one state hypotheses, as well as the spin-two models listed in Table 6 are examined. In addition, the fractional presence of J^P models of a state nearly degenerate in mass with the SM state are tested. In all cases, the template method is employed as discussed in Section 4.4. The $X \rightarrow \gamma\gamma$ decay channel is also studied in the context of the exotic spin-two scenarios and the results presented in Ref. [15] are combined with those obtained in the $X \rightarrow ZZ$ and WW channels [12, 14]. All spin-one and spin-two scenarios studied are excluded, which motivates the detailed study of the spin-zero scenario in Section 6. All studies in this paper are presented under the hypothesis of a boson mass of $m_H = 125.6$ GeV, which is the combined value in the $H \rightarrow ZZ$ and WW channels [12, 14]. The only exception is the analysis of the $X \rightarrow ZZ, WW, \text{ and } \gamma\gamma$ channels combined that is performed with the $m_H = 125.0$ GeV hypothesis, which is the combined value for the three channels [12, 14, 15]. This mass difference has little effect on the results and it is in the same range as the systematic uncertainties assigned to the energy scale in the mass reconstruction.

5.1 Exotic-spin study with the $H \rightarrow ZZ \rightarrow 4\ell$ channel

In the case of the spin-one studies, the hypothesis testing is performed for a discrete set of values of the parameter f_{b2} . The input observables are $(\mathcal{D}_{\text{bkg}}, \mathcal{D}_{1^-}, \mathcal{D}_{1^+})$. It has been demonstrated in the context of this study that the distributions of these observables are not sensitive to the phase between the b_1 and b_2 coupling parameters in Eq. (8) and therefore the results of the f_{b2} scan are valid for any value of the phase term in the interference. The spin-one hypothesis is tested for two scenarios, $q\bar{q}$ production and using only decay information. The latter requires the input observables $(\mathcal{D}_{\text{bkg}}^{\text{dec}}, \mathcal{D}_{1^-}^{\text{dec}}, \mathcal{D}_{1^+}^{\text{dec}})$.

Figure 5 (left) shows the distribution of the test statistic $q = -2 \ln(\mathcal{L}_{J^P} / \mathcal{L}_{0^+})$ for a SM Higgs boson and for the $J^P = 1^+$ hypothesis. The expected and observed separations of spin-one models from the test statistic distributions are summarized in Table 7 and in Fig. 6. The expected separation between the alternative signal hypotheses is quoted for two cases. In the first case, the expected SM Higgs boson signal strength and the alternative signal cross section are the ones obtained in the fit to the data. The second case assumes the nominal SM Higgs boson signal strength (defined as $\mu = 1$), while the cross section for the alternative signal hypothesis is taken to be the same as for the SM Higgs boson (the $2e2\mu$ channel at 8 TeV is taken as a reference). Since the observed signal strength is very close to unity, the two results for the expected separations are also similar.

Figure 5 (right) also shows an example of the likelihood scan, $-2\Delta \ln \mathcal{L}$ as a function of $f(J^P)$ for the $q\bar{q}$ produced 1^+ model, where the fractional cross section of a second overlapping but non-interfering resonance $f(J^P)$ is defined in Eq. (16). The expected and observed measurements of the non-interfering fractions are also summarized in Table 7 and in Fig. 7. The production cross section fractions are represented by $f(J^P)$ and therefore require knowledge of the reconstruction efficiency for the interpretation of the measured yields. In the case of the production independent scenarios of spin-one models, the $f(J^P)$ results are extracted using the reconstruction efficiency of the $q\bar{q} \rightarrow X$ process. The values of $-2\Delta \ln \mathcal{L} = 1$ and 3.84 represent the 68% and 95% CL, respectively.

All spin-one tests are consistent with the expectation for the SM Higgs boson. While the decay-only analysis uses less information and is expected to provide weaker constraints, the fluctuations in the observed data lead to stronger constraints for spin-one models. The least restrictive result corresponds to the 1^+ model in the $q\bar{q}$ production test with a CL_s value of 0.031%.

Any arbitrary spin-one model for the resonance observed in the $X \rightarrow ZZ \rightarrow 4\ell$ decay mode with any mixture of parity-even and parity-odd interactions and any production mechanism is excluded at a CL of 99.97% or higher.

In the case of the spin-two studies, hypothesis testing is performed for ten models and three scenarios: gg , $q\bar{q}$ production, and using only decay information. Two input observables are used since interference between the different amplitude components is not considered. Several models have been tested in Ref. [12] and here those results are repeated for completeness. They cover all the lowest order terms in the amplitude without considering mixing of different contributions.

An example distribution of the test statistic and observed value in the case of the SM Higgs boson and the spin-two hypothesis 2_{h2}^+ is shown in Fig. 8 (left). The expected and observed separation from the test statistic distributions for all the spin-two models considered is summarized in Table 8 and in Fig. 9. The 2_{h2}^+ model is the least restricted one, see Table 8: $CL_s = 0.74\%$ for any production mechanism. The observed non-interfering fraction measurements are summarized in Table 8 and in Fig. 10. In the case of production-independent scenarios the

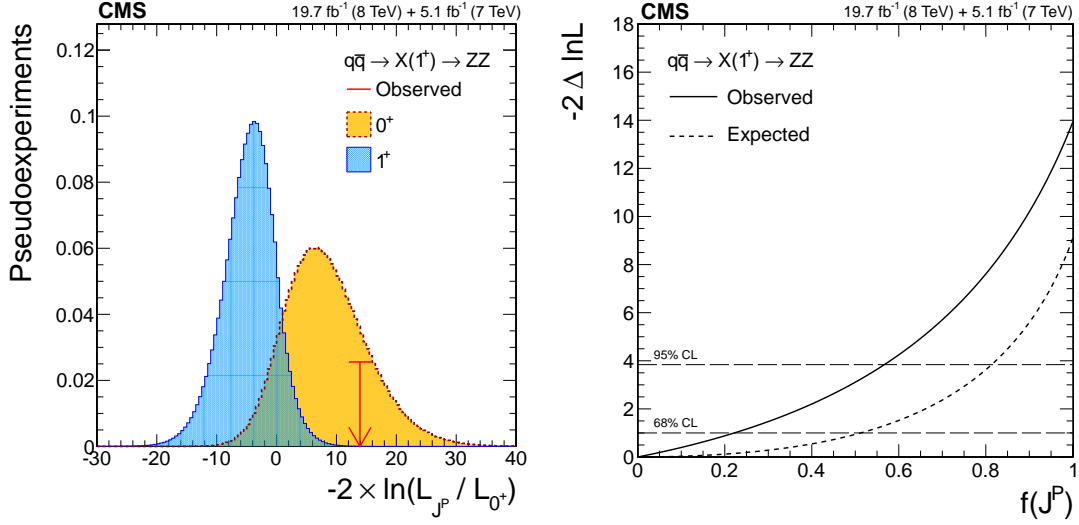


Figure 5: (left) Distributions of the test statistic $q = -2 \ln(\mathcal{L}_{J^P} / \mathcal{L}_{0^+})$ for the $J^P = 1^+$ hypothesis of $q\bar{q} \rightarrow X(1^+) \rightarrow ZZ$ tested against the SM Higgs boson hypothesis (0^+). The expectation for the SM Higgs boson is represented by the yellow histogram on the right and the alternative J^P hypothesis by the blue histogram on the left. The red arrow indicates the observed q value. (right) Observed value of $-2\Delta \ln \mathcal{L}$ as a function of $f(J^P)$ and the expectation in the SM for the $q\bar{q} \rightarrow X(1^+) \rightarrow ZZ$ alternative J^P model.

Table 7: List of spin-one models tested in the $X \rightarrow ZZ$ analysis. The expected separation is quoted for two scenarios, for the signal production cross section obtained from the fit to data for each hypothesis and using the SM expectation ($\mu = 1$). The observed separation shows the consistency of the observation with the SM Higgs boson model or the alternative J^P model, from which the CL_s value is derived. The $f(J^P)$ constraints are quoted, where the decay-only measurements are valid for any production (Prod.) mechanism and are performed using the efficiency of the $q\bar{q} \rightarrow X \rightarrow ZZ$ selection.

$f_{b2}(J^P)$	J^P	Expected	Obs. 0^+	Obs. J^P	CL_s	$f(J^P)$ 95% CL	$f(J^P)$
Model	Prod.	($\mu=1$)				Obs. (Exp.)	Best Fit
0.0(1^-)	$q\bar{q}$	2.9σ (2.8σ)	-1.4σ	$+5.0\sigma$	$<0.001\%$	<0.46 (0.78)	$0.00^{+0.16}_{-0.00}$
0.2	$q\bar{q}$	2.6σ (2.6σ)	-1.4σ	$+4.6\sigma$	0.002%	<0.49 (0.81)	$0.00^{+0.17}_{-0.00}$
0.4	$q\bar{q}$	2.5σ (2.4σ)	-1.3σ	$+4.4\sigma$	0.005%	<0.51 (0.83)	$0.00^{+0.19}_{-0.00}$
0.6	$q\bar{q}$	2.4σ (2.4σ)	-1.2σ	$+4.1\sigma$	0.015%	<0.53 (0.83)	$0.00^{+0.20}_{-0.00}$
0.8	$q\bar{q}$	2.4σ (2.4σ)	-1.0σ	$+4.0\sigma$	0.021%	<0.55 (0.83)	$0.00^{+0.21}_{-0.00}$
1.0(1^+)	$q\bar{q}$	2.4σ (2.4σ)	-0.8σ	$+3.8\sigma$	0.031%	<0.57 (0.81)	$0.00^{+0.22}_{-0.00}$
0.0(1^-)	any	2.9σ (2.7σ)	-2.0σ	$>5.0\sigma$	$<0.001\%$	<0.37 (0.79)	$0.00^{+0.12}_{-0.00}$
0.2	any	2.7σ (2.5σ)	-2.2σ	$>5.0\sigma$	$<0.001\%$	<0.38 (0.82)	$0.00^{+0.12}_{-0.00}$
0.4	any	2.5σ (2.4σ)	-2.3σ	$>5.0\sigma$	$<0.001\%$	<0.39 (0.84)	$0.00^{+0.13}_{-0.00}$
0.6	any	2.5σ (2.3σ)	-2.4σ	$>5.0\sigma$	$<0.001\%$	<0.39 (0.86)	$0.00^{+0.13}_{-0.00}$
0.8	any	2.4σ (2.3σ)	-2.3σ	$>5.0\sigma$	$<0.001\%$	<0.40 (0.86)	$0.00^{+0.13}_{-0.00}$
1.0(1^+)	any	2.5σ (2.3σ)	-2.3σ	$>5.0\sigma$	$<0.001\%$	<0.41 (0.85)	$0.00^{+0.13}_{-0.00}$

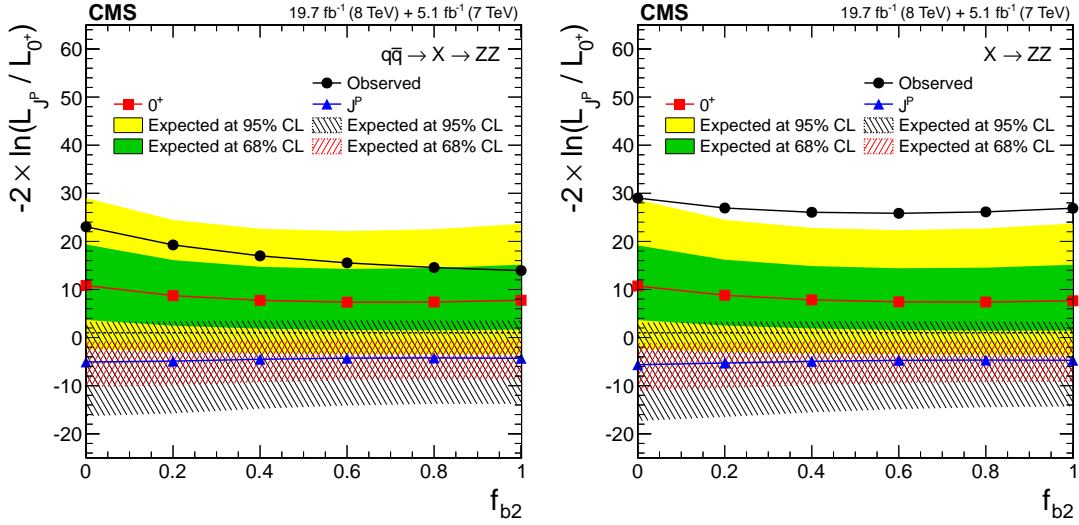


Figure 6: Distributions of the test statistic $q = -2 \ln(\mathcal{L}_{J^P} / \mathcal{L}_{0^+})$ as a function of f_{b2} for the spin-one J^P models tested against the SM Higgs boson hypothesis in the $q\bar{q} \rightarrow X \rightarrow ZZ$ (left) and decay-only $X \rightarrow ZZ$ (right) analyses. The median expectation for the SM Higgs boson is represented by the red squares with the green (68% CL) and yellow (95% CL) solid color regions and for the alternative J^P hypotheses by the blue triangles with the red (68% CL) and blue (95% CL) hatched regions. The observed values are indicated by the black dots.

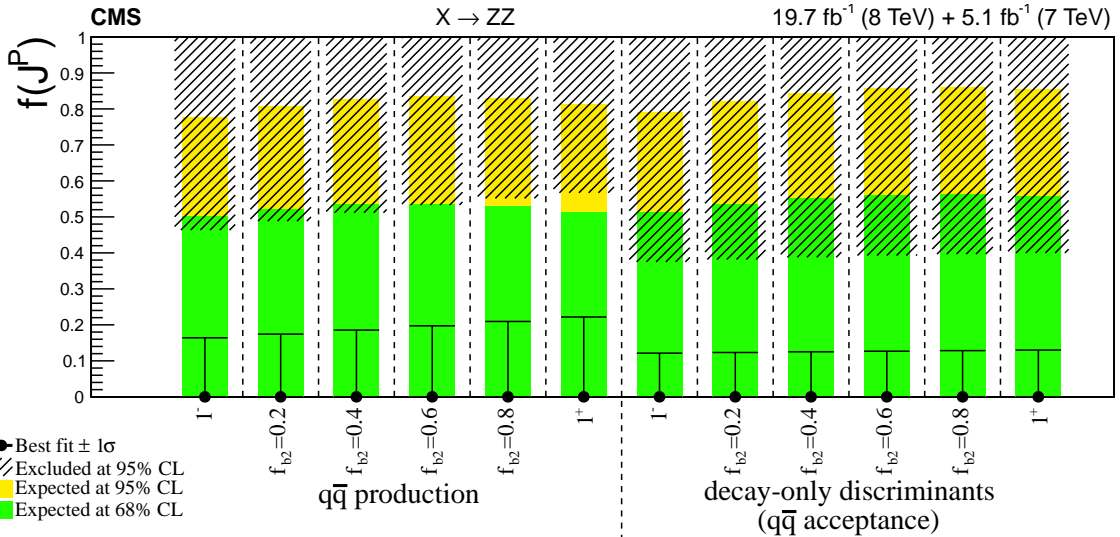


Figure 7: Summary of the $f(J^P)$ constraints as a function of f_{b2} from Table 7, where the decay-only measurements are performed using the efficiency of the $q\bar{q} \rightarrow X \rightarrow ZZ$ selection. The expected 68% and 95% CL regions are shown as green and yellow bands. The observed constraints at 68% and 95% CL are shown as the points with error bars and the excluded hatched regions.

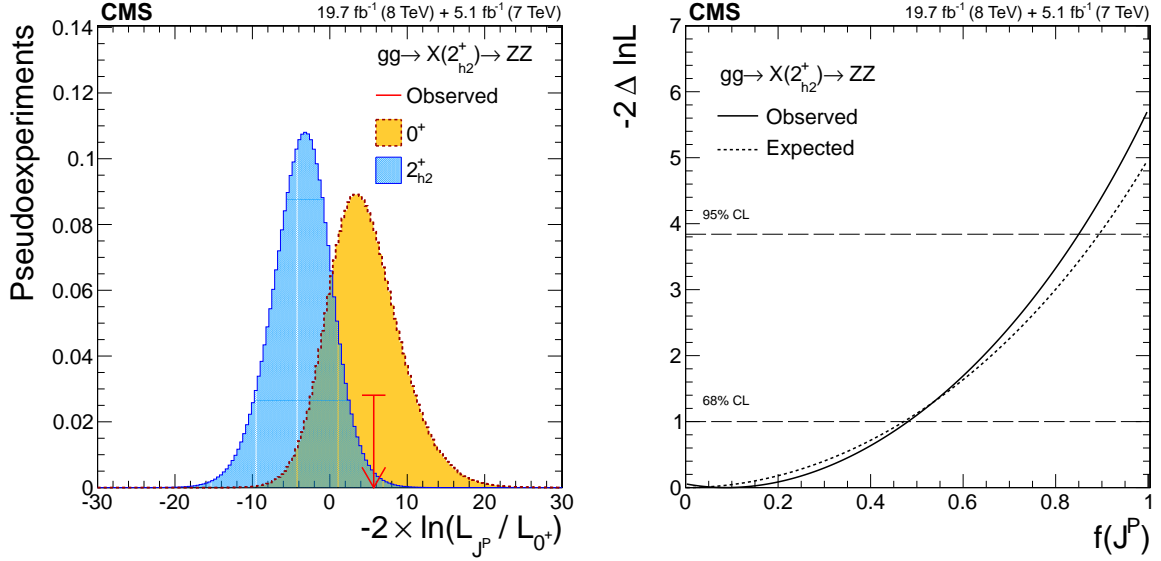


Figure 8: (left) Distributions of the test statistic $q = -2 \ln(\mathcal{L}_{J^P} / \mathcal{L}_{0^+})$ for the $J^P = 2_{h2}^+$ hypothesis of $gg \rightarrow X(2_{h2}^+) \rightarrow ZZ$ tested against the SM Higgs boson hypothesis (0^+). The expectation for the SM Higgs boson is represented by the yellow histogram on the right and the alternative J^P hypothesis by the blue histogram on the left. The red arrow indicates the observed q value. (right) Observed value of $-2\Delta \ln \mathcal{L}$ as a function of $f(J^P)$ and the expectation in the SM for the $gg \rightarrow X(2_{h2}^+) \rightarrow ZZ$ alternative J^P model.

$f(J^P)$ results are extracted using the $gg \rightarrow X$ efficiency. Figure 8 (right) shows the likelihood scan for the 2_{h2}^+ hypothesis as a function of $f(J^P)$.

The data disfavor all the spin-two $X \rightarrow ZZ \rightarrow 4\ell$ hypotheses tested in favor of the SM hypothesis $J^P = 0^+$ with $1 - CL_s$ values larger than 99% CL when only decay information is used (Table 8).

5.2 Exotic-spin study with the $H \rightarrow WW \rightarrow \ell\nu\ell\nu$ channel

Similar to the $X \rightarrow ZZ \rightarrow 4\ell$ study above, ten spin-two hypotheses, listed in Table 2, and three spin-one hypotheses, including a mixed case with $f_{b2}^{WW} = 0.5$, are tested using the $X \rightarrow WW \rightarrow \ell\nu\ell\nu$ decay. Examples of distributions of the test statistic, $q = -2 \ln(\mathcal{L}_{J^P} / \mathcal{L}_{0^+})$, for the SM Higgs boson and alternative spin-one and spin-two models are shown in Figs. 11 and 12 (left). Examples of the likelihood scans, $-2\Delta \ln \mathcal{L}$, as a function of $f(J^P)$ are also shown in Figs. 11 and 12 (right).

The expected and observed separation of the test statistic for the various models are summarized in Table 9 for spin-one and in Table 10 for spin-two. The expected separation between the SM Higgs boson and each alternative spin-one or spin-two hypothesis is larger than one standard deviation in most cases, reaching three standard deviation for several models.

The spin-one J^P hypothesis is tested against the SM Higgs boson for several values of f_{b2}^{WW} . The results are shown in Fig. 13 (left) and summarized in Table 9. As in the $X \rightarrow ZZ \rightarrow 4\ell$ study, the 1^+ model is found to be the least restricted.

The summary of the spin-two results is presented in Fig. 14 and Table 10. In the case of the spin-two studies, the results for the different scenarios are estimated assuming different production fractions from $f(q\bar{q}) = 0$, representing the pure $gg \rightarrow X$ process, to $f(q\bar{q}) = 1$, representing the pure $q\bar{q} \rightarrow X$ process. A scan of the $f(q\bar{q})$ fraction is performed in each case, with an

Table 8: List of spin-two models tested in the $X \rightarrow ZZ$ analysis. The expected separation is quoted for two scenarios, for the signal production cross section obtained from the fit to data for each hypothesis, and using the SM expectation ($\mu = 1$). The observed separation shows the consistency of the observation with the SM Higgs boson or an alternative J^P model, from which the CL_s value is derived. The $f(J^P)$ constraints are quoted, where the decay-only measurements are valid for any production (Prod.) mechanism and are performed using the efficiency of the $gg \rightarrow X \rightarrow ZZ$ selection. Results from Ref. [12] are explicitly noted.

J^P	J^P	Expected				$f(J^P)$ 95% CL	$f(J^P)$
Model	Prod.	($\mu=1$)	Obs. 0^+	Obs. J^P	CL_s	Obs. (Exp.)	Best Fit
2_m^+ [12]	gg	1.9σ (1.8σ)	-1.1σ	$+3.0\sigma$	0.90%	<0.71 (1.00)	$0.00^{+0.30}_{-0.00}$
2_{h2}^+	gg	2.0σ (2.1σ)	-0.3σ	$+2.4\sigma$	2.0%	<0.85 (0.89)	$0.09^{+0.39}_{-0.09}$
2_{h3}^+	gg	3.2σ (3.4σ)	$+0.3\sigma$	$+3.0\sigma$	0.17%	<0.72 (0.58)	$0.13^{+0.29}_{-0.13}$
2_h^+ [12]	gg	3.8σ (4.0σ)	$+1.8\sigma$	$+2.0\sigma$	2.3%	<1.00 (0.48)	$0.48^{+0.28}_{-0.29}$
2_b^+ [12]	gg	1.6σ (1.8σ)	-1.4σ	$+3.4\sigma$	0.50%	<0.64 (1.00)	$0.00^{+0.24}_{-0.00}$
2_{h6}^+	gg	3.4σ (3.7σ)	-0.6σ	$+4.9\sigma$	$<0.001\%$	<0.38 (0.58)	$0.00^{+0.13}_{-0.00}$
2_{h7}^+	gg	3.8σ (4.5σ)	-0.3σ	$+4.5\sigma$	$<0.001\%$	<0.44 (0.43)	$0.00^{+0.19}_{-0.00}$
2_h^- [12]	gg	4.2σ (4.5σ)	$+1.0\sigma$	$+3.2\sigma$	0.090%	<0.77 (0.44)	$0.29^{+0.26}_{-0.23}$
2_{h9}^-	gg	2.5σ (2.6σ)	-1.1σ	$+4.0\sigma$	0.029%	<0.46 (0.76)	$0.00^{+0.15}_{-0.00}$
2_{h10}^-	gg	4.2σ (4.3σ)	-0.1σ	$+4.8\sigma$	$<0.001\%$	<0.57 (0.50)	$0.06^{+0.27}_{-0.06}$
2_m^+ [12]	$q\bar{q}$	1.7σ (1.7σ)	-1.7σ	$+3.8\sigma$	0.17%	<0.56 (0.99)	$0.00^{+0.19}_{-0.00}$
2_{h2}^+	$q\bar{q}$	2.2σ (2.2σ)	-0.8σ	$+3.3\sigma$	0.26%	<0.61 (0.86)	$0.00^{+0.23}_{-0.00}$
2_{h3}^+	$q\bar{q}$	3.1σ (3.0σ)	$+0.2\sigma$	$+3.0\sigma$	0.21%	<0.81 (0.70)	$0.13^{+0.40}_{-0.13}$
2_h^+	$q\bar{q}$	4.0σ (3.9σ)	$+0.2\sigma$	$+3.9\sigma$	0.008%	<0.71 (0.53)	$0.21^{+0.28}_{-0.21}$
2_b^+	$q\bar{q}$	1.7σ (1.7σ)	-1.9σ	$+4.1\sigma$	0.062%	<0.45 (1.00)	$0.00^{+0.14}_{-0.00}$
2_{h6}^+	$q\bar{q}$	3.4σ (3.3σ)	-0.2σ	$+4.0\sigma$	0.008%	<0.74 (0.71)	$0.04^{+0.45}_{-0.04}$
2_{h7}^+	$q\bar{q}$	4.1σ (3.9σ)	$+0.4\sigma$	$+3.8\sigma$	0.010%	<0.77 (0.55)	$0.35^{+0.23}_{-0.28}$
2_h^-	$q\bar{q}$	4.3σ (4.4σ)	$+0.0\sigma$	$+4.6\sigma$	$<0.001\%$	<0.57 (0.48)	$0.01^{+0.31}_{-0.01}$
2_{h9}^-	$q\bar{q}$	2.4σ (2.2σ)	$+0.5\sigma$	$+2.0\sigma$	3.1%	<0.99 (0.86)	$0.31^{+0.43}_{-0.31}$
2_{h10}^-	$q\bar{q}$	4.0σ (3.9σ)	$+0.4\sigma$	$+4.0\sigma$	0.006%	<0.75 (0.59)	$0.30^{+0.26}_{-0.30}$
2_m^+ [12]	any	1.5σ (1.5σ)	-1.6σ	$+3.4\sigma$	0.71%	<0.63 (1.00)	$0.00^{+0.22}_{-0.00}$
2_{h2}^+	any	1.9σ (2.0σ)	-0.9σ	$+3.0\sigma$	0.74%	<0.66 (0.95)	$0.00^{+0.27}_{-0.00}$
2_{h3}^+	any	3.0σ (3.1σ)	$+0.0\sigma$	$+3.1\sigma$	0.18%	<0.69 (0.64)	$0.00^{+0.35}_{-0.00}$
2_h^+	any	3.8σ (4.0σ)	$+0.3\sigma$	$+3.6\sigma$	0.025%	<0.64 (0.49)	$0.07^{+0.30}_{-0.07}$
2_b^+	any	1.7σ (1.7σ)	-1.6σ	$+3.6\sigma$	0.29%	<0.55 (1.00)	$0.00^{+0.19}_{-0.00}$
2_{h6}^+	any	3.3σ (3.4σ)	-0.3σ	$+4.2\sigma$	0.003%	<0.54 (0.62)	$0.00^{+0.23}_{-0.00}$
2_{h7}^+	any	4.0σ (4.2σ)	$+0.6\sigma$	$+3.5\sigma$	0.032%	<0.70 (0.47)	$0.17^{+0.28}_{-0.17}$
2_h^-	any	4.2σ (4.6σ)	-0.2σ	$+4.8\sigma$	$<0.001\%$	<0.48 (0.43)	$0.04^{+0.21}_{-0.04}$
2_{h9}^-	any	2.2σ (2.1σ)	-0.6σ	$+2.9\sigma$	0.57%	<0.69 (0.89)	$0.00^{+0.27}_{-0.00}$
2_{h10}^-	any	3.9σ (4.0σ)	$+0.1\sigma$	$+4.3\sigma$	0.002%	<0.61 (0.54)	$0.08^{+0.30}_{-0.08}$

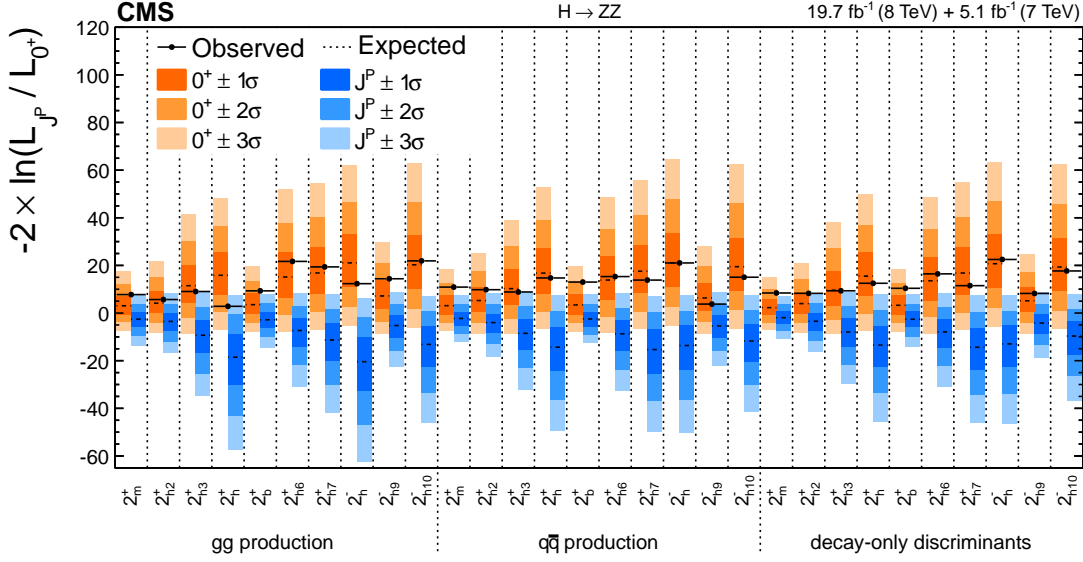


Figure 9: Distributions of the test statistic $q = -2 \ln(\mathcal{L}_{J^P} / \mathcal{L}_{0^+})$ for the spin-two J^P models tested against the SM Higgs boson hypothesis in the $X \rightarrow ZZ$ analyses. The expected median and the 68.3%, 95.4%, and 99.7% CL regions for the SM Higgs boson (orange, the left for each model) and for the alternative J^P hypotheses (blue, right) are shown. The observed q values are indicated by the black dots.

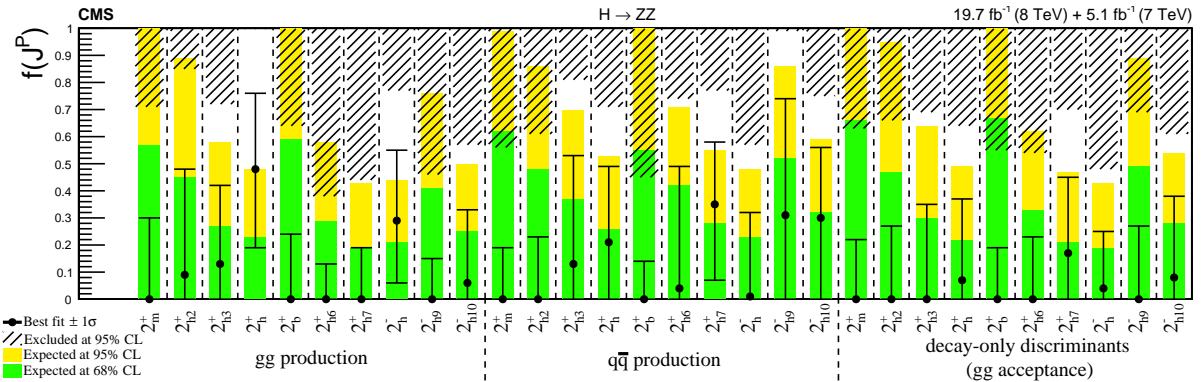


Figure 10: Summary of the $f(J^P)$ constraints for the spin-two models from Table 8, where the decay-only measurements are performed using the efficiency of the $gg \rightarrow X \rightarrow ZZ$ selection. The expected 68% and 95% CL regions are shown as the green and yellow bands. The observed constraints at 68% and 95% CL are shown as the points with error bars and the excluded hatched regions.

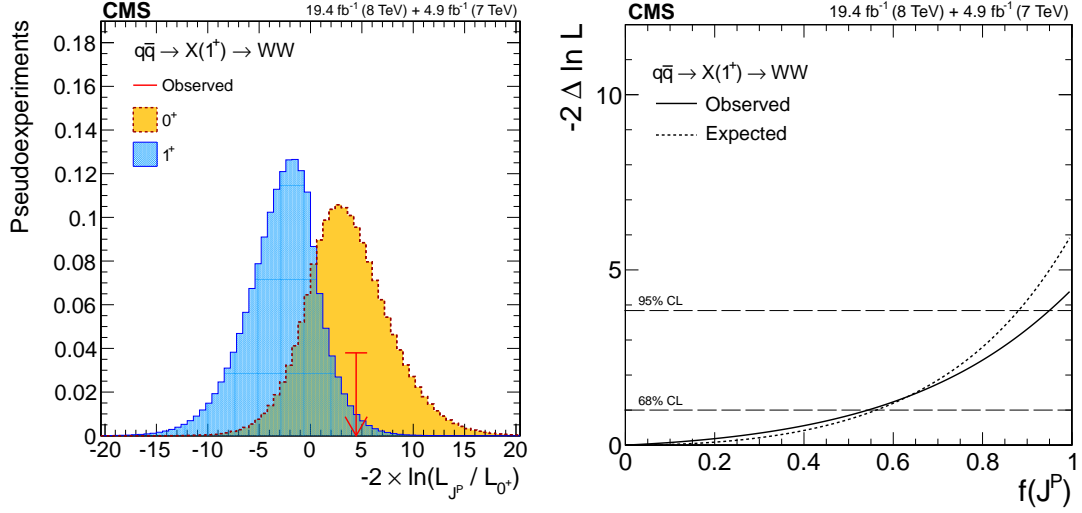


Figure 11: (left) Distributions of the test statistic $q = -2 \ln(\mathcal{L}_{J^P} / \mathcal{L}_{0^+})$ for the $J^P = 1^+$ hypothesis of $q\bar{q} \rightarrow X(1^+) \rightarrow WW$ against the SM Higgs boson hypothesis (0^+). The expectation for the SM Higgs boson is represented by the yellow histogram on the right and the alternative J^P hypothesis by the blue histogram on the left. The red arrow indicates the observed q value. (right) Observed value of $-2\Delta \ln \mathcal{L}$ as a function of $f(J^P)$ and the expectation in the SM for the $q\bar{q} \rightarrow X(1^+) \rightarrow WW$ alternative J^P model.

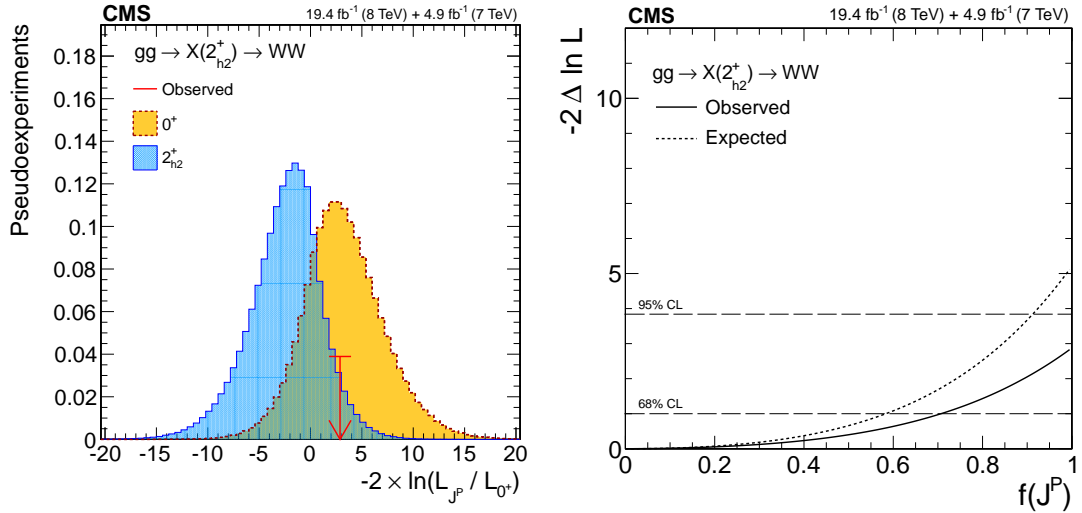


Figure 12: (left) Distributions of the test statistic $q = -2 \ln(\mathcal{L}_{J^P} / \mathcal{L}_{0^+})$ for the $J^P = 2_{h2}^+$ hypothesis of $gg \rightarrow X(2_{h2}^+) \rightarrow WW$ against the SM Higgs boson hypothesis (0^+). The expectation for the SM Higgs boson is represented by the yellow histogram on the right and the alternative J^P hypothesis by the blue histogram on the left. The red arrow indicates the observed q value. (right) Observed value of $-2\Delta \ln \mathcal{L}$ as a function of $f(J^P)$ and the expectation in the SM for the $gg \rightarrow X(2_{h2}^+) \rightarrow WW$ alternative J^P model.

Table 9: List of spin-one models tested in the $X \rightarrow WW$ analysis. The expected separation is quoted for two scenarios, for the signal production cross section obtained from the fit to data for each hypothesis, and using the SM expectation ($\mu = 1$). The observed separation shows the consistency of the observation with the SM Higgs boson model or the alternative J^P model, from which a CL_s value is derived. The constraints on the non-interfering J^P fraction are quoted in the last two columns.

$f_{b2}^{WW}(J^P)$	J^P	Expected		$f(J^P)$ 95% CL		$f(J^P)$	
Model	Prod.	($\mu=1$)	Obs. 0^+	Obs. J^P	CL_s	Obs. (Exp.)	Best Fit
0.0(1^-)	$q\bar{q}$	2.2σ (3.3σ)	-0.1σ	$+2.5\sigma$	1.5%	<0.88 (0.81)	$0.00^{+0.55}_{-0.00}$
0.5	$q\bar{q}$	2.0σ (3.0σ)	-0.2σ	$+2.2\sigma$	3.1%	<0.93 (0.86)	$0.00^{+0.57}_{-0.00}$
1.0(1^+)	$q\bar{q}$	1.8σ (2.7σ)	-0.3σ	$+2.1\sigma$	4.1%	<0.95 (0.88)	$0.00^{+0.54}_{-0.00}$

example of the scan for the 2_{h2}^+ model shown in Fig. 13 (right). The results with pure gluon fusion production $f(q\bar{q}) = 0$ are found to be the least restricted in each case. The observed non-interfering fraction measurements are summarized in Fig. 15.

In all cases the data favor the SM hypothesis over the alternative spin-one or spin-two hypotheses.

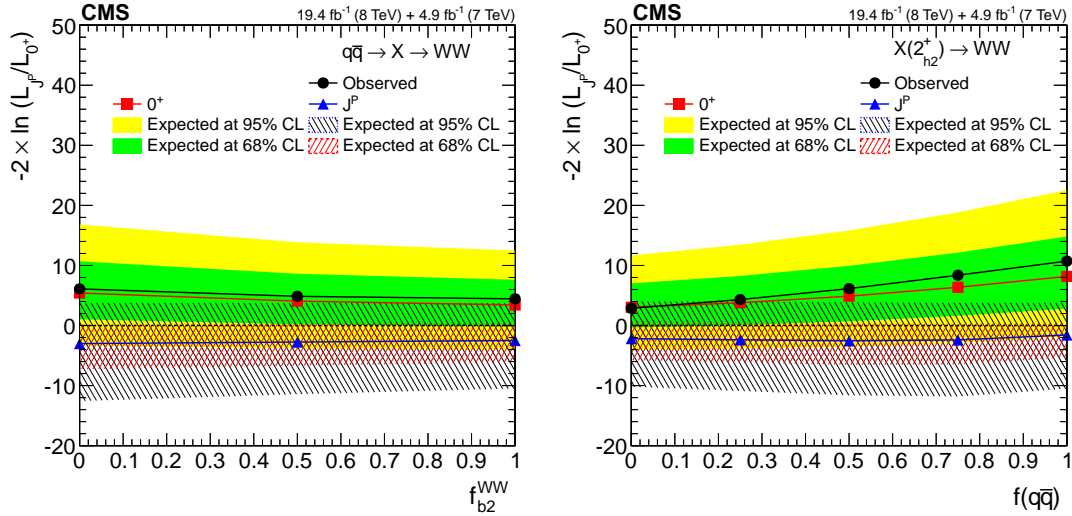


Figure 13: (left) Distributions of the test statistic $q = -2 \ln(\mathcal{L}_{J^P} / \mathcal{L}_{0^+})$ as a function of f_{b2}^{WW} for the hypothesis of the spin-one J^P models against the SM Higgs boson hypothesis in the $q\bar{q} \rightarrow X \rightarrow WW$ analysis. (right) Distribution of the test statistic $q = -2 \ln(\mathcal{L}_{J^P} / \mathcal{L}_{0^+})$ as a function of $f(q\bar{q})$ for the 2_{h2}^+ hypothesis against the SM Higgs boson hypothesis in the $H \rightarrow WW$ analysis. The median expectation for the SM Higgs boson is represented by the red squares with the green (68% CL) and yellow (95% CL) solid color regions and for the alternative J^P hypotheses by the blue triangles with the red (68% CL) and blue (95% CL) hatched regions. The observed values are indicated by the black dots.

5.3 Combined exotic-spin results with the $H \rightarrow ZZ$ and WW channels

The results of testing the spin-one and spin-two hypotheses obtained by considering the $X \rightarrow ZZ \rightarrow 4\ell$ and $X \rightarrow WW \rightarrow l\nu l\nu$ decay channels together are presented in this section. The assumption made is that the same tensor structure for the interactions appears in both XZZ and XWW couplings, as outlined for spin-two models in Table 2.

Table 10: List of spin-two models tested in the $X \rightarrow WW$ analysis. The expected separation is quoted for two scenarios, for the signal production cross section obtained from the fit to data for each hypothesis, and using the SM expectation ($\mu = 1$). The observed separation shows the consistency of the observation with the SM Higgs boson or an alternative J^P model, from which the CL_s value is derived. The constraints on the non-interfering J^P fraction are quoted in the last two columns. Results from Ref. [14] are explicitly noted.

J^P	J^P	Expected	$f(J^P)$ 95% CL				$f(J^P)$
Model	Mrod.	($\mu=1$)	Obs. 0^+	Obs. J^P	CL_s	Obs. (Exp.)	Best Fit
2_m^+ [14]	gg	1.8σ (2.9σ)	$+0.6\sigma$	$+1.2\sigma$	16%	<1.00 (0.87)	$0.50^{+0.42}_{-0.50}$
2_{h2}^+	gg	1.7σ (2.6σ)	0.0σ	$+1.6\sigma$	10%	<1.00 (0.91)	$0.00^{+0.71}_{-0.00}$
2_{h3}^+	gg	1.9σ (2.8σ)	$+0.1\sigma$	$+1.9\sigma$	5.2%	<0.99 (0.82)	$0.00^{+0.62}_{-0.00}$
2_h^+	gg	0.7σ (1.3σ)	$+0.1\sigma$	$+0.6\sigma$	52%	<1.00 (1.00)	$0.13^{+0.87}_{-0.13}$
2_b^+	gg	1.8σ (2.7σ)	$+0.1\sigma$	$+1.7\sigma$	8.6%	<1.00 (0.89)	$0.03^{+0.68}_{-0.03}$
2_{h6}^+	gg	2.5σ (3.4σ)	$+0.0\sigma$	$+2.6\sigma$	0.88%	<0.81 (0.69)	$0.00^{+0.50}_{-0.00}$
2_{h7}^+	gg	1.8σ (2.5σ)	$+0.2\sigma$	$+1.7\sigma$	8.1%	<1.00 (0.85)	$0.01^{+0.64}_{-0.01}$
2_h^-	gg	1.2σ (2.3σ)	-0.1σ	$+1.4\sigma$	19%	<1.00 (1.00)	$0.00^{+0.78}_{-0.00}$
2_{h9}^-	gg	1.4σ (2.5σ)	-0.2σ	$+1.6\sigma$	12%	<1.00 (1.00)	$0.00^{+0.66}_{-0.00}$
2_{h10}^-	gg	2.0σ (3.3σ)	$+0.4\sigma$	$+1.6\sigma$	7.8%	<1.00 (0.85)	$0.36^{+0.46}_{-0.36}$
2_m^+ [14]	$q\bar{q}$	2.7σ (3.9σ)	-0.2σ	$+3.1\sigma$	0.25%	<0.76 (0.68)	$0.00^{+0.45}_{-0.00}$
2_{h2}^+	$q\bar{q}$	2.6σ (3.7σ)	-0.4σ	$+3.3\sigma$	0.16%	<0.66 (0.70)	$0.00^{+0.32}_{-0.00}$
2_{h3}^+	$q\bar{q}$	2.3σ (3.3σ)	-0.4σ	$+2.9\sigma$	0.56%	<0.76 (0.75)	$0.00^{+0.40}_{-0.00}$
2_h^+	$q\bar{q}$	1.6σ (2.3σ)	-0.1σ	$+1.7\sigma$	8.8%	<1.00 (0.95)	$0.00^{+0.67}_{-0.00}$
2_b^+	$q\bar{q}$	2.8σ (3.8σ)	-0.2σ	$+3.2\sigma$	0.18%	<0.71 (0.68)	$0.00^{+0.38}_{-0.00}$
2_{h6}^+	$q\bar{q}$	2.8σ (3.7σ)	0.0σ	$+2.9\sigma$	0.41%	<0.80 (0.70)	$0.00^{+0.52}_{-0.00}$
2_{h7}^+	$q\bar{q}$	2.2σ (3.1σ)	-0.2σ	$+2.5\sigma$	1.6%	<0.85 (0.80)	$0.00^{+0.48}_{-0.00}$
2_h^-	$q\bar{q}$	2.0σ (2.9σ)	$+0.1\sigma$	$+1.9\sigma$	5.1%	<1.00 (0.87)	$0.01^{+0.67}_{-0.01}$
2_{h9}^-	$q\bar{q}$	2.0σ (2.9σ)	$+0.2\sigma$	$+1.8\sigma$	6.2%	<1.00 (0.86)	$0.10^{+0.64}_{-0.10}$
2_{h10}^-	$q\bar{q}$	2.6σ (3.6σ)	$+0.1\sigma$	$+2.5\sigma$	1.1%	<0.90 (0.78)	$0.07^{+0.58}_{-0.07}$

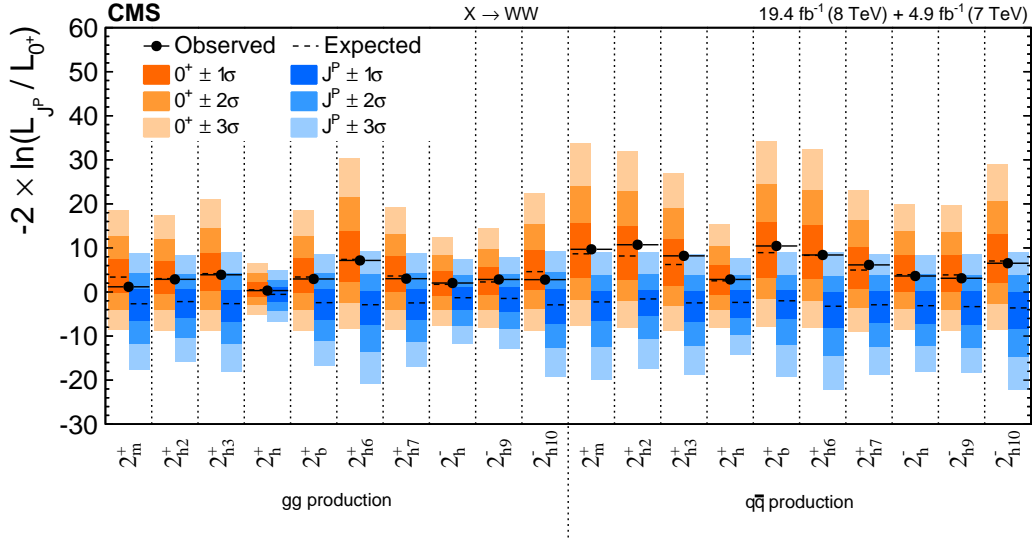


Figure 14: Distribution of the test statistic $q = -2 \ln(\mathcal{L}_{J^P} / \mathcal{L}_{0^+})$ for the spin-two J^P models tested against the SM Higgs boson hypothesis in the $X \rightarrow WW$ analyses. The expected median and the 68.3%, 95.4%, and 99.7% CL regions for the SM Higgs boson (orange, the left for each model) and for the alternative J^P hypotheses (blue, right) are shown. The observed q values are indicated by the black dots.

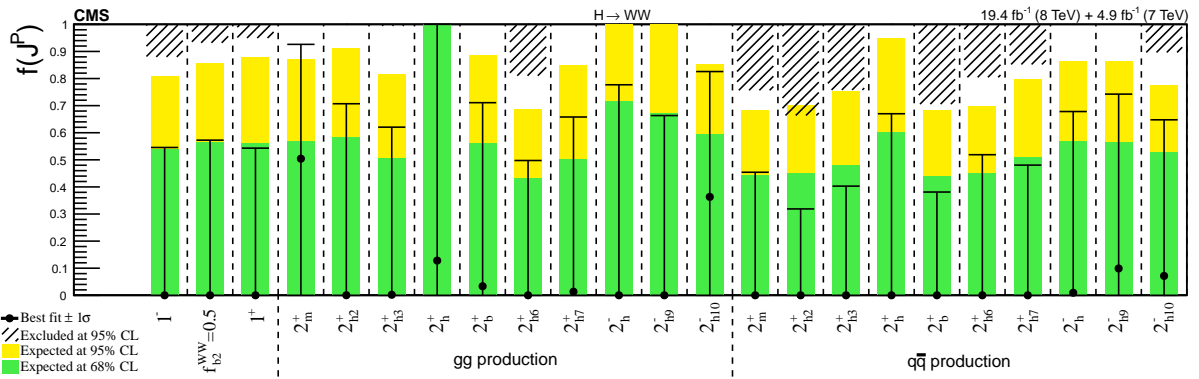


Figure 15: Summary of the $f(J^P)$ constraints for the spin-one and spin-two models from Tables 9 and 10 in the $X \rightarrow WW$ analyses. The expected 68% and 95% CL regions are shown as the green and yellow bands. The observed constraints at 68% and 95% CL are shown as the points with error bars and the excluded hatched regions.

Since only isolated tensor structure terms, and not the interference between them, are tested, the relationship between the absolute strengths of those couplings is not important and is not used in the analysis. Therefore the combined spin-one exclusion of pure 1^- and 1^+ states is tested, and for spin-two the ten hypotheses listed in Table 2 are tested. The combination of the $f(J^P)$ results is not considered here because the relative strength between the two channels is left unconstrained and the fractions remain independent measurements.

The $q\bar{q}$ production mechanism is tested for spin-one and spin-two models, and gluon fusion is tested for spin-two models. The combination of an arbitrary admixture of the $q\bar{q}$ and gluon production mechanisms is also tested. These results are based on the channels presented in Sections 5.1 and 5.2. For several of the models some production mechanisms have been tested already [11, 12, 14].

In the spin-one studies, an example of the distribution of the test statistic and observed value in the case of the SM Higgs boson along with the spin-one 1^+ hypothesis is shown in Fig. 16. The expected and observed separations from the test statistic distributions are summarized in Table 11. In the case of the spin-two studies, the distributions of the test statistic and observed value in the case of the SM Higgs boson along with the spin-two hypotheses $gg \rightarrow X(2_{h2}^+)$ and $gg \rightarrow X(2_m^+)$ are shown in Figs. 16 (right) and 17 (left). All the spin-one and spin-two models tested in the combination are summarized in Fig. 18.

The expected separations between the test statistic distributions for all the models considered are summarized in Table 11. In all cases, the expected separation between the alternative signal hypotheses is quoted for the case where the expected SM Higgs boson signal strength and the alternative signal cross sections are obtained in the fit of the data. The signal strengths in the $X \rightarrow ZZ$ and $X \rightarrow WW$ channels are fit independently. The expected separation is also quoted for the case where the events are generated with the SM expectation for the signal cross section ($\mu=1$).

These tests are performed for several choices of the ratio of the two production rates $f(q\bar{q})$. The analysis, which uses information from the $X \rightarrow ZZ \rightarrow 4\ell$ decay channel, is performed in a production-independent way, unless $f(q\bar{q}) = 0$ or 1. Part of the analysis, which is based on the $X \rightarrow WW \rightarrow \ell\nu\ell\nu$ decay channel, tests several choices of the $f(q\bar{q})$ ratio explicitly. An example of such a test is shown in Fig. 17 (right). For the combined $X \rightarrow ZZ$ and WW analysis, as in the case of the $X \rightarrow WW$ analysis, the results with gluon fusion ($f(q\bar{q}) = 0$) and with $q\bar{q}$ production ($f(q\bar{q}) = 1$) exhibit the largest and the smallest observed separation when compared to any other value in the scan of $0 < f(q\bar{q}) < 1$. The data disfavor all the spin-one and spin-two hypotheses tested in favor of the SM hypothesis $J^P = 0^+$ with $1 - CL_s$ values larger than 98% CL (Table 11).

5.4 Combined exotic-spin results with the $H \rightarrow ZZ, WW,$ and $\gamma\gamma$ channels

In this analysis, the $X \rightarrow \gamma\gamma$ decay channel is studied only in the context of the exotic spin-two 2_m^+ hypothesis. Several spin-two scenarios in Table 2 are only defined for couplings to massive vector bosons and are not defined for $X \rightarrow \gamma\gamma$. Several of the remaining higher-dimension operators in the spin-two scenario are not considered here. However, the direct model-independent analysis of the $\cos\theta^*$ distribution can be performed [15, 29]. The spin-one scenario of a resonance decaying to a two-photon final state is forbidden [67, 68], and all spin-zero scenarios have an identical isotropic two-photon distribution in the rest frame of the boson. Therefore the spin-zero and spin-one scenarios are not considered.

The individual 2_m^+ hypothesis test results in each channel were presented earlier [12, 14, 15]

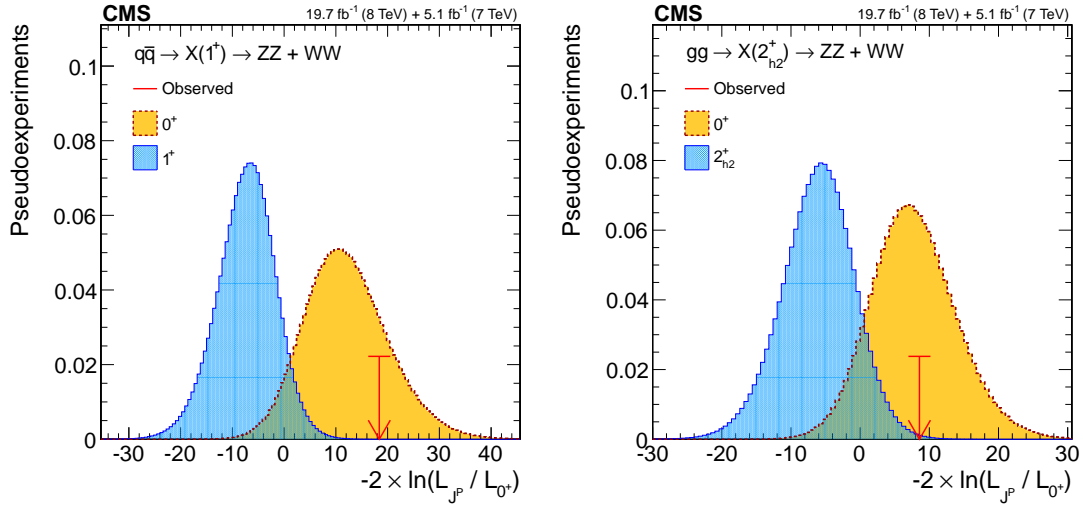


Figure 16: Distributions of the test statistic $q = -2 \ln(\mathcal{L}_{J^P} / \mathcal{L}_{0^+})$ in the combination of the $X \rightarrow ZZ$ and WW channels for the hypotheses of $q\bar{q} \rightarrow X(1^+)$ (left) and $gg \rightarrow X(2_{h2}^+)$ (right) tested against the SM Higgs boson hypothesis. The expectation for the SM Higgs boson is represented by the yellow histogram on the right of each plot and the alternative J^P hypothesis by the blue histogram on the left. The red arrow indicates the observed q value.

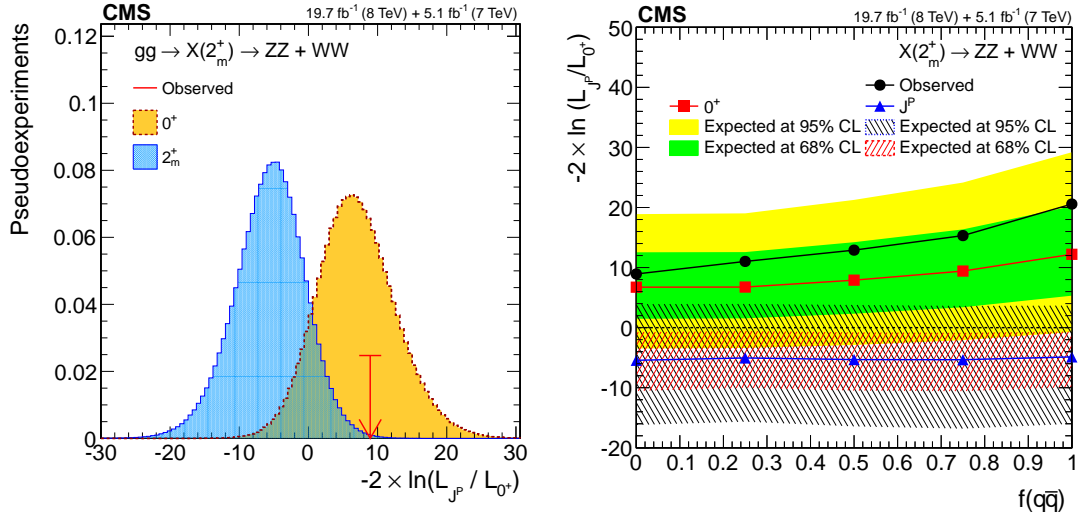


Figure 17: (left) Distributions of the test statistic $q = -2 \ln(\mathcal{L}_{J^P} / \mathcal{L}_{0^+})$ in the combination of the $X \rightarrow ZZ$ and WW channels for the hypothesis of $gg \rightarrow X(2_m^+)$ tested against the SM Higgs boson hypothesis. The expectation for the SM Higgs boson is represented by the yellow histogram on the right and the alternative J^P hypothesis by the blue histogram on the left. The red arrow indicates the observed q value. (right) Distribution of q as a function of $f(q\bar{q})$ for the 2_m^+ hypothesis against the SM Higgs boson hypothesis in the $X \rightarrow ZZ$ and WW channels. The median expectation for the SM Higgs boson is represented with the solid green (68% CL) and yellow (95% CL) regions. The alternative 2_m^+ hypotheses are represented by the blue triangles with the red (68% CL) and blue (95% CL) hatched regions. The observed values are indicated by the black dots.

Table 11: List of spin-one and spin-two models tested in the combination of the $X \rightarrow ZZ$ and $X \rightarrow WW$ channels. The combined expected separation is quoted for two scenarios, for the signal production cross section obtained from the fit to data for each hypothesis and using the SM expectation ($\mu = 1$). For comparison, the former expectations are also quoted for the individual channels as in Tables 7-10. The observed separation shows the consistency of the observation with the SM Higgs boson model or an alternative J^P model, from which the CL_s value is derived.

J^P Model	J^P Prod.	Expected $X \rightarrow ZZ$	Expected $X \rightarrow WW$	Expected ($\mu=1$)	Obs. 0^+	Obs. J^P	CL_s
1^-	$q\bar{q}$	2.9σ	2.2σ	$3.6\sigma (4.6\sigma)$	-1.2σ	$+4.9\sigma$	$<0.001\%$
1^+	$q\bar{q}$	2.4σ	1.8σ	$3.0\sigma (3.8\sigma)$	-0.8σ	$+4.3\sigma$	0.004%
2_m^+	gg	1.9σ	1.8σ	$2.4\sigma (3.4\sigma)$	-0.4σ	$+2.9\sigma$	0.53%
2_{h2}^+	gg	2.0σ	1.7σ	$2.5\sigma (3.3\sigma)$	-0.2σ	$+2.8\sigma$	0.52%
2_{h3}^+	gg	3.2σ	1.6σ	$3.7\sigma (4.3\sigma)$	$+0.4\sigma$	$+3.5\sigma$	0.031%
2_h^+	gg	3.8σ	0.7σ	$3.8\sigma (4.2\sigma)$	$+1.7\sigma$	$+2.1\sigma$	1.9%
2_b^+	gg	1.6σ	1.8σ	$2.4\sigma (3.2\sigma)$	-0.9σ	$+3.4\sigma$	0.16%
2_{h6}^+	gg	3.4σ	2.5σ	$4.2\sigma (4.9\sigma)$	-0.5σ	$>5\sigma$	$<0.001\%$
2_{h7}^+	gg	3.8σ	1.8σ	$4.2\sigma (5.0\sigma)$	-0.1σ	$+4.7\sigma$	$<0.001\%$
2_h^-	gg	4.2σ	1.2σ	$4.3\sigma (5.0\sigma)$	$+1.0\sigma$	$+3.4\sigma$	0.039%
2_{h9}^-	gg	2.5σ	1.4σ	$2.8\sigma (3.5\sigma)$	-1.0σ	$+4.2\sigma$	0.009%
2_{h10}^-	gg	4.2σ	2.0σ	$4.6\sigma (5.3\sigma)$	$+0.1\sigma$	$+4.9\sigma$	$<0.001\%$
2_m^+	$q\bar{q}$	1.7σ	2.7σ	$3.1\sigma (4.3\sigma)$	-1.0σ	$+4.5\sigma$	0.002%
2_{h2}^+	$q\bar{q}$	2.2σ	2.6σ	$3.3\sigma (4.3\sigma)$	-0.8σ	$+4.4\sigma$	0.002%
2_{h3}^+	$q\bar{q}$	3.1σ	2.6σ	$3.8\sigma (4.5\sigma)$	0.0σ	$+4.1\sigma$	0.005%
2_h^+	$q\bar{q}$	4.0σ	1.6σ	$4.3\sigma (4.5\sigma)$	$+0.2\sigma$	$+4.3\sigma$	0.002%
2_b^+	$q\bar{q}$	1.7σ	2.8σ	$3.1\sigma (4.2\sigma)$	-1.3σ	$+4.8\sigma$	$<0.001\%$
2_{h6}^+	$q\bar{q}$	3.4σ	2.8σ	$4.3\sigma (5.0\sigma)$	-0.1σ	$+4.8\sigma$	$<0.001\%$
2_{h7}^+	$q\bar{q}$	4.1σ	2.2σ	$4.6\sigma (5.0\sigma)$	$+0.3\sigma$	$+4.5\sigma$	$<0.001\%$
2_h^-	$q\bar{q}$	4.3σ	2.0σ	$4.7\sigma (5.2\sigma)$	$+0.1\sigma$	$+5.0\sigma$	$<0.001\%$
2_{h9}^-	$q\bar{q}$	2.4σ	2.0σ	$3.1\sigma (3.8\sigma)$	$+0.5\sigma$	$+2.7\sigma$	0.55%
2_{h10}^-	$q\bar{q}$	4.0σ	2.6σ	$4.7\sigma (5.3\sigma)$	$+0.5\sigma$	$+4.6\sigma$	$<0.001\%$

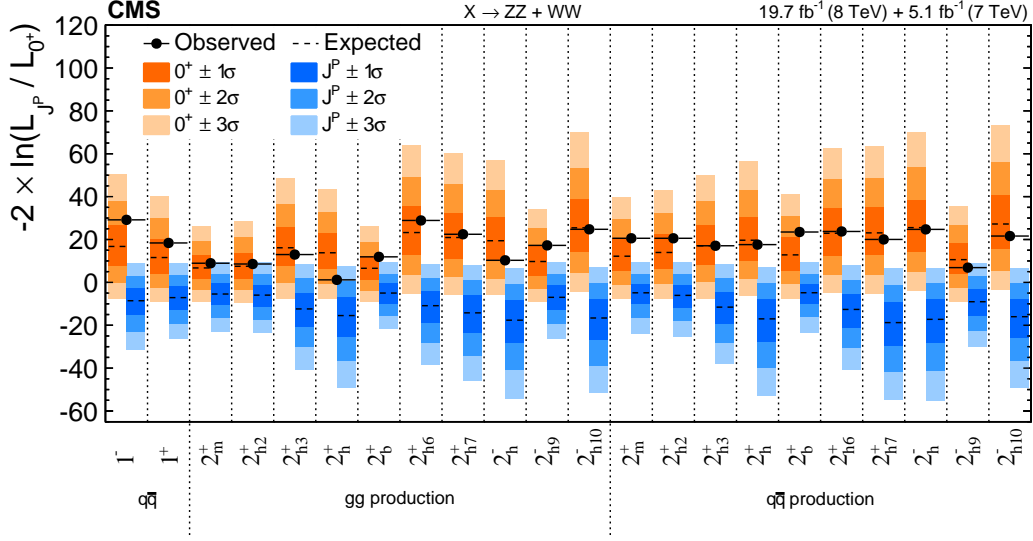


Figure 18: Distributions of the test statistic $q = -2 \ln(\mathcal{L}_{J^P} / \mathcal{L}_{0^+})$ for the spin-one and spin-two J^P models tested against the SM Higgs boson hypothesis in the combined $X \rightarrow ZZ$ and WW analyses. The expected median and the 68.3%, 95.4%, and 99.7% CL regions for the SM Higgs boson (orange, the left for each model) and for the alternative J^P hypotheses (blue, right) are shown. The observed q values are indicated by the black dots.

and the combined results are shown in Table 12. In Fig. 19 examples of the test statistic, $q = -2 \ln(\mathcal{L}_{J^P} / \mathcal{L}_{0^+})$, are shown for various fractions of the $q\bar{q}$ production mechanism $f(q\bar{q})$. As a result, the 2_m^+ model is excluded with a 99.87% CL or higher for any combination of the gg and $q\bar{q}$ production mechanisms.

Table 12: Results of the study of the 2_m^+ model for the combination of the $X \rightarrow ZZ$, WW , and $\gamma\gamma$ decay channels. The expected separation is quoted for the three channels separately and for the combination with the signal strength for each hypothesis determined from the fit to data independently in each channel. Also shown in parentheses is the expectation with the SM signal cross section ($\mu=1$). The observed separation shows the consistency of the observation with the SM 0^+ model or J^P model and corresponds to the scenario where the signal strength is floated in the fit to data.

J^P Model	J^P Prod.	Expected X \rightarrow ZZ	Expected X \rightarrow WW	Expected X \rightarrow $\gamma\gamma$	Expected ($\mu=1$)	Obs. 0^+	Obs. J^P	CL_s
2_m^+	gg	1.9σ	1.8σ	1.6σ	3.0σ (3.7σ)	-0.2σ	$+3.3\sigma$	0.13%
2_m^+	$q\bar{q}$	1.7σ	2.7σ	1.2σ	3.3σ (4.4σ)	-0.9σ	$+4.7\sigma$	0.001%

6 Study of spin-zero HVV couplings

Given the exclusion of the exotic spin-one and spin-two scenarios presented in Section 5, detailed studies of HVV interactions under the assumption that the new boson is a spin-zero resonance are performed. The results are obtained following the techniques presented in Section 4.

First, constraints are applied on the presence of only one anomalous term in the HVV amplitude where the couplings are considered to be real. A summary of such results is presented in Table 13 and Fig. 20. The details of these and other measurements are presented in the following subsections, with further measurements considering simultaneously up to four fractions

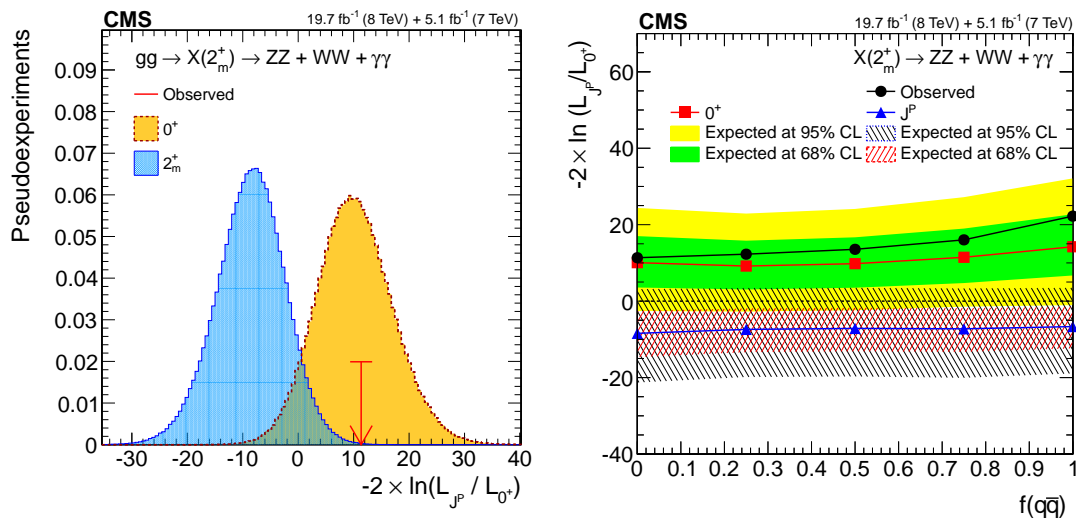


Figure 19: (left) Distributions of the test statistic $q = -2 \ln(\mathcal{L}_{J^P} / \mathcal{L}_{0^+})$ in the combination of the $X \rightarrow ZZ, WW$, and $\gamma\gamma$ channels for the hypothesis of $gg \rightarrow X(2_m^+)$ tested against the SM Higgs boson hypothesis (0^+). The expectation for the SM Higgs boson is represented by the yellow histogram on the right and the alternative J^P hypothesis by the blue histogram on the left. The red arrow indicates the observed q value. (right) Distributions of the test statistic $q = -2 \ln(\mathcal{L}_{J^P} / \mathcal{L}_{0^+})$ as a function of $f(q\bar{q})$ for the hypotheses of the 2_m^+ model tested against the SM Higgs boson hypothesis in the $X \rightarrow ZZ, WW$, and $\gamma\gamma$ channels. The median expectation for the SM Higgs boson is represented with the solid green (68% CL) and yellow (95% CL) regions. The alternative 2_m^+ hypotheses are represented by the blue triangles with the red (68% CL) and blue (95% CL) hatched regions. The observed values are indicated by the black dots.

and phase parameters in several cases. The combination of the HZZ and HWW coupling measurements provides further constraints on the HVV interactions. All results are obtained with the template method, and the f_{a2} and f_{a3} measurements in HZZ interactions are also validated with the multidimensional distribution method.

Table 13: Summary of allowed 68% CL (central values with uncertainties) and 95% CL (ranges in square brackets) intervals on anomalous coupling parameters in HVV interactions under the assumption that all the coupling ratios are real ($\phi_{ai}^{\text{VV}} = 0$ or π). The ranges are truncated at the physical boundaries of $f_{ai}^{\text{VV}} = 1$. The last column indicates the observed (expected) confidence level of a pure anomalous coupling corresponding to $f_{ai}^{\text{VV}} = 1$ when compared to the SM expectation $f_{ai}^{\text{VV}} = 0$. The expected results are quoted for the SM signal production cross section ($\mu = 1$). The results are obtained with the template method.

Parameter	Observed	Expected	$f_{ai}^{\text{VV}} = 1$
$f_{\Lambda 1} \cos(\phi_{\Lambda 1})$	$0.22^{+0.10}_{-0.16} [-0.25, 0.37]$	$0.00^{+0.16}_{-0.87} [-1.00, 0.27]$ $\cup [0.92, 1.00]$	1.1% (16%)
$f_{a2} \cos(\phi_{a2})$	$0.00^{+0.41}_{-0.06} [-0.66, -0.57]$ $\cup [-0.15, 1.00]$	$0.00^{+0.38}_{-0.08} [-0.18, 1.00]$	5.2% (5.0%)
$f_{a3} \cos(\phi_{a3})$	$0.00^{+0.14}_{-0.11} [-0.40, 0.43]$	$0.00^{+0.33}_{-0.33} [-0.70, 0.70]$	0.02% (0.41%)
$f_{\Lambda 1}^{\text{WW}} \cos(\phi_{\Lambda 1}^{\text{WW}})$	$0.21^{+0.18}_{-1.21} [-1.00, 1.00]$	$0.00^{+0.34}_{-1.00} [-1.00, 0.41]$ $\cup [0.49, 1.00]$	78% (67%)
$f_{a2}^{\text{WW}} \cos(\phi_{a2}^{\text{WW}})$	$-0.02^{+1.02}_{-0.16} [-1.00, -0.54]$ $\cup [-0.29, 1.00]$	$0.00^{+1.00}_{-0.12} [-1.00, -0.58]$ $\cup [-0.22, 1.00]$	42% (46%)
$f_{a3}^{\text{WW}} \cos(\phi_{a3}^{\text{WW}})$	$-0.03^{+1.03}_{-0.97} [-1.00, 1.00]$	$0.00^{+1.00}_{-1.00} [-1.00, 1.00]$	34% (49%)
$f_{\Lambda 1}^{\text{Z}\gamma} \cos(\phi_{\Lambda 1}^{\text{Z}\gamma})$	$-0.27^{+0.34}_{-0.49} [-1.00, 1.00]$	$0.00^{+0.83}_{-0.53} [-1.00, 1.00]$	26% (16%)
$f_{a2}^{\text{Z}\gamma} \cos(\phi_{a2}^{\text{Z}\gamma})$	$0.00^{+0.14}_{-0.20} [-0.49, 0.46]$	$0.00^{+0.51}_{-0.51} [-0.78, 0.79]$	<0.01% (0.01%)
$f_{a3}^{\text{Z}\gamma} \cos(\phi_{a3}^{\text{Z}\gamma})$	$0.02^{+0.21}_{-0.13} [-0.40, 0.51]$	$0.00^{+0.51}_{-0.51} [-0.75, 0.75]$	<0.01% (<0.01%)
$f_{a2}^{\gamma\gamma} \cos(\phi_{a2}^{\gamma\gamma})$	$0.12^{+0.20}_{-0.11} [-0.04, +0.51]$	$0.00^{+0.11}_{-0.09} [-0.32, 0.34]$	<0.01% (<0.01%)
$f_{a3}^{\gamma\gamma} \cos(\phi_{a3}^{\gamma\gamma})$	$-0.02^{+0.06}_{-0.13} [-0.35, 0.32]$	$0.00^{+0.15}_{-0.11} [-0.37, 0.40]$	<0.01% (<0.01%)

6.1 Study of HZZ couplings with the $H \rightarrow ZZ \rightarrow 4\ell$ channel

The study of the anomalous HVV couplings starts with the test of three contributions to the HZZ interaction as shown in Eq. (1). Only real couplings are considered in this test, $\phi_{ai} = 0$ or π , where ϕ_{ai} generically refers to the phase of the coupling in question, such as $\phi_{\Lambda 1}$, ϕ_{a2} , or ϕ_{a3} . Since the expansion of terms in Eq. (1) is considered for small anomalous contributions, all other parameters are set to zero when the anomalous couplings of interest are considered. These constraints of real couplings and zero contribution from other terms are relaxed in further tests discussed below. In the template approach, the three sets of observables in each fit are given in Table 6. The only exception is in the $f_{\Lambda 1}$ measurement, where the usual interference discriminant does not provide additional information and instead the third observable is \mathcal{D}_{0h+} to minimize the number of configurations also used for other studies. Since \mathcal{D}_{0h+} does not bring additional information for this measurement, it is not reflected in Table 6.

The results of the likelihood function scan for the three parameters, $f_{ai} \cos \phi_{ai}$, are shown in Fig. 21 (left), where the $\cos \phi_{ai}$ term allows for a signed quantity with $\cos \phi_{ai} = -1$ or $+1$. The 68% and 95% CL intervals are shown in Table 13. Using the transformation in Eq. (5), these

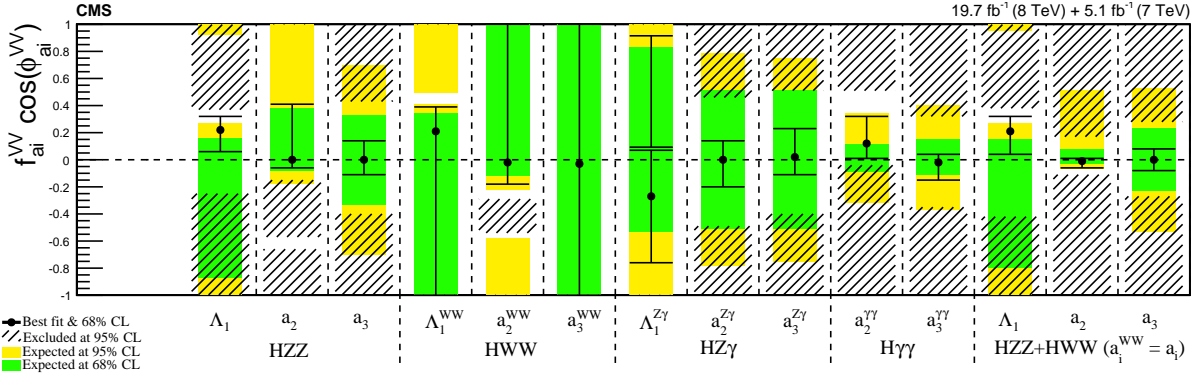


Figure 20: Summary of allowed confidence level intervals on anomalous coupling parameters in HVV interactions under the assumption that all the coupling ratios are real ($\phi_{ai}^{VV} = 0$ or π). The expected 68% and 95% CL regions are shown as the green and yellow bands. The observed constraints at 68% and 95% CL are shown as the points with errors and the excluded hatched regions. In the case of the $f_{\Lambda 1}^{Z\gamma}$ measurement, there are two minima and two 68% CL intervals, while only one global minimum is indicated with a point. The combination of the HZZ and HWW measurements is presented, assuming the symmetry $a_i = a_i^{WW}$, including $R_{ai} = 0.5$.

results can be interpreted for the coupling parameters used in Eq. (1), as shown in Table 14. Strong destructive interference of the SM and anomalous contributions at $f_{\Lambda 1} \cos(\phi_{\Lambda 1}) \sim +0.5$ or $f_{a 2} \cos(\phi_{a 2}) \sim -0.5$ leads to very different kinematic distributions and exclusions with high confidence levels. Additional features with multiple likelihood function maxima observed in the $f_{\Lambda 1}$ likelihood scan are due to the superposition of measurements in the $4e/4\mu$ and $2e2\mu$ channels, which have different maxima due to the interference between the leptons.

Next, two parameters f_{ai} and ϕ_{ai} are considered at the same time. For example, if the coupling is known to be either positive or negative, such a scenario is considered in Table 15. In this case, constraints are set on f_{ai} for a given phase value. More generally, one can allow ϕ_{ai} to be unconstrained, that is, to have any value between $-\pi$ and $+\pi$ with a generally complex coupling. Such a fit is performed for $f_{\Lambda 1}$ and $f_{a 2}$ using the same configuration, but with additional $\phi_{\Lambda 1}$ and $\phi_{a 2}$ parameters in Eq. (21). The results with ϕ_{ai} unconstrained (any) are shown in Table 15 as well. The $f_{a 3}$ measurement with $\phi_{a 3}$ unconstrained is performed with a different technique and is presented in Ref. [12], where the \mathcal{D}_{CP} observable is removed from the fit and the result becomes insensitive to the phase of the amplitude. This technique is adopted due to its simpler implementation and equivalent performance.

The next step in generalizing the constraints is to consider two anomalous contributions at the same time, both with and without the constraints that the couplings are real. Therefore, up to four parameters are considered at the same time: f_{ai} , ϕ_{ai} , f_{aj} , and ϕ_{aj} . Constraints on one parameter, when other parameters are left unconstrained in the full allowed parameter space, with $0 \leq f_{ai} \leq 1$, are presented in Table 15. Even though the expansion with only three anomalous contributions in Eq. (1) becomes incomplete when large values of $f_{ai} \sim 1$ are considered, this is still a valuable test of the consistency of the data with the SM. All of the above results, with phases fixed or unconstrained and with other anomalous couplings unconstrained are shown in Fig. 21 (right). Some observed f_{ai} constraints appear to be tighter when compared to the one-parameter fits shown in Fig. 21 (left). This happens because the values of other profiled parameters are away from the SM expectation at the minimum of $-2 \ln \mathcal{L}$, though still consistent with the SM. The expected constraints are always weaker with additional free parameters.

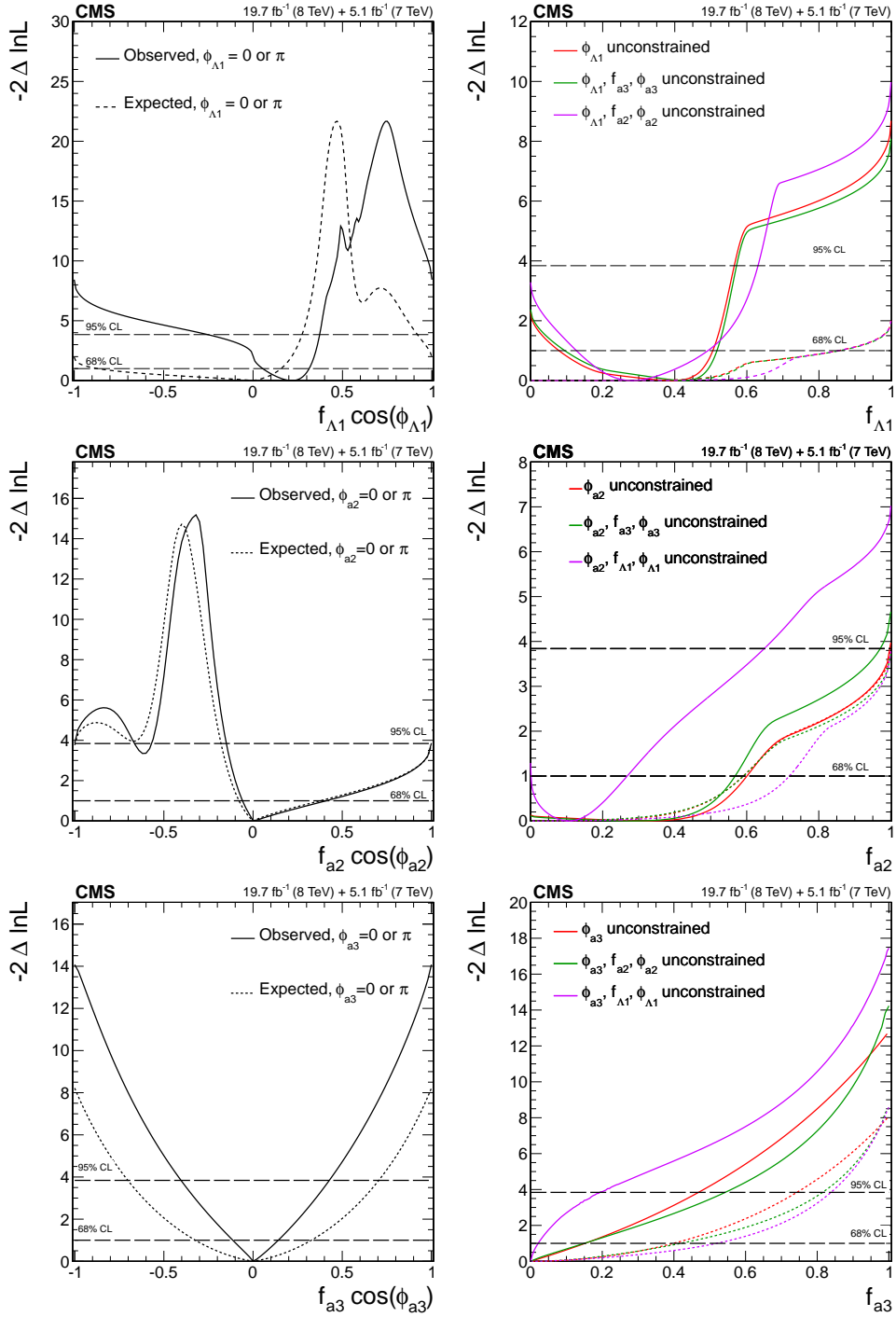


Figure 21: Expected (dashed) and observed (solid) likelihood scans using the template method for the effective fractions $f_{\Lambda 1}$, $f_{a 2}$, $f_{a 3}$ (from top to bottom) describing HZZ interactions. Plots on the left show the results when the couplings studied are constrained to be real and all other couplings are fixed to the SM predictions. The $\cos \phi_{ai}$ term allows a signed quantity where $\cos \phi_{ai} = -1$ or $+1$. Plots on the right show the results where the phases of the anomalous couplings and additional HZZ couplings are left unconstrained, as indicated in the legend. The $f_{a 3}$ result with $\phi_{a 3}$ unconstrained (in the bottom-right plot) is from Ref. [12].

Table 14: Summary of the allowed 95% CL intervals on the anomalous couplings in HZZ interactions using results in Table 13. The coupling ratios are assumed to be real (including $\cos(\phi_{\Lambda_1}) = 0$ or π).

Parameter	Observed	Expected
$(\Lambda_1 \sqrt{ a_1 }) \cos(\phi_{\Lambda_1})$	$[-\infty, -119 \text{ GeV}] \cup [104 \text{ GeV}, \infty]$	$[-\infty, 50 \text{ GeV}] \cup [116 \text{ GeV}, \infty]$
a_2/a_1	$[-2.28, -1.88] \cup [-0.69, \infty]$	$[-0.77, \infty]$
a_3/a_1	$[-2.05, 2.19]$	$[-3.85, 3.85]$

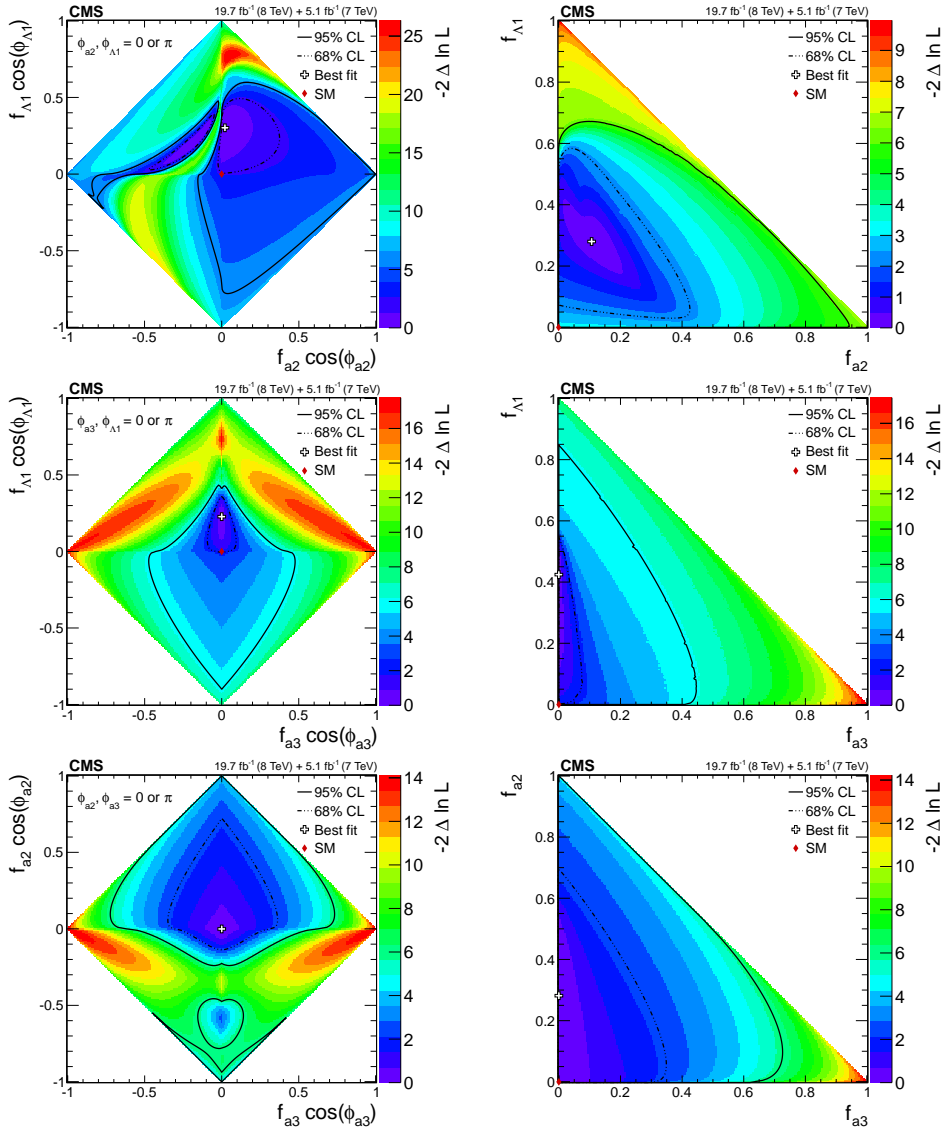


Figure 22: Observed likelihood scans using the template method for pairs of effective fractions f_{Λ_1} vs. f_{a2} , f_{Λ_1} vs. f_{a3} , and f_{a2} vs. f_{a3} (from top to bottom) describing HZZ interactions. Plots on the left show the results when the couplings studied are constrained to be real and all other couplings are fixed to the SM predictions. Plots on the right show the results when the phases of the anomalous couplings are left unconstrained. The SM expectations correspond to points (0,0) and the best fit values are shown with the crosses. The confidence level intervals are indicated by the corresponding $-2 \Delta \ln \mathcal{L}$ contours.

The above one-parameter measurements, with other couplings also considered to be unconstrained, are obtained from the fit configurations used for the two-parameter measurements shown in Fig. 22. Both options are considered, either with or without the assumption that the couplings are real. To keep the number of observables to the maximum of three, in the template approach, the following discriminants are used to set the constraints, $(\mathcal{D}_{\text{bkg}}, \mathcal{D}_{\Lambda 1}, \mathcal{D}_{0h+})$, $(\mathcal{D}_{\text{bkg}}, \mathcal{D}_{\Lambda 1}, \mathcal{D}_{0-})$, and $(\mathcal{D}_{\text{bkg}}, \mathcal{D}_{0-}$ or $\mathcal{D}_{0h+})$, for the measurements of $f_{\Lambda 1}$ vs. f_{a2} , $f_{\Lambda 1}$ vs. f_{a3} , and f_{a2} vs. f_{a3} , respectively. The left set of plots in Fig. 22 shows constraints on two real couplings, and the right set of plots in Fig. 22 shows constraints on two couplings that are allowed to have any complex phase. Similarly to the one-parameter constraints, the allowed 95% CL regions are formally defined using the profile likelihood function ($-2\Delta \ln \mathcal{L} = 5.99$). The results in Table 15 are obtained from these two-parameter likelihood scans by profiling one parameter.

Overall, all anomalous HZZ couplings are found to be consistent with zero, which is also consistent with the expectation from the SM where these couplings are expected to be very small, well below the current sensitivity.

Table 15: Summary of the allowed 68% CL (central values with uncertainties) and 95% CL (ranges in square brackets) intervals on anomalous coupling parameters in the HZZ interactions under the condition of a given phase of the coupling (0 or π) or when the phase or other parameters are unconstrained (any value allowed). Results are presented with the template method and expectations are quoted in parentheses following the observed values. The results for f_{a3} with ϕ_{a3} unconstrained are from Ref. [12].

Measurement	$f_{\Lambda 1}$	f_{a2}	f_{a3}
$\phi_{ai} = 0$	$0.22^{+0.10}_{-0.16}$ [0.00, 0.37] ($0.00^{+0.16}_{-0.00}$ [0.00, 0.27] \cup [0.92, 1.00])	$0.00^{+0.42}_{-0.00}$ [0.00, 1.00] ($0.00^{+0.35}_{-0.00}$ [0.00, 1.00])	$0.00^{+0.14}_{-0.00}$ [0.00, 0.43] ($0.00^{+0.33}_{-0.00}$ [0.00, 0.70])
$\phi_{ai} = \pi$	$0.00^{+0.08}_{-0.00}$ [0.00, 0.82] ($0.00^{+0.87}_{-0.00}$ [0.00, 1.00])	$0.00^{+0.06}_{-0.00}$ [0.00, 0.15] \cup [0.56, 0.68] ($0.00^{+0.08}_{-0.00}$ [0.00, 0.18] \cup [0.62, 0.73])	$0.00^{+0.11}_{-0.00}$ [0.00, 0.40] ($0.00^{+0.32}_{-0.00}$ [0.00, 0.70])
any ϕ_{ai}	$0.39^{+0.16}_{-0.31}$ [0.00, 0.57] ($0.00^{+0.85}_{-0.00}$ [0.00, 1.00])	$0.32^{+0.28}_{-0.32}$ [0.00, 1.00] ($0.00^{+0.59}_{-0.00}$ [0.00, 1.00])	$0.00^{+0.17}_{-0.00}$ [0.00, 0.47] ($0.00^{+0.40}_{-0.00}$ [0.00, 0.74])
any $\phi_{ai}, f_{\Lambda 1}, \phi_{\Lambda 1}$		$0.11^{+0.16}_{-0.11}$ [0.00, 0.65] ($0.00^{+0.72}_{-0.00}$ [0.00, 1.00])	$0.00^{+0.02}_{-0.00}$ [0.00, 0.19] ($0.00^{+0.52}_{-0.00}$ [0.00, 0.84])
any $\phi_{ai}, f_{a2}, \phi_{a2}$	$0.28^{+0.21}_{-0.15}$ [0.00, 0.63] ($0.00^{+0.85}_{-0.00}$ [0.00, 1.00])		$0.00^{+0.15}_{-0.00}$ [0.00, 0.54] ($0.00^{+0.42}_{-0.00}$ [0.00, 0.81])
any $\phi_{ai}, f_{a3}, \phi_{a3}$	$0.42^{+0.09}_{-0.33}$ [0.00, 0.57] ($0.00^{+0.86}_{-0.00}$ [0.00, 1.00])	$0.28^{+0.29}_{-0.28}$ [0.00, 0.97] ($0.00^{+0.59}_{-0.00}$ [0.00, 1.00])	

6.2 Validation of the HZZ measurements

It has been shown that the template method with a small set of optimal observables and multi-dimensional distribution method are expected to produce equivalent results [31]. Nonetheless, this is validated explicitly with a subset of the above HZZ measurements. The multidimensional distribution method has been applied to the study of the f_{a2} and f_{a3} parameters, as shown in Table 16. Figure 23 shows the expected and observed likelihood scans for the ef-

fective fractions f_{a2} and f_{a3} under the assumption of real couplings for both the template and multidimensional distribution methods. The two methods have a compatible expected performance and the differences are within the systematic uncertainties of the methods. The observed constraints are not expected to produce identical results because of the incomplete overlap of the data, which is due to the slightly different selection requirement on $m_{4\ell}$. Also, statistical variations occur because of the different parameterization of observables. The two methods provide consistent results.

Table 16: Summary of the allowed 95% CL intervals on the anomalous coupling parameters in HZZ interactions under the assumption that all the coupling ratios are real ($\phi_{ai} = 0$ or π) using the multidimensional distribution method. These results cross-check those presented in Table 13.

Parameter	Observed	Expected
$f_{a2} \cos(\phi_{a2})$	$[-0.14, 1.00]$	$[-0.18, 0.97]$
$f_{a3} \cos(\phi_{a3})$	$[-0.44, 0.40]$	$[-0.67, 0.67]$

6.3 Study of $\text{HZ}\gamma$ and $\text{H}\gamma\gamma$ couplings with the $\text{H} \rightarrow \text{VV} \rightarrow 4\ell$ channel

In the following, constraints on anomalous $\text{HZ}\gamma$ and $\text{H}\gamma\gamma$ interactions are obtained using the $\text{H} \rightarrow \text{VV} \rightarrow 4\ell$ data. Five anomalous couplings are considered, following Eq. (1) and Table 6, where the three observables for each measurement are listed. Only real couplings, $\phi_{ai} = 0$ or π , are considered in this test. The results of the likelihood function scan for the three parameters, $f_{ai} \cos \phi_{ai}$, are shown in Fig. 24, following the same formalism presented for the HZZ couplings in Section 6.1. The 68% and 95% CL intervals are shown in Table 13. In the case of the $f_{\Lambda 1}^{Z\gamma}$ measurement, there are two minima and only one central value with its 68% CL interval is shown in Table 13, while both 68% CL intervals are presented in Fig. 20.

Table 17: Summary of the allowed 95% CL intervals on the anomalous couplings in $\text{HZ}\gamma$ and $\text{H}\gamma\gamma$ interactions using results obtained with the template method in Table 13. The coupling ratios are assumed to be real ($\cos(\phi_{ai}^{\text{VV}}) = 0$ or π).

Parameter	Observed	Expected
$(\Lambda_1^{Z\gamma} \sqrt{ a_1 }) \cos(\phi_{\Lambda 1}^{Z\gamma})$	$[-\infty, +\infty]$	$[-\infty, +\infty]$
$a_2^{Z\gamma} / a_1$	$[-0.046, 0.044]$	$[-0.089, 0.092]$
$a_3^{Z\gamma} / a_1$	$[-0.042, 0.053]$	$[-0.090, 0.090]$
$a_2^{\gamma\gamma} / a_1$	$[-0.011, 0.054]$	$[-0.036, 0.038]$
$a_3^{\gamma\gamma} / a_1$	$[-0.039, 0.037]$	$[-0.041, 0.044]$
$(\sigma_2^{Z\gamma} / \sigma_{\text{SM}}^{Z\gamma}) (2a_2^{Z\gamma} / a_1)^2 \cos(\phi_{a2}^{Z\gamma})$	$[-1.7, 1.6] \times 10^2$	$[-6.5, 6.9] \times 10^2$
$(\sigma_3^{Z\gamma} / \sigma_{\text{SM}}^{Z\gamma}) (2a_3^{Z\gamma} / a_1)^2 \cos(\phi_{a2}^{Z\gamma})$	$[-1.2, 1.9] \times 10^2$	$[-5.5, 5.5] \times 10^2$
$(\sigma_2^{\gamma\gamma} / \sigma_{\text{SM}}^{\gamma\gamma}) (2a_2^{\gamma\gamma} / a_1)^2 \cos(\phi_{a2}^{\gamma\gamma})$	$[-0.3, 7.3] \times 10^2$	$[-3.3, 3.6] \times 10^2$
$(\sigma_3^{\gamma\gamma} / \sigma_{\text{SM}}^{\gamma\gamma}) (2a_3^{\gamma\gamma} / a_1)^2 \cos(\phi_{a3}^{\gamma\gamma})$	$[-3.8, 3.3] \times 10^2$	$[-4.1, 4.7] \times 10^2$

Using the transformation in Eq. (5), these results can be interpreted in terms of the coupling parameters used in Eq. (1) as shown in Table 17. The ratio $(\sigma_i^{\text{V}\gamma} / \sigma_{\text{SM}}^{\text{V}\gamma}) (2a_i^{\text{V}\gamma} / a_1)^2$ approximates the ratio $\mu = \sigma / \sigma_{\text{SM}}$ of the measured and expected SM cross sections for a Higgs boson decay $\text{H} \rightarrow \text{V}\gamma$. The ratio $(2/a_1)^2$ scales this measurement with respect to the $\text{H} \rightarrow \text{ZZ}$ coupling and is expected to be 1.0 in the SM. As can be seen in Table 17, the constraints presented on these

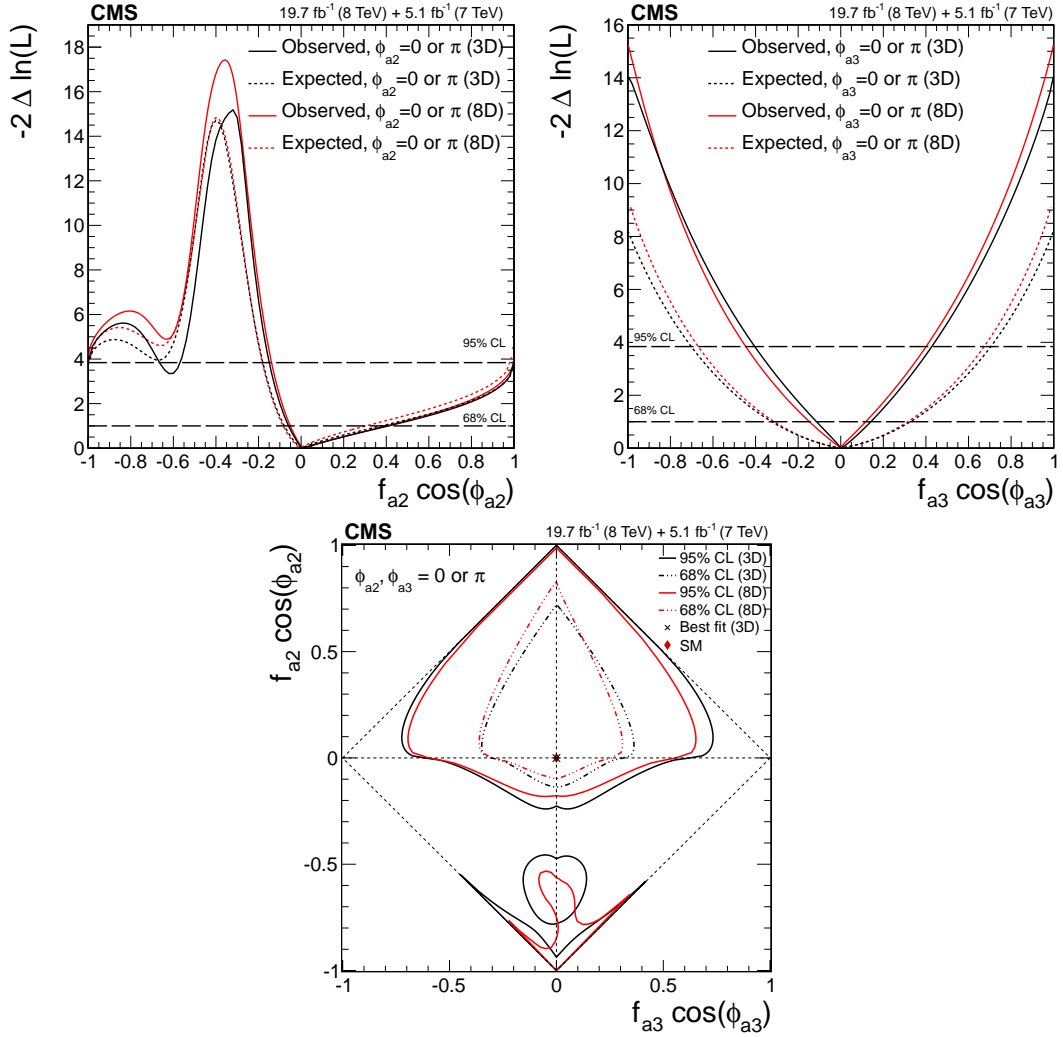


Figure 23: Expected (dashed) and observed (solid) likelihood scans for f_{a2} (top left) and f_{a3} (top right), and observed likelihood scan for the f_{a2} vs. f_{a3} fractions (bottom), obtained using the template method (3D, black) and the multidimensional distribution method (8D, red) in the study of anomalous HZZ interactions. The couplings are constrained to be real.

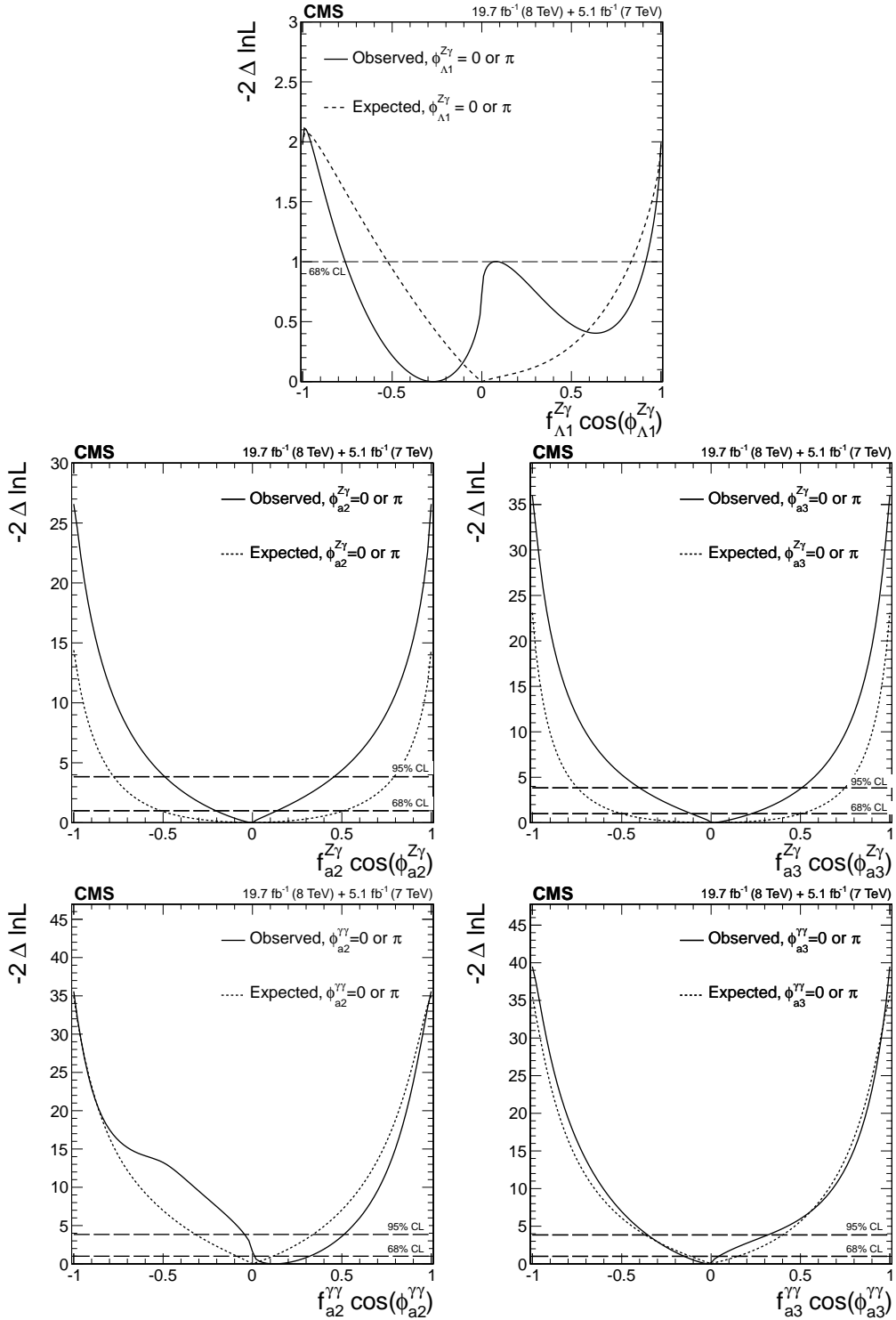


Figure 24: Expected (dashed) and observed (solid) likelihood scans using the template method for the effective fractions $f_{\Lambda 1}^{Z\gamma}$ (top), $f_{a2}^{Z\gamma}$ (middle left), $f_{a3}^{Z\gamma}$ (middle right), $f_{a2}^{\gamma\gamma}$ (bottom left), and $f_{a3}^{\gamma\gamma}$ (bottom right). The couplings studied are constrained to be real and all other couplings are fixed to the SM predictions. The $\cos \phi_{ai}^{VV}$ term allows a signed quantity where $\cos \phi_{ai}^{VV} = -1$ or $+1$.

ratios (<170 for $|a_2^{Z\gamma}|$ or <730 for $|a_2^{\gamma\gamma}|$ at 95% CL) are about one or three orders of magnitude higher than from the analyses of the direct $H \rightarrow Z\gamma$ ($\mu < 9.5$ at 95% CL [19]) or $H \rightarrow \gamma\gamma$ ($\mu = 1.14_{-0.23}^{+0.26}$ at 68% CL [15]) decays with on-shell photons, respectively. Therefore, the constraints presented on $f_{a_2}^{Z\gamma}$, $f_{a_3}^{Z\gamma}$, $f_{a_2}^{\gamma\gamma}$, $f_{a_3}^{\gamma\gamma}$ are not competitive compared with the direct cross-section measurements in $H \rightarrow Z\gamma$ or $\gamma\gamma$ decays. However, eventually with sufficiently large integrated luminosity it might be possible to measure $f_{a_2}^{V\gamma}$ and $f_{a_3}^{V\gamma}$ separately in the $H \rightarrow VV \rightarrow 4\ell$ decay, allowing for measurements of the CP properties in these couplings [56, 64]. The $H \rightarrow Z\gamma$ or $\gamma\gamma$ measurements with on-shell photons are sensitive only to the sum of the two cross-section fractions $f_{a_2}^{V\gamma}$ and $f_{a_3}^{V\gamma}$ and therefore cannot distinguish the two. Moreover, the $f_{\Lambda_1}^{Z\gamma}$ measurement is not possible with on-shell photons.

As in the case of the HZZ couplings, anomalous $HZ\gamma$ and $H\gamma\gamma$ couplings are found to be consistent with zero, as expected in the SM with the current precision. Since the measurement of the $HZ\gamma$ and $H\gamma\gamma$ couplings in the $H \rightarrow VV \rightarrow 4\ell$ decay is not yet competitive with the on-shell measurements, further investigation of several parameters simultaneously is not considered with the current data.

6.4 Study of HWW couplings with the $H \rightarrow WW \rightarrow \ell\nu\ell\nu$ channel

Constraints on anomalous HWW interactions are obtained using the $H \rightarrow WW \rightarrow \ell\nu\ell\nu$ final state. Three measurements are performed using the template method with the two observables, m_T and $m_{\ell\ell}$, as summarized in Table 6. Only real couplings, $\phi_{ai}^{WW} = 0$ or π , are considered. The results of the likelihood function scan for the three parameters, $f_{ai}^{WW} \cos\phi_{ai}^{WW}$, are shown in Fig. 25, following the HZZ approach presented in Section 6.1. The 68% and 95% CL intervals are shown in Table 13. Using the transformation in Eq. (5), these results could be interpreted for the coupling parameters used in Eq. (1) as shown in Table 18.

Similarly to the HZZ case, strong destructive interference of the SM and anomalous contributions at $f_{\Lambda_1}^{WW} \cos(\phi_{\Lambda_1}^{WW}) \sim +0.5$ or $f_{a_2}^{WW} \cos(\phi_{a_2}^{WW}) \sim -0.5$ leads to very different kinematic distributions and exclusions with high confidence levels. Since the measurement of the HWW anomalous couplings with the $H \rightarrow WW \rightarrow \ell\nu\ell\nu$ decay is not expected to provide strong constraints with the current data, a deeper investigation of several parameters simultaneously is not considered here. On the other hand, the combination of the HZZ and HWW measurements is expected to provide an improvement in the precision of the HVV couplings with certain symmetry considerations.

Table 18: Summary of the allowed 95% CL intervals on the anomalous couplings in HWW interactions using results obtained with the template method in Table 13. The coupling ratios are assumed to be real (including $\cos(\phi_{\Lambda_1}^{WW}) = 0$ or π).

Parameter	Observed	Expected
$(\Lambda_1^{WW} \sqrt{ a_1^{WW} }) \cos(\phi_{\Lambda_1}^{WW})$	$[-\infty, +\infty]$	$[-\infty, 87 \text{ GeV}] \cup [93 \text{ GeV}, +\infty]$
a_2^{WW}/a_1^{WW}	$[-\infty, -1.22] \cup [-0.71, +\infty]$	$[-\infty, -1.30] \cup [-0.59, +\infty]$
a_3^{WW}/a_1^{WW}	$[-\infty, +\infty]$	$[-\infty, +\infty]$

6.5 Combination of HZZ and HWW results

Further improvement on the HVV anomalous coupling constraints can be obtained from the combination of the $H \rightarrow ZZ \rightarrow 4\ell$ and $H \rightarrow WW \rightarrow \ell\nu\ell\nu$ analyses by employing symmetry considerations between the HZZ and HWW interactions. Two scenarios are considered. In

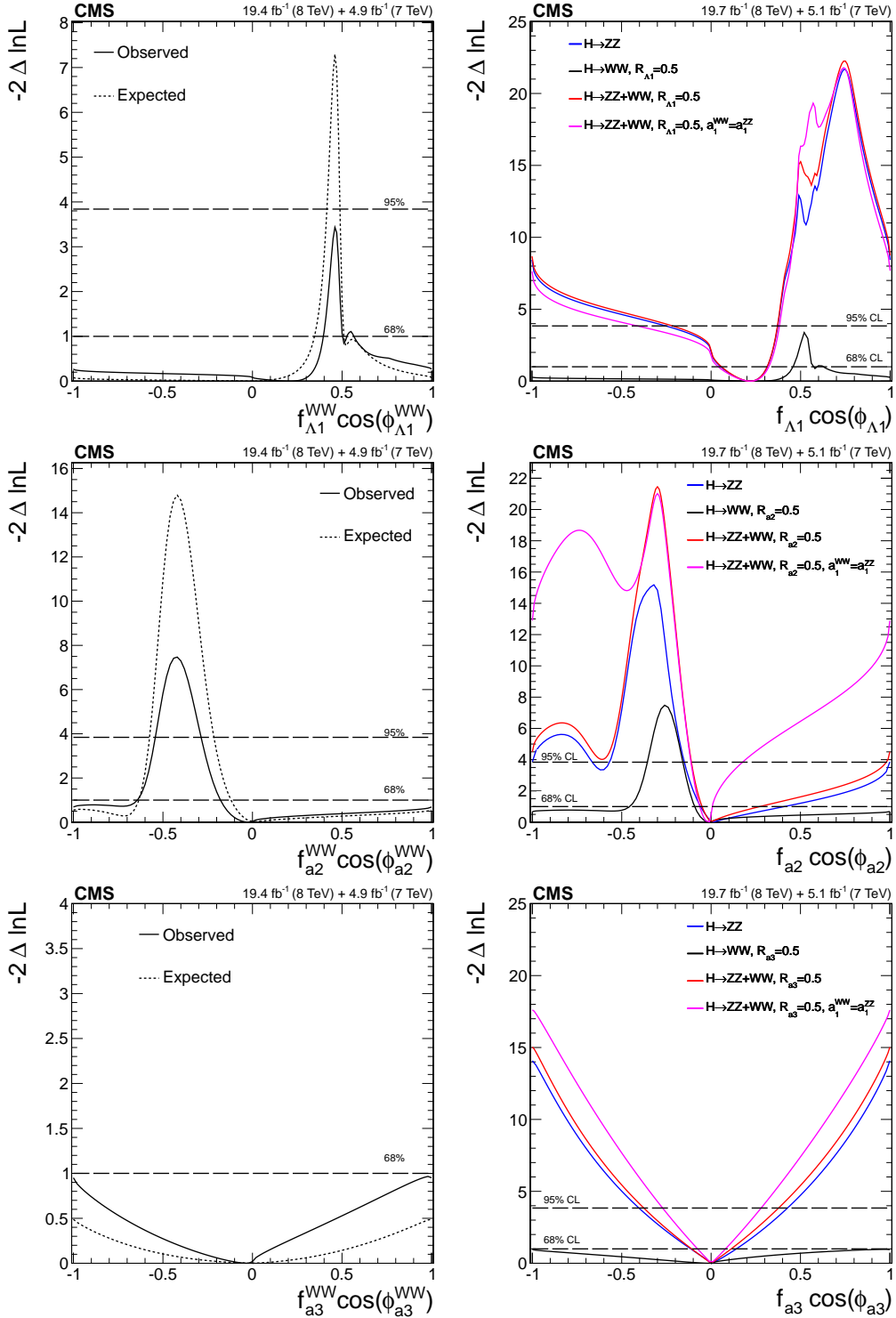


Figure 25: Expected (dashed) and observed (solid) likelihood scans for effective fractions $f_{\Lambda 1}$ (top), f_{a2} (middle), f_{a3} (bottom). The couplings studied are constrained to be real and all other anomalous couplings are fixed to the SM predictions. The $\cos \phi_{ai}$ term allows a signed quantity where $\cos \phi_{ai} = -1$ or $+1$. Plots on the left show the results of the $H \rightarrow WW \rightarrow \ell\nu\ell\nu$ analysis expressed in terms of the HWW couplings. Plots on the right show the combined $H \rightarrow WW$ and $H \rightarrow ZZ$ result in terms of the HZZ couplings for $R_{ai} = 0.5$. Measurements are shown for each channel separately and two types of combination are present: using $a_1^{WW} = a_1$ (red) and without such a constraint (magenta).

the first, custodial symmetry is assumed, leading to $a_1^{WW} = a_1$. The second scenario assumes no relationship between the two couplings. In both cases, a combined likelihood scan of f_{ai} is performed for the full range of $-1 \leq R_{ai} \leq +1$. For a given value of R_{ai} in Eq. (6), the f_{ai} and f_{ai}^{WW} values are related by Eq. (7) and constraints on a single parameter can be obtained.

For the combination where custodial symmetry is assumed, the yield in the $H \rightarrow WW \rightarrow \ell\nu\ell\nu$ channel is related to the yield in the $H \rightarrow ZZ \rightarrow 4\ell$ channel, which leads to stronger constraints. This yield relationship is possible if either the fraction of VBF and VH production is known or the reconstruction efficiency for these and gluon fusion production mechanisms is the same. The latter is known to be somewhat different in the $H \rightarrow WW \rightarrow \ell\nu\ell\nu$ channel due to the selection being sensitive to the associated jets, see Table 4. The fraction of VBF and VH production has been found to be small and consistent with the SM expectation of 12% [21]. However, this constraint is performed under the assumption of the SM kinematics of associated particles. While it is possible to obtain similar constraints on associated Higgs boson production with anomalous couplings, that analysis is beyond the scope of this paper. Therefore, we assume that the gluon fusion production dominates and the fraction of VBF and VH production is not larger than expected in the SM. This leads to potential uncertainty on the yield relationship of about 3%, which we neglect. Should the fraction of VBF and VH production be different, the corresponding limits could be recalculated.

Table 19: Summary of allowed 68% CL (central values with uncertainties) and 95% CL (ranges in square brackets) intervals on anomalous coupling parameters in HVV interactions in combination of HZZ and HWW measurements assuming the symmetry $a_i = a_i^{WW}$, including $R_{ai} = 0.5$, and real coupling ratios ($\phi_{ai}^{VV} = 0$ or π). The last column indicates the observed (expected) confidence level of a pure anomalous coupling corresponding to $f_{ai}^{VV} = 1$ when compared to the SM expectation $f_{ai}^{VV} = 0$. The results are obtained with the template method.

Parameter	Observed	Expected	$f_{ai}^{VV} = 1$
$f_{\Lambda 1} \cos(\phi_{\Lambda 1})$	$0.21_{-0.17}^{+0.11} [-0.42, 0.38]$	$0.00_{-0.80}^{+0.15} [-1, 0.27] \cup [0.95, 1]$	0.56% (13%)
$f_{a2} \cos(\phi_{a2})$	$-0.01_{-0.05}^{+0.02} [-0.11, 0.17]$	$0.00_{-0.03}^{+0.08} [-0.07, 0.51]$	0.03% (0.25%)
$f_{a3} \cos(\phi_{a3})$	$0.00_{-0.08}^{+0.08} [-0.27, 0.28]$	$0.00_{-0.23}^{+0.23} [-0.53, 0.53]$	<0.01% (0.08%)

Table 20: Summary of the allowed 95% CL intervals on the anomalous couplings in HVV interactions in combination of HZZ and HWW measurements in Table 19 assuming the symmetry $a_i = a_i^{WW}$, including $R_{ai} = 0.5$, and real coupling ratios ($\phi_{ai}^{VV} = 0$ or π).

Parameter	Observed	Expected
$(\Lambda_1 \sqrt{ a_1 }) \cos(\phi_{\Lambda 1})$	$[-\infty, -100 \text{ GeV}] \cup [103 \text{ GeV}, \infty]$	$[-\infty, 43 \text{ GeV}] \cup [116 \text{ GeV}, \infty]$
a_2/a_1	$[-0.58, 0.76]$	$[-0.45, 1.67]$
a_3/a_1	$[-1.54, 1.57]$	$[-2.65, 2.65]$

An example of the combination under the assumption $R_{ai} = 0.5$ ($r_{ai} = 1$) is shown in Fig. 25 and Table 19, where the effect of using the information on the relative yield can be seen. Both combination scenarios are shown. When the $H \rightarrow ZZ \rightarrow 4\ell$ and $H \rightarrow WW \rightarrow \ell\nu\ell\nu$ signal yields are left independent, custodial symmetry is not assumed. The increase in expected signal yield towards $f_{ai} = \pm 1$ is greater in the $H \rightarrow WW$ channel compared to the $H \rightarrow ZZ$ channel, leading to additional discriminating power when the yields are related. For example, the enhancement relative to the SM is a factor of 2.4 for $f_{a2} = \pm 1$. Since the number of events observed in the $H \rightarrow ZZ \rightarrow 4\ell$ and $H \rightarrow WW \rightarrow \ell\nu\ell\nu$ channels is compatible with the SM, this enhancement of 2.4 is not compatible with the SM and the $f_{a2} = \pm 1$ scenario is strongly

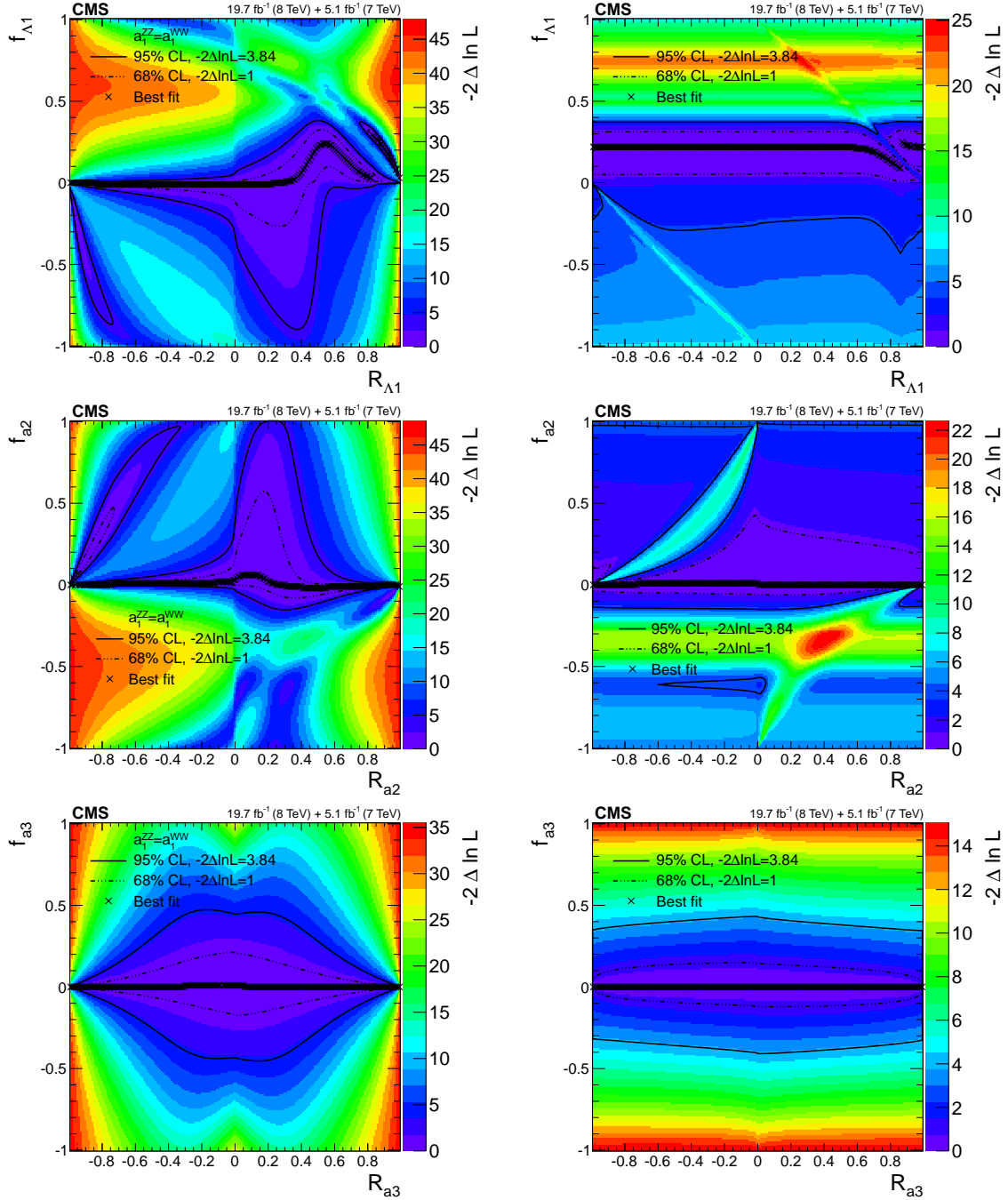


Figure 26: Observed conditional likelihood scans of $f_{\Lambda 1}$ (top), f_{a2} (middle), f_{a3} (bottom) for a given R_{ai} value from the combined analysis of the $H \rightarrow WW$ and $H \rightarrow ZZ$ channels using the template method. The results are shown with custodial symmetry $a_1 = a_1^{WW}$ (left) and without such an assumption (right). Each cross indicates the minimum value of $-2 \Delta \ln \mathcal{L}$ and the contours indicate the one-parameter confidence intervals of f_{ai} for a given value of R_{ai} .

excluded from the consideration of the yields alone. The combined analysis uses both yield and kinematic information in an optimal way. Using the transformation in Eq. (5), these results could be interpreted for the coupling parameters used in Eq. (1) as shown in Table 20.

To present the results in a model-independent way, conditional likelihood scans of f_{ai} , for a particular R_{ai} value, are performed. In this way, the confidence intervals of f_{ai} are obtained for a given value of R_{ai} . These results are presented in Fig. 26, and show features that arise from the combination of the $H \rightarrow ZZ$ and WW channels, but with larger exclusion power in some areas of the parameter space.

7 Summary

In this paper, a comprehensive study of the spin-parity properties of the recently discovered H boson and of the tensor structure of its interactions with electroweak gauge bosons is presented using the $H \rightarrow ZZ$, $Z\gamma^*$, $\gamma^*\gamma^* \rightarrow 4\ell$, $H \rightarrow WW \rightarrow \ell\nu\ell\nu$, and $H \rightarrow \gamma\gamma$ decay modes. The results are based on the 2011 and 2012 data from pp collisions recorded with the CMS detector at the LHC, and correspond to an integrated luminosity of up to 5.1 fb^{-1} at a center-of-mass energy of 7 TeV and up to 19.7 fb^{-1} at 8 TeV.

The phenomenological formulation for the interactions of a spin-zero, -one, or -two boson with the SM particles is based on a scattering amplitude or, equivalently, an effective field theory Lagrangian, with operators up to dimension five. The dedicated simulation and matrix element likelihood approach for the analysis of the kinematics of H boson production and decay in different topologies are based on this formulation. A maximum likelihood fit of the signal and background distributions provides constraints on the anomalous couplings of the H boson.

The study focuses on testing for the presence of anomalous effects in HZZ and HWW interactions under spin-zero, -one, and -two hypotheses. The combination of the $H \rightarrow ZZ$ and $H \rightarrow WW$ measurements leads to tighter constraints on the H boson spin-parity and anomalous HVV interactions. The combination with the $H \rightarrow \gamma\gamma$ measurements also allows tighter constraints in the spin-two case. The $HZ\gamma$ and $H\gamma\gamma$ interactions are probed for the first time using the 4ℓ final state.

The exotic-spin study covers the analysis of mixed-parity spin-one states and ten spin-two hypotheses under the assumption of production either via gluon fusion or quark-antiquark annihilation, or without such an assumption. The spin-one hypotheses are excluded at a greater than 99.999% CL in the ZZ and WW modes, while in the $\gamma\gamma$ mode they are excluded by the Landau-Yang theorem. The spin-two boson with gravity-like minimal couplings is excluded at a 99.87% CL, and the other spin-two hypotheses tested are excluded at a 99% CL or higher.

Given the exclusion of the spin-one and spin-two scenarios, constraints are set on the contribution of eleven anomalous couplings to the HZZ , $HZ\gamma$, $H\gamma\gamma$, and HWW interactions of a spin-zero H boson, as summarized in Table 13. Among these is the measurement of the f_{a3} parameter, which is defined as the fractional pseudoscalar cross section in the $H \rightarrow ZZ$ channel. The constraint is $f_{a3} < 0.43$ (0.40) at a 95% CL for the positive (negative) phase of the pseudoscalar coupling with respect to the dominant SM-like coupling and $f_{a3} = 1$ exclusion of a pure pseudoscalar hypothesis at a 99.98% CL.

All observations are consistent with the expectations for a scalar SM-like Higgs boson. It is not presently established that the interactions of the observed state conserve C -parity or CP -parity. However, under the assumption that both quantities are conserved, our measurements require the quantum numbers of the new state to be $J^{PC} = 0^{++}$. The positive P -parity follows from

the f_{a3}^{VV} measurements in the $H \rightarrow ZZ, Z\gamma^*, \gamma^*\gamma^* \rightarrow 4\ell$, and $H \rightarrow WW \rightarrow \ell\nu\ell\nu$ decays and the positive C -parity follows from observation of the $H \rightarrow \gamma\gamma$ decay. Further measurements probing the tensor structure of the HVV and $Hf\bar{f}$ interactions can test the assumption of CP -invariance.

Acknowledgments

We thank Markus Schulze for optimizing the JHUGEN Monte Carlo simulation program for this analysis. We congratulate our colleagues in the CERN accelerator departments for the excellent performance of the LHC and thank the technical and administrative staffs at CERN and at other CMS institutes for their contributions to the success of the CMS effort. In addition, we gratefully acknowledge the computing centres and personnel of the Worldwide LHC Computing Grid for delivering so effectively the computing infrastructure essential to our analyses. Finally, we acknowledge the enduring support for the construction and operation of the LHC and the CMS detector provided by the following funding agencies: the Austrian Federal Ministry of Science, Research and Economy and the Austrian Science Fund; the Belgian Fonds de la Recherche Scientifique, and Fonds voor Wetenschappelijk Onderzoek; the Brazilian Funding Agencies (CNPq, CAPES, FAPERJ, and FAPESP); the Bulgarian Ministry of Education and Science; CERN; the Chinese Academy of Sciences, Ministry of Science and Technology, and National Natural Science Foundation of China; the Colombian Funding Agency (COLCIENCIAS); the Croatian Ministry of Science, Education and Sport, and the Croatian Science Foundation; the Research Promotion Foundation, Cyprus; the Ministry of Education and Research, Estonian Research Council via IUT23-4 and IUT23-6 and European Regional Development Fund, Estonia; the Academy of Finland, Finnish Ministry of Education and Culture, and Helsinki Institute of Physics; the Institut National de Physique Nucléaire et de Physique des Particules / CNRS, and Commissariat à l'Énergie Atomique et aux Énergies Alternatives / CEA, France; the Bundesministerium für Bildung und Forschung, Deutsche Forschungsgemeinschaft, and Helmholtz-Gemeinschaft Deutscher Forschungszentren, Germany; the General Secretariat for Research and Technology, Greece; the National Scientific Research Foundation, and National Innovation Office, Hungary; the Department of Atomic Energy and the Department of Science and Technology, India; the Institute for Studies in Theoretical Physics and Mathematics, Iran; the Science Foundation, Ireland; the Istituto Nazionale di Fisica Nucleare, Italy; the Ministry of Science, ICT and Future Planning, and National Research Foundation (NRF), Republic of Korea; the Lithuanian Academy of Sciences; the Ministry of Education, and University of Malaya (Malaysia); the Mexican Funding Agencies (CINVESTAV, CONACYT, SEP, and UASLP-FAI); the Ministry of Business, Innovation and Employment, New Zealand; the Pakistan Atomic Energy Commission; the Ministry of Science and Higher Education and the National Science Centre, Poland; the Fundação para a Ciência e a Tecnologia, Portugal; JINR, Dubna; the Ministry of Education and Science of the Russian Federation, the Federal Agency of Atomic Energy of the Russian Federation, Russian Academy of Sciences, and the Russian Foundation for Basic Research; the Ministry of Education, Science and Technological Development of Serbia; the Secretaría de Estado de Investigación, Desarrollo e Innovación and Programa Consolider-Ingenio 2010, Spain; the Swiss Funding Agencies (ETH Board, ETH Zurich, PSI, SNF, UniZH, Canton Zurich, and SER); the Ministry of Science and Technology, Taipei; the Thailand Center of Excellence in Physics, the Institute for the Promotion of Teaching Science and Technology of Thailand, Special Task Force for Activating Research and the National Science and Technology Development Agency of Thailand; the Scientific and Technical Research Council of Turkey, and Turkish Atomic Energy Authority; the National Academy of Sciences of Ukraine, and State Fund for Fundamental Researches, Ukraine; the Science and

Technology Facilities Council, UK; the US Department of Energy, and the US National Science Foundation.

Individuals have received support from the Marie-Curie programme and the European Research Council and EPLANET (European Union); the Leventis Foundation; the A. P. Sloan Foundation; the Alexander von Humboldt Foundation; the Belgian Federal Science Policy Office; the Fonds pour la Formation à la Recherche dans l'Industrie et dans l'Agriculture (FRIA-Belgium); the Agentschap voor Innovatie door Wetenschap en Technologie (IWT-Belgium); the Ministry of Education, Youth and Sports (MEYS) of the Czech Republic; the Council of Science and Industrial Research, India; the HOMING PLUS programme of Foundation for Polish Science, cofinanced from European Union, Regional Development Fund; the Compagnia di San Paolo (Torino); the Consorzio per la Fisica (Trieste); MIUR project 20108T4XTM (Italy); the Thalys and Aristeia programmes cofinanced by EU-ESF and the Greek NSRF; and the National Priorities Research Program by Qatar National Research Fund.

References

- [1] ATLAS Collaboration, "Observation of a new particle in the search for the Standard Model Higgs boson with the ATLAS detector at the LHC", *Phys. Lett. B* **716** (2012) 1, doi:10.1016/j.physletb.2012.08.020, arXiv:1207.7214.
- [2] CMS Collaboration, "Observation of a new boson at a mass of 125 GeV with the CMS experiment at the LHC", *Phys. Lett. B* **716** (2012) 30, doi:10.1016/j.physletb.2012.08.021, arXiv:1207.7235.
- [3] CMS Collaboration, "Observation of a new boson with mass near 125 GeV in pp collisions at $\sqrt{s} = 7$ and 8 TeV", *JHEP* **06** (2013) 081, doi:10.1007/JHEP06(2013)081, arXiv:1303.4571.
- [4] S. L. Glashow, "Partial-symmetries of Weak Interactions", *Nucl. Phys.* **22** (1961) 579, doi:10.1016/0029-5582(61)90469-2.
- [5] F. Englert and R. Brout, "Broken Symmetry and the Mass of Gauge Vector Mesons", *Phys. Rev. Lett.* **13** (1964) 321, doi:10.1103/PhysRevLett.13.321.
- [6] P. W. Higgs, "Broken symmetries, massless particles and gauge fields", *Phys. Lett.* **12** (1964) 132, doi:10.1016/0031-9163(64)91136-9.
- [7] P. W. Higgs, "Broken Symmetries and the Masses of Gauge Bosons", *Phys. Rev. Lett.* **13** (1964) 508, doi:10.1103/PhysRevLett.13.508.
- [8] G. S. Guralnik, C. R. Hagen, and T. W. B. Kibble, "Global Conservation Laws and Massless Particles", *Phys. Rev. Lett.* **13** (1964) 585, doi:10.1103/PhysRevLett.13.585.
- [9] S. Weinberg, "A Model of Leptons", *Phys. Rev. Lett.* **19** (1967) 1264, doi:10.1103/PhysRevLett.19.1264.
- [10] A. Salam, "Weak and electromagnetic interactions", in *Elementary particle physics: relativistic groups and analyticity*, N. Svartholm, ed., p. 367. Almqvist & Wiksell, Stockholm, 1968. Proceedings of the eighth Nobel symposium.

- [11] CMS Collaboration, "On the mass and spin-parity of the Higgs boson candidate via its decays to Z boson pairs", *Phys. Rev. Lett.* **110** (2013) 081803, doi:10.1103/PhysRevLett.110.081803, arXiv:1212.6639.
- [12] CMS Collaboration, "Measurement of the properties of a Higgs boson in the four-lepton final state", *Phys. Rev. D* **89** (2014) 092007, doi:10.1103/PhysRevD.89.092007, arXiv:1312.5353.
- [13] CMS Collaboration, "Constraints on the Higgs boson width from off-shell production and decay to Z-boson pairs", *Phys. Lett. B* **736** (2014) 64, doi:10.1016/j.physletb.2014.06.077, arXiv:1405.3455.
- [14] CMS Collaboration, "Measurement of Higgs boson production and properties in the WW decay channel with leptonic final states", *JHEP* **01** (2014) 096, doi:10.1007/JHEP01(2014)096, arXiv:1312.1129.
- [15] CMS Collaboration, "Observation of the diphoton decay of the Higgs boson and measurement of its properties", *Eur. Phys. J. C* **74** (2014) 3076, doi:10.1140/epjc/s10052-014-3076-z, arXiv:1407.0558.
- [16] CMS Collaboration, "Search for the standard model Higgs boson produced in association with a W or a Z boson and decaying to bottom quarks", *Phys. Rev. D* **89** (2014) 012003, doi:10.1103/PhysRevD.89.012003, arXiv:1310.3687.
- [17] CMS Collaboration, "Evidence for the 125 GeV Higgs boson decaying to a pair of τ leptons", *JHEP* **05** (2014) 104, doi:10.1007/JHEP05(2014)104, arXiv:1401.5041.
- [18] CMS Collaboration, "Search for the standard model Higgs boson produced in association with a top-quark pair in pp collisions at the LHC", *JHEP* **05** (2013) 145, doi:10.1007/JHEP05(2013)145, arXiv:1303.0763.
- [19] CMS Collaboration, "Search for a Higgs boson decaying into a Z and a photon in pp collisions at $\sqrt{s} = 7$ and 8 TeV", *Phys. Lett. B* **726** (2013) 587, doi:10.1016/j.physletb.2013.09.057, arXiv:1307.5515.
- [20] CMS Collaboration, "Search for invisible decays of Higgs bosons in the vector boson fusion and associated ZH production modes", *Eur. Phys. J. C* **74** (2014) 2980, doi:10.1140/epjc/s10052-014-2980-6, arXiv:1404.1344.
- [21] CMS Collaboration, "Precise determination of the mass of the Higgs boson and tests of compatibility of its couplings with the standard model predictions using proton collisions at 7 and 8 TeV", (2014). arXiv:1412.8662. Submitted to EPJC.
- [22] ATLAS Collaboration, "Evidence for the spin-0 nature of the Higgs boson using ATLAS data", *Phys. Lett. B* **726** (2013) 120, doi:10.1016/j.physletb.2013.08.026, arXiv:1307.1432.
- [23] ATLAS Collaboration, "Measurements of Higgs boson production and couplings in diboson final states with the ATLAS detector at the LHC", *Phys. Lett. B* **726** (2013) 119, doi:10.1016/j.physletb.2013.08.010, arXiv:1307.1427.

- [24] ATLAS Collaboration, “Measurement of the Higgs boson mass from the $H \rightarrow \gamma\gamma$ and $H \rightarrow ZZ^* \rightarrow 4\ell$ channels with the ATLAS detector using 25 fb^{-1} of pp collision data”, *Phys. Rev. D* **90** (2014) 052004, doi:10.1103/PhysRevD.90.052004, arXiv:1406.3827.
- [25] ATLAS Collaboration, “Search for Higgs boson decays to a photon and a Z boson in pp collisions at $\sqrt{s} = 7$ and 8 TeV with the ATLAS detector”, *Phys. Lett. B* **732** (2014) 8, doi:10.1016/j.physletb.2014.03.015, arXiv:1402.3051.
- [26] ATLAS Collaboration, “Search for Invisible Decays of a Higgs Boson Produced in Association with a Z Boson in ATLAS”, *Phys. Rev. Lett.* **112** (2014) 201802, doi:10.1103/PhysRevLett.112.201802, arXiv:1402.3244.
- [27] ATLAS Collaboration, “Measurement of Higgs boson production in the diphoton decay channel in pp collisions at center-of-mass energies of 7 and 8 TeV with the ATLAS detector”, (2014). arXiv:1408.7084.
- [28] Y. Gao et al., “Spin determination of single-produced resonances at hadron colliders”, *Phys. Rev. D* **81** (2010) 075022, doi:10.1103/PhysRevD.81.075022, arXiv:1001.3396.
- [29] S. Bolognesi et al., “Spin and parity of a single-produced resonance at the LHC”, *Phys. Rev. D* **86** (2012) 095031, doi:10.1103/PhysRevD.86.095031, arXiv:1208.4018.
- [30] Y. Chen, N. Tran, and R. Vega-Morales, “Scrutinizing the Higgs Signal and Background in the $2e2\mu$ Golden Channel”, *JHEP* **01** (2013) 182, doi:10.1007/JHEP01(2013)182, arXiv:1211.1959.
- [31] I. Anderson et al., “Constraining anomalous HVV interactions at proton and lepton colliders”, *Phys. Rev. D* **89** (2014) 035007, doi:10.1103/PhysRevD.89.035007, arXiv:1309.4819.
- [32] M. Chen et al., “Role of interference in unraveling the ZZ couplings of the newly discovered boson at the LHC”, *Phys. Rev. D* **89** (2014) 034002, doi:10.1103/PhysRevD.89.034002, arXiv:1310.1397.
- [33] Y. Chen et al., “8D Likelihood Effective Higgs Couplings Extraction Framework in the Golden Channel”, (2014). arXiv:1401.2077.
- [34] J. R. Dell’Aquila and C. A. Nelson, “Simple tests for CP or P violation by sequential decays: $V_1 V_2$ modes with decays into $\bar{\ell}_A \ell_B$ and/or $\bar{q}_A q_B$ ”, *Phys. Rev. D* **33** (1986) 101, doi:10.1103/PhysRevD.33.101.
- [35] C. A. Nelson, “Correlation between Decay Planes in Higgs Boson Decays into W Pair (into Z Pair)”, *Phys. Rev. D* **37** (1988) 1220, doi:10.1103/PhysRevD.37.1220.
- [36] A. Soni and R. M. Xu, “Probing CP violation via Higgs decays to four leptons”, *Phys. Rev. D* **48** (1993) 5259, doi:10.1103/PhysRevD.48.5259, arXiv:hep-ph/9301225.
- [37] D. Chang, W.-Y. Keung, and I. Phillips, “ CP odd correlation in the decay of neutral Higgs boson into ZZ , W^+W^- , or $t\bar{t}$ ”, *Phys. Rev. D* **48** (1993) 3225, doi:10.1103/PhysRevD.48.3225, arXiv:hep-ph/9303226.

- [38] V. D. Barger et al., “Higgs bosons: Intermediate mass range at e^+e^- colliders”, *Phys. Rev. D* **49** (1994) 79, doi:10.1103/PhysRevD.49.79, arXiv:hep-ph/9306270.
- [39] T. Arens and L. M. Sehgal, “Energy spectra and energy correlations in the decay $H \rightarrow Z Z \rightarrow \mu^+\mu^-\mu^+\mu^-$ ”, *Z. Phys. C* **66** (1995) 89, doi:10.1007/BF01496583, arXiv:hep-ph/9409396.
- [40] T. Han and J. Jiang, “CP violating ZZH coupling at e^+e^- linear colliders”, *Phys. Rev. D* **63** (2001) 096007, doi:10.1103/PhysRevD.63.096007, arXiv:hep-ph/0011271.
- [41] T. Plehn, D. L. Rainwater, and D. Zeppenfeld, “Determining the structure of Higgs couplings at the LHC”, *Phys. Rev. Lett.* **88** (2002) 051801, doi:10.1103/PhysRevLett.88.051801, arXiv:hep-ph/0105325.
- [42] S. Y. Choi, D. J. Miller, M. M. Mühlleitner, and P. M. Zerwas, “Identifying the Higgs spin and parity in decays to Z pairs”, *Phys. Lett. B* **553** (2003) 61, doi:10.1016/S0370-2693(02)03191-X, arXiv:hep-ph/0210077.
- [43] C. P. Buszello, I. Fleck, P. Marquard, and J. J. van der Bij, “Prospective analysis of spin- and CP-sensitive variables in $H \rightarrow ZZ \rightarrow l_1^+l_1^-l_2^+l_2^-$ at the LHC”, *Eur. Phys. J. C* **32** (2004) 209, doi:10.1140/epjc/s2003-01392-0, arXiv:hep-ph/0212396.
- [44] E. Accomando et al., “Workshop on CP Studies and Non-Standard Higgs Physics”, (2006). arXiv:hep-ph/0608079.
- [45] R. M. Godbole, D. J. Miller, and M. M. Mühlleitner, “Aspects of CP violation in the H ZZ coupling at the LHC”, *JHEP* **12** (2007) 031, doi:10.1088/1126-6708/2007/12/031, arXiv:0708.0458.
- [46] O. Antipin and A. Soni, “Towards establishing the spin of warped gravitons”, *JHEP* **10** (2008) 018, doi:10.1088/1126-6708/2008/10/018, arXiv:0806.3427.
- [47] W.-Y. Keung, I. Low, and J. Shu, “Landau-Yang Theorem and Decays of a Z' Boson into Two Z Bosons”, *Phys. Rev. Lett.* **101** (2008) 091802, doi:10.1103/PhysRevLett.101.091802, arXiv:0806.2864.
- [48] K. Hagiwara, Q. Li, and K. Mawatari, “Jet angular correlation in vector-boson fusion processes at hadron colliders”, *JHEP* **07** (2009) 101, doi:10.1088/1126-6708/2009/07/101, arXiv:0905.4314.
- [49] A. De Rújula et al., “Higgs look-alikes at the LHC”, *Phys. Rev. D* **82** (2010) 013003, doi:10.1103/PhysRevD.82.013003, arXiv:1001.5300.
- [50] N. D. Christensen, T. Han, and Y. Li, “Testing CP Violation in ZZH Interactions at the LHC”, *Phys. Lett. B* **693** (2010) 28, doi:10.1016/j.physletb.2010.08.008, arXiv:1005.5393.
- [51] J. S. Gainer, K. Kumar, I. Low, and R. Vega-Morales, “Improving the sensitivity of Higgs boson searches in the golden channel”, *JHEP* **11** (2011) 027, doi:10.1007/JHEP11(2011)027, arXiv:1108.2274.
- [52] J. Ellis, D. S. Hwang, V. Sanz, and T. You, “A Fast Track towards the ‘Higgs’ Spin and Parity”, *JHEP* **11** (2012) 134, doi:10.1007/JHEP11(2012)134, arXiv:1208.6002.

- [53] J. S. Gainer et al., “Geolocating the Higgs Boson Candidate at the LHC”, *Phys. Rev. Lett.* **111** (2013) 041801, doi:10.1103/PhysRevLett.111.041801, arXiv:1304.4936.
- [54] P. Artoisenet et al., “A framework for Higgs characterisation”, *JHEP* **11** (2013) 043, doi:10.1007/JHEP11(2013)043, arXiv:1306.6464.
- [55] Y. Chen and R. Vega-Morales, “Extracting Effective Higgs Couplings in the Golden Channel”, *JHEP* **04** (2014) 057, doi:10.1007/JHEP04(2014)057, arXiv:1310.2893.
- [56] Y. Chen, R. Harnik, and R. Vega-Morales, “Probing the Higgs Couplings to Photons in $h \rightarrow 4\ell$ at the LHC”, (2014). arXiv:1404.1336.
- [57] J. S. Gainer et al., “Beyond Geolocating: Constraining Higher Dimensional Operators in $H \rightarrow 4\ell$ with Off-Shell Production and More”, (2014). arXiv:1403.4951.
- [58] N. P. Samios et al., “Parity of the Neutral Pion and the Decay $\pi^0 \rightarrow 2e^+ + 2e^-$ ”, *Phys. Rev.* **126** (1962) 1844, doi:10.1103/PhysRev.126.1844.
- [59] N. Cabibbo and A. Maksymowicz, “Angular Correlations in K_{e4} Decays and Determination of Low-Energy π - π Phase Shifts”, *Phys. Rev. B* **137** (1965) 438, doi:10.1103/PhysRev.137.B438. [Erratum doi:10.1103/PhysRev.168.1926].
- [60] G. Kramer and W. F. Palmer, “Branching ratios and CP asymmetries in the decay $B \rightarrow VV$ ”, *Phys. Rev. D* **45** (1992) 193, doi:10.1103/PhysRevD.45.193.
- [61] KTeV Collaboration, “Determination of the Parity of the Neutral Pion via the Four-Electron Decay”, *Phys. Rev. Lett.* **100** (2008) 182001, doi:10.1103/PhysRevLett.100.182001, arXiv:0802.2064.
- [62] BABAR Collaboration, “Time-Dependent and Time-Integrated Angular Analysis of $B \rightarrow \phi K_s \pi^0$ and $B \rightarrow \phi K^+ \pi^-$ ”, *Phys. Rev. D* **78** (2008) 092008, doi:10.1103/PhysRevD.78.092008, arXiv:0808.3586.
- [63] I. Low, J. Lykken, and G. Shaughnessy, “Have We Observed the Higgs (Imposter)?”, *Phys. Rev. D* **86** (2012) 093012, doi:10.1103/PhysRevD.86.093012, arXiv:1207.1093.
- [64] S. Dawson et al., “Higgs Working Group Report of the Snowmass 2013 Community Planning Study”, (2013). arXiv:1310.8361.
- [65] I. Low and J. Lykken, “Revealing the electroweak properties of a new scalar resonance”, *JHEP* **10** (2010) 053, doi:10.1007/JHEP10(2010)053, arXiv:1005.0872.
- [66] P. Sikivie, L. Susskind, M. B. Voloshin, and V. I. Zakharov, “Isospin Breaking in Technicolor Models”, *Nucl. Phys. B* **173** (1980) 189, doi:10.1016/0550-3213(80)90214-X.
- [67] L. D. Landau, “On the angular momentum of a two-photon system”, *Dokl. Akad. Nauk* **60** (1948) 207.
- [68] C. N. Yang, “Selection Rules for the Dematerialization of a Particle into Two Photons”, *Phys. Rev.* **77** (1950) 242, doi:10.1103/PhysRev.77.242.

- [69] L. Randall and R. Sundrum, "An alternative to compactification", *Phys. Rev. Lett.* **83** (1999) 4690, doi:10.1103/PhysRevLett.83.4690, arXiv:hep-th/9906064.
- [70] L. Randall and R. Sundrum, "A large mass hierarchy from a small extra dimension", *Phys. Rev. Lett.* **83** (1999) 3370, doi:10.1103/PhysRevLett.83.3370, arXiv:hep-ph/9905221.
- [71] K. Agashe, H. Davoudiasl, G. Perez, and A. Soni, "Warped gravitons at the CERN LHC and beyond", *Phys. Rev. D* **76** (2007) 036006, doi:10.1103/PhysRevD.76.036006, arXiv:hep-ph/0701186.
- [72] N. Kauer and G. Passarino, "Inadequacy of zero-width approximation for a light Higgs boson signal", *JHEP* **08** (2012) 116, doi:10.1007/JHEP08(2012)116, arXiv:1206.4803.
- [73] F. Caola and K. Melnikov, "Constraining the Higgs boson width with ZZ production at the LHC", *Phys. Rev. D* **88** (2013) 054024, doi:10.1103/PhysRevD.88.054024, arXiv:1307.4935.
- [74] Particle Data Group, K. A. Olive et al., "Review of Particle Physics", *Chin. Phys. C* **38** (2014) 090001, doi:10.1088/1674-1137/38/9/090001.
- [75] CLEO Collaboration, "Experimental study of $\chi_b(2P) \rightarrow \pi\pi \chi_b(1P)$ ", *Phys. Rev. D* **73** (2006) 012003, doi:10.1103/PhysRevD.73.012003, arXiv:hep-ex/0511019.
- [76] S. G. Karshenboim, "Precision study of positronium: Testing bound state QED theory", *Int. J. Mod. Phys. A* **19** (2004) 3879, doi:10.1142/S0217751X04020142, arXiv:hep-ph/0310099.
- [77] CMS Collaboration, "The CMS experiment at the CERN LHC", *JINST* **3** (2008) S08004, doi:10.1088/1748-0221/3/08/S08004.
- [78] CMS Collaboration, "Measurement of inclusive W and Z boson production cross sections in pp collisions at $\sqrt{s} = 8$ TeV", *Phys. Rev. Lett.* **112** (2014) 191802, doi:10.1103/PhysRevLett.112.191802, arXiv:1402.0923.
- [79] CMS Collaboration, "CMS Luminosity Based on Pixel Cluster Counting - Summer 2013 Update", CMS Physics Analysis Summary CMS-PAS-LUM-13-001, 2013.
- [80] S. Frixione, P. Nason, and C. Oleari, "Matching NLO QCD computations with Parton Shower simulations: the POWHEG method", *JHEP* **11** (2007) 070, doi:10.1088/1126-6708/2007/11/070, arXiv:0709.2092.
- [81] E. Bagnaschi, G. Degrossi, P. Slavich, and A. Vicini, "Higgs production via gluon fusion in the POWHEG approach in the SM and in the MSSM", *JHEP* **02** (2012) 088, doi:10.1007/JHEP02(2012)088, arXiv:1111.2854.
- [82] P. Nason and C. Oleari, "NLO Higgs boson production via vector-boson fusion matched with shower in POWHEG", *JHEP* **02** (2010) 037, doi:10.1007/JHEP02(2010)037, arXiv:0911.5299.
- [83] T. Sjöstrand, S. Mrenna, and P. Skands, "PYTHIA 6.4 physics and manual", *JHEP* **05** (2006) 026, doi:10.1088/1126-6708/2006/05/026, arXiv:hep-ph/0603175.

- [84] GEANT4 Collaboration, "GEANT4—a simulation toolkit", *Nucl. Instrum. Meth. A* **506** (2003) 250, doi:10.1016/S0168-9002(03)01368-8.
- [85] T. Binoth, N. Kauer, and P. Mertsch, "Gluon-induced QCD corrections to $pp \rightarrow ZZ \rightarrow \ell\bar{\ell}\ell'\bar{\ell}'$ ", in *Proceedings of the XVI Int. Workshop on Deep-Inelastic Scattering and Related Topics (DIS'07)*. 2008. arXiv:0807.0024.
- [86] J. M. Campbell and R. K. Ellis, "MCFM for the Tevatron and the LHC", *Nucl. Phys. Proc. Suppl.* **205** (2010) 10, doi:10.1016/j.nuclphysbps.2010.08.011, arXiv:1007.3492.
- [87] J. M. Campbell, R. K. Ellis, and C. Williams, "Vector boson pair production at the LHC", *JHEP* **07** (2011) 018, doi:10.1007/JHEP07(2011)018, arXiv:1105.0020.
- [88] J. M. Campbell, R. K. Ellis, and C. Williams, "Bounding the Higgs width at the LHC using full analytic results for $gg \rightarrow e^-e^+\mu^-\mu^+$ ", *JHEP* **04** (2014) 060, doi:10.1007/JHEP04(2014)060, arXiv:1311.3589.
- [89] J. Alwall et al., "MadGraph 5: going beyond", *JHEP* **06** (2011) 128, doi:10.1007/JHEP06(2011)128, arXiv:1106.0522.
- [90] T. Binoth, M. Ciccolini, N. Kauer, and M. Krämer, "Gluon-induced W-boson pair production at the LHC", *JHEP* **12** (2006) 046, doi:10.1088/1126-6708/2006/12/046, arXiv:hep-ph/0611170.
- [91] A. Ballestrero et al., "PHANTOM: A Monte Carlo event generator for six parton final states at high energy colliders", *Comput. Phys. Comm.* **180** (2009) 3, doi:10.1016/j.cpc.2008.10.005, arXiv:hep-ph/0801.3359.
- [92] S. Jadach, J. H. Kuhn, and Z. Was, "TAUOLA - a library of Monte Carlo programs to simulate decays of polarized tau leptons", *Comput. Phys. Comm.* **64** (1991) 275, doi:10.1016/0010-4655(91)90038-M.
- [93] CMS Collaboration, "Particle-Flow Event Reconstruction in CMS and Performance for Jets, Taus, and MET", CMS Physics Analysis Summary CMS-PAS-PFT-09-001, 2009.
- [94] CMS Collaboration, "Commissioning of the Particle-flow Event Reconstruction with the first LHC collisions recorded in the CMS detector", CMS Physics Analysis Summary CMS-PAS-PFT-10-001, 2010.
- [95] CMS Collaboration, "Performance of CMS muon reconstruction in pp collision events at $\sqrt{s} = 7$ TeV", *JINST* **7** (2012) P10002, doi:10.1088/1748-0221/7/10/P10002, arXiv:1206.4071.
- [96] M. Cacciari, G. P. Salam, and G. Soyez, "The anti- k_t jet clustering algorithm", *JHEP* **04** (2008) 063, doi:10.1088/1126-6708/2008/04/063, arXiv:0802.1189.
- [97] M. Cacciari, G. P. Salam, and G. Soyez, "FastJet user manual", *Eur. Phys. J. C* **72** (2012) 1896, doi:10.1140/epjc/s10052-012-1896-2, arXiv:1111.6097.
- [98] P. Avery et al., "Precision studies of the Higgs boson decay channel $H \rightarrow ZZ^* \rightarrow 4\ell$ with MEKD", *Phys. Rev. D* **87** (2013) 055006, doi:10.1103/PhysRevD.87.055006, arXiv:1210.0896.

- [99] N. D. Christensen and C. Duhr, “FeynRules - Feynman rules made easy”, *Comput. Phys. Comm.* **180** (2009) 1614, doi:10.1016/j.cpc.2009.02.018, arXiv:0806.4194.
- [100] M. Rosenblatt, “Remarks on Some Nonparametric Estimates of a Density Function”, *Ann. Math. Stat.* **27** (1956) 832, doi:10.1214/aoms/1177728190.
- [101] E. Parzen, “On Estimation of a Probability Density Function and Mode”, *Ann. Math. Stat.* **33** (1962) 1065, doi:10.1214/aoms/1177704472.
- [102] S. S. Wilks, “The Large-Sample Distribution of the Likelihood Ratio for Testing Composite Hypotheses”, *Ann. Math. Stat.* **9** (1938) 60, doi:10.1214/aoms/1177732360.
- [103] A. L. Read, “Presentation of search results: the CL_s technique”, *J. Phys. G* **28** (2002) 2693, doi:10.1088/0954-3899/28/10/313.
- [104] T. Junk, “Confidence level computation for combining searches with small statistics”, *Nucl. Instrum. Meth. A* **434** (1999) 435, doi:10.1016/S0168-9002(99)00498-2, arXiv:hep-ex/9902006.
- [105] S. Heinemeyer et al., “Handbook of LHC Higgs cross sections: 3. Higgs properties”, CERN Report CERN-2013-004, 2013. doi:10.5170/CERN-2013-004, arXiv:1307.1347.
- [106] CMS Collaboration, “Measurement of the weak mixing angle with the Drell-Yan process in proton-proton collisions at the LHC”, *Phys. Rev. D* **84** (2011) 112002, doi:10.1103/PhysRevD.84.112002, arXiv:1110.2682.
- [107] CMS Collaboration, “Observation of Z decays to four leptons with the CMS detector at the LHC”, *JHEP* **12** (2012) 034, doi:10.1007/JHEP12(2012)034, arXiv:1210.3844.

A The CMS Collaboration

Yerevan Physics Institute, Yerevan, Armenia

V. Khachatryan, A.M. Sirunyan, A. Tumasyan

Institut für Hochenergiephysik der OeAW, Wien, Austria

W. Adam, T. Bergauer, M. Dragicevic, J. Erö, M. Friedl, R. Frühwirth¹, V.M. Ghete, C. Hartl, N. Hörmann, J. Hrubec, M. Jeitler¹, W. Kiesenhofer, V. Knünz, M. Krammer¹, I. Krätschmer, D. Liko, I. Mikulec, D. Rabadý², B. Rahbaran, H. Rohringer, R. Schöfbeck, J. Strauss, W. Treberer-Treberspurg, W. Waltenberger, C.-E. Wulz¹

National Centre for Particle and High Energy Physics, Minsk, Belarus

V. Mossolov, N. Shumeiko, J. Suarez Gonzalez

Universiteit Antwerpen, Antwerpen, Belgium

S. Alderweireldt, S. Bansal, T. Cornelis, E.A. De Wolf, X. Janssen, A. Knutsson, J. Lauwers, S. Luyckx, S. Ochesanu, R. Rougny, M. Van De Klundert, H. Van Haeevermaet, P. Van Mechelen, N. Van Remortel, A. Van Spilbeeck

Vrije Universiteit Brussel, Brussel, Belgium

F. Blekman, S. Blyweert, J. D'Hondt, N. Daci, N. Heracleous, J. Keaveney, S. Lowette, M. Maes, A. Olbrechts, Q. Python, D. Strom, S. Tavernier, W. Van Doninck, P. Van Mulders, G.P. Van Onsem, I. Vilella

Université Libre de Bruxelles, Bruxelles, Belgium

C. Caillol, B. Clerbaux, G. De Lentdecker, D. Dobur, L. Favart, A.P.R. Gay, A. Grebenyuk, A. Léonard, A. Mohammadi, L. Perniè², A. Randle-conde, T. Reis, T. Seva, L. Thomas, C. Vander Velde, P. Vanlaer, J. Wang, F. Zenoni

Ghent University, Ghent, Belgium

V. Adler, K. Beernaert, L. Benucci, A. Cimmino, S. Costantini, S. Crucy, S. Dildick, A. Fagot, G. Garcia, J. Mccartin, A.A. Ocampo Rios, D. Ryckbosch, S. Salva Diblen, M. Sigamani, N. Strobbe, F. Thyssen, M. Tytgat, E. Yazgan, N. Zaganidis

Université Catholique de Louvain, Louvain-la-Neuve, Belgium

S. Basegmez, C. Beluffi³, G. Bruno, R. Castello, A. Caudron, L. Ceard, G.G. Da Silveira, C. Delaere, T. du Pree, D. Favart, L. Forthomme, A. Giammanco⁴, J. Hollar, A. Jafari, P. Jez, M. Komm, V. Lemaitre, C. Nuttens, L. Perrini, A. Pin, K. Piotrkowski, A. Popov⁵, L. Quertenmont, M. Selvaggi, M. Vidal Marono, J.M. Vizan Garcia

Université de Mons, Mons, Belgium

N. Bely, T. Caebergs, E. Daubie, G.H. Hammad

Centro Brasileiro de Pesquisas Fisicas, Rio de Janeiro, Brazil

W.L. Aldá Júnior, G.A. Alves, L. Brito, M. Correa Martins Junior, T. Dos Reis Martins, J. Molina, C. Mora Herrera, M.E. Pol, P. Rebello Teles

Universidade do Estado do Rio de Janeiro, Rio de Janeiro, Brazil

W. Carvalho, J. Chinellato⁶, A. Custódio, E.M. Da Costa, D. De Jesus Damiao, C. De Oliveira Martins, S. Fonseca De Souza, H. Malbouisson, D. Matos Figueiredo, L. Mundim, H. Nogima, W.L. Prado Da Silva, J. Santaolalla, A. Santoro, A. Sznajder, E.J. Tonelli Manganote⁶, A. Vilela Pereira

Universidade Estadual Paulista ^a, Universidade Federal do ABC ^b, São Paulo, Brazil

C.A. Bernardes^b, S. Dogra^a, T.R. Fernandez Perez Tomei^a, E.M. Gregores^b, P.G. Mercadante^b, S.F. Novaes^a, Sandra S. Padula^a

Institute for Nuclear Research and Nuclear Energy, Sofia, Bulgaria

A. Aleksandrov, V. Genchev², R. Hadjiiska, P. Iaydjiev, A. Marinov, S. Piperov, M. Rodozov, G. Sultanov, M. Vutova

University of Sofia, Sofia, Bulgaria

A. Dimitrov, I. Glushkov, L. Litov, B. Pavlov, P. Petkov

Institute of High Energy Physics, Beijing, China

J.G. Bian, G.M. Chen, H.S. Chen, M. Chen, T. Cheng, R. Du, C.H. Jiang, R. Plestina⁷, F. Romeo, J. Tao, Z. Wang

State Key Laboratory of Nuclear Physics and Technology, Peking University, Beijing, China

C. Asawatangtrakuldee, Y. Ban, Q. Li, S. Liu, Y. Mao, S.J. Qian, D. Wang, Z. Xu, W. Zou

Universidad de Los Andes, Bogota, Colombia

C. Avila, A. Cabrera, L.F. Chaparro Sierra, C. Florez, J.P. Gomez, B. Gomez Moreno, J.C. Sanabria

University of Split, Faculty of Electrical Engineering, Mechanical Engineering and Naval Architecture, Split, Croatia

N. Godinovic, D. Lelas, D. Polic, I. Puljak

University of Split, Faculty of Science, Split, Croatia

Z. Antunovic, M. Kovac

Institute Rudjer Boskovic, Zagreb, Croatia

V. Brigljevic, K. Kadija, J. Luetic, D. Mekterovic, L. Sudic

University of Cyprus, Nicosia, Cyprus

A. Attikis, G. Mavromanolakis, J. Mousa, C. Nicolaou, F. Ptochos, P.A. Razis

Charles University, Prague, Czech Republic

M. Bodlak, M. Finger, M. Finger Jr.⁸

Academy of Scientific Research and Technology of the Arab Republic of Egypt, Egyptian Network of High Energy Physics, Cairo, Egypt

Y. Assran⁹, A. Ellithi Kamel¹⁰, M.A. Mahmoud¹¹, A. Radi^{12,13}

National Institute of Chemical Physics and Biophysics, Tallinn, Estonia

M. Kadastik, M. Murumaa, M. Raidal, A. Tiko

Department of Physics, University of Helsinki, Helsinki, Finland

P. Eerola, G. Fedi, M. Voutilainen

Helsinki Institute of Physics, Helsinki, Finland

J. Härkönen, V. Karimäki, R. Kinnunen, M.J. Kortelainen, T. Lampén, K. Lassila-Perini, S. Lehti, T. Lindén, P. Luukka, T. Mäenpää, T. Peltola, E. Tuominen, J. Tuominiemi, E. Tuovinen, L. Wendland

Lappeenranta University of Technology, Lappeenranta, Finland

J. Talvitie, T. Tuuva

DSM/IRFU, CEA/Saclay, Gif-sur-Yvette, France

M. Besancon, F. Couderc, M. Dejardin, D. Denegri, B. Fabbro, J.L. Faure, C. Favaro, F. Ferri, S. Ganjour, A. Givernaud, P. Gras, G. Hamel de Monchenault, P. Jarry, E. Locci, J. Malcles, J. Rander, A. Rosowsky, M. Titov

Laboratoire Leprince-Ringuet, Ecole Polytechnique, IN2P3-CNRS, Palaiseau, France

S. Baffioni, F. Beaudette, P. Busson, C. Charlot, T. Dahms, M. Dalchenko, L. Dobrzynski, N. Filipovic, A. Florent, R. Granier de Cassagnac, L. Mastrolorenzo, P. Miné, I.N. Naranjo, M. Nguyen, C. Ochando, G. Ortona, P. Paganini, S. Regnard, R. Salerno, J.B. Sauvan, Y. Sirois, C. Veelken, Y. Yilmaz, A. Zabi

Institut Pluridisciplinaire Hubert Curien, Université de Strasbourg, Université de Haute Alsace Mulhouse, CNRS/IN2P3, Strasbourg, France

J.-L. Agram¹⁴, J. Andrea, A. Aubin, D. Bloch, J.-M. Brom, E.C. Chabert, C. Collard, E. Conte¹⁴, J.-C. Fontaine¹⁴, D. Gelé, U. Goerlach, C. Goetzmann, A.-C. Le Bihan, K. Skovpen, P. Van Hove

Centre de Calcul de l'Institut National de Physique Nucleaire et de Physique des Particules, CNRS/IN2P3, Villeurbanne, France

S. Gadrat

Université de Lyon, Université Claude Bernard Lyon 1, CNRS-IN2P3, Institut de Physique Nucléaire de Lyon, Villeurbanne, France

S. Beauceron, N. Beaupere, C. Bernet⁷, G. Boudoul², E. Bouvier, S. Brochet, C.A. Carrillo Montoya, J. Chasserat, R. Chierici, D. Contardo², P. Depasse, H. El Mamouni, J. Fan, J. Fay, S. Gascon, M. Gouzevitch, B. Ille, T. Kurca, M. Lethuillier, L. Mirabito, S. Perries, J.D. Ruiz Alvarez, D. Sabes, L. Sgandurra, V. Sordini, M. Vander Donckt, P. Verdier, S. Viret, H. Xiao

Institute of High Energy Physics and Informatization, Tbilisi State University, Tbilisi, Georgia

Z. Tsamalaidze⁸

RWTH Aachen University, I. Physikalisches Institut, Aachen, Germany

C. Autermann, S. Beranek, M. Bontenackels, M. Edelhoff, L. Feld, A. Heister, O. Hindrichs, K. Klein, A. Ostapchuk, M. Preuten, F. Raupach, J. Sammet, S. Schael, J.F. Schulte, H. Weber, B. Wittmer, V. Zhukov⁵

RWTH Aachen University, III. Physikalisches Institut A, Aachen, Germany

M. Ata, M. Brodski, E. Dietz-Laursonn, D. Duchardt, M. Erdmann, R. Fischer, A. Güth, T. Hebbeker, C. Heidemann, K. Hoepfner, D. Klingebiel, S. Knutzen, P. Kreuzer, M. Merschmeyer, A. Meyer, P. Millet, M. Olschewski, K. Padeken, P. Papacz, H. Reithler, S.A. Schmitz, L. Sonnenschein, D. Teyssier, S. Thüer, M. Weber

RWTH Aachen University, III. Physikalisches Institut B, Aachen, Germany

V. Cherepanov, Y. Erdogan, G. Flügge, H. Geenen, M. Geisler, W. Haj Ahmad, F. Hoehle, B. Kargoll, T. Kress, Y. Kuessel, A. Künsken, J. Lingemann², A. Nowack, I.M. Nugent, O. Pooth, A. Stahl

Deutsches Elektronen-Synchrotron, Hamburg, Germany

M. Aldaya Martin, I. Asin, N. Bartosik, J. Behr, U. Behrens, A.J. Bell, A. Bethani, K. Borras, A. Burgmeier, A. Cakir, L. Calligaris, A. Campbell, S. Choudhury, F. Costanza, C. Diez Pardos, G. Dolinska, S. Dooling, T. Dorland, G. Eckerlin, D. Eckstein, T. Eichhorn, G. Flucke, J. Garay Garcia, A. Geiser, P. Gunnellini, J. Hauk, M. Hempel¹⁵, H. Jung, A. Kalogeropoulos, M. Kasemann, P. Katsas, J. Kieseler, C. Kleinwort, I. Korol, D. Krücker, W. Lange, J. Leonard, K. Lipka, A. Lobanov, W. Lohmann¹⁵, B. Lutz, R. Mankel, I. Marfin¹⁵, I.-A. Melzer-Pellmann,

A.B. Meyer, G. Mittag, J. Mnich, A. Mussgiller, S. Naumann-Emme, A. Nayak, E. Ntomari, H. Perrey, D. Pitzl, R. Placakyte, A. Raspereza, P.M. Ribeiro Cipriano, B. Roland, E. Ron, M.Ö. Sahin, J. Salfeld-Nebgen, P. Saxena, T. Schoerner-Sadenius, M. Schröder, C. Seitz, S. Spannagel, A.D.R. Vargas Trevino, R. Walsh, C. Wissing

University of Hamburg, Hamburg, Germany

V. Blobel, M. Centis Vignali, A.R. Draeger, J. Erfle, E. Garutti, K. Goebel, M. Görner, J. Haller, M. Hoffmann, R.S. Höing, A. Junkes, H. Kirschenmann, R. Klanner, R. Kogler, J. Lange, T. Lapsien, T. Lenz, I. Marchesini, J. Ott, T. Peiffer, A. Perieanu, N. Pietsch, J. Poehlsen, T. Poehlsen, D. Rathjens, C. Sander, H. Schettler, P. Schleper, E. Schlieckau, A. Schmidt, M. Seidel, V. Sola, H. Stadie, G. Steinbrück, D. Troendle, E. Usai, L. Vanelderen, A. Vanhoefer

Institut für Experimentelle Kernphysik, Karlsruhe, Germany

C. Barth, C. Baus, J. Berger, C. Böser, E. Butz, T. Chwalek, W. De Boer, A. Descroix, A. Dierlamm, M. Feindt, F. Frensch, M. Giffels, A. Gilbert, F. Hartmann², T. Hauth, U. Husemann, I. Katkov⁵, A. Kornmayer², E. Kuznetsova, P. Lobelle Pardo, M.U. Mozer, T. Müller, Th. Müller, A. Nürnberg, G. Quast, K. Rabbertz, S. Röcker, H.J. Simonis, F.M. Stober, R. Ulrich, J. Wagner-Kuhr, S. Wayand, T. Weiler, R. Wolf

Institute of Nuclear and Particle Physics (INPP), NCSR Demokritos, Aghia Paraskevi, Greece

G. Anagnostou, G. Daskalakis, T. Gerasis, V.A. Giakoumopoulou, A. Kyriakis, D. Loukas, A. Markou, C. Markou, A. Psallidas, I. Topsis-Giotis

University of Athens, Athens, Greece

A. Agapitos, S. Kesisoglou, A. Panagiotou, N. Saoulidou, E. Stiliaris

University of Ioánnina, Ioánnina, Greece

X. Aslanoglou, I. Evangelou, G. Flouris, C. Foudas, P. Kokkas, N. Manthos, I. Papadopoulos, E. Paradas, J. Strologas

Wigner Research Centre for Physics, Budapest, Hungary

G. Bencze, C. Hajdu, P. Hidas, D. Horvath¹⁶, F. Sikler, V. Veszpremi, G. Vesztergombi¹⁷, A.J. Zsigmond

Institute of Nuclear Research ATOMKI, Debrecen, Hungary

N. Beni, S. Czellar, J. Karancsi¹⁸, J. Molnar, J. Palinkas, Z. Szillasi

University of Debrecen, Debrecen, Hungary

A. Makovec, P. Raics, Z.L. Trocsanyi, B. Ujvari

National Institute of Science Education and Research, Bhubaneswar, India

S.K. Swain

Panjab University, Chandigarh, India

S.B. Beri, V. Bhatnagar, R. Gupta, U. Bhawandeep, A.K. Kalsi, M. Kaur, R. Kumar, M. Mittal, N. Nishu, J.B. Singh

University of Delhi, Delhi, India

Ashok Kumar, Arun Kumar, S. Ahuja, A. Bhardwaj, B.C. Choudhary, A. Kumar, S. Malhotra, M. Naimuddin, K. Ranjan, V. Sharma

Saha Institute of Nuclear Physics, Kolkata, India

S. Banerjee, S. Bhattacharya, K. Chatterjee, S. Dutta, B. Gomber, Sa. Jain, Sh. Jain, R. Khurana, A. Modak, S. Mukherjee, D. Roy, S. Sarkar, M. Sharan

Bhabha Atomic Research Centre, Mumbai, India

A. Abdulsalam, D. Dutta, V. Kumar, A.K. Mohanty², L.M. Pant, P. Shukla, A. Topkar

Tata Institute of Fundamental Research, Mumbai, India

T. Aziz, S. Banerjee, S. Bhowmik¹⁹, R.M. Chatterjee, R.K. Dewanjee, S. Dugad, S. Ganguly, S. Ghosh, M. Guchait, A. Gurtu²⁰, G. Kole, S. Kumar, M. Maity¹⁹, G. Majumder, K. Mazumdar, G.B. Mohanty, B. Parida, K. Sudhakar, N. Wickramage²¹

Institute for Research in Fundamental Sciences (IPM), Tehran, Iran

H. Bakhshiansohi, H. Behnamian, S.M. Etesami²², A. Fahim²³, R. Goldouzian, M. Khakzad, M. Mohammadi Najafabadi, M. Naseri, S. Paktinat Mehdiabadi, F. Rezaei Hosseinabadi, B. Safarzadeh²⁴, M. Zeinali

University College Dublin, Dublin, Ireland

M. Felcini, M. Grunewald

INFN Sezione di Bari ^a, Università di Bari ^b, Politecnico di Bari ^c, Bari, Italy

M. Abbrescia^{a,b}, C. Calabria^{a,b}, S.S. Chhibra^{a,b}, A. Colaleo^a, D. Creanza^{a,c}, N. De Filippis^{a,c}, M. De Palma^{a,b}, L. Fiore^a, G. Iaselli^{a,c}, G. Maggi^{a,c}, M. Maggi^a, S. My^{a,c}, S. Nuzzo^{a,b}, A. Pompili^{a,b}, G. Pugliese^{a,c}, R. Radogna^{a,b,2}, G. Selvaggi^{a,b}, A. Sharma^a, L. Silvestris^{a,2}, R. Venditti^{a,b}, P. Verwilligen^a

INFN Sezione di Bologna ^a, Università di Bologna ^b, Bologna, Italy

G. Abbiendi^a, A.C. Benvenuti^a, D. Bonacorsi^{a,b}, S. Braibant-Giacomelli^{a,b}, L. Brigliadori^{a,b}, R. Campanini^{a,b}, P. Capiluppi^{a,b}, A. Castro^{a,b}, F.R. Cavallo^a, G. Codispoti^{a,b}, M. Cuffiani^{a,b}, G.M. Dallavalle^a, F. Fabbri^a, A. Fanfani^{a,b}, D. Fasanella^{a,b}, P. Giacomelli^a, C. Grandi^a, L. Guiducci^{a,b}, S. Marcellini^a, G. Masetti^a, A. Montanari^a, F.L. Navarra^{a,b}, A. Perrotta^a, F. Primavera^{a,b}, A.M. Rossi^{a,b}, T. Rovelli^{a,b}, G.P. Siroli^{a,b}, N. Tosi^{a,b}, R. Travaglini^{a,b}

INFN Sezione di Catania ^a, Università di Catania ^b, CSFNSM ^c, Catania, Italy

S. Albergo^{a,b}, G. Cappello^a, M. Chiorboli^{a,b}, S. Costa^{a,b}, F. Giordano^{a,2}, R. Potenza^{a,b}, A. Tricomi^{a,b}, C. Tuve^{a,b}

INFN Sezione di Firenze ^a, Università di Firenze ^b, Firenze, Italy

G. Barbagli^a, V. Ciulli^{a,b}, C. Civinini^a, R. D'Alessandro^{a,b}, E. Focardi^{a,b}, E. Gallo^a, S. Gonzi^{a,b}, V. Gori^{a,b}, P. Lenzi^{a,b}, M. Meschini^a, S. Paoletti^a, G. Sguazzoni^a, A. Tropiano^{a,b}

INFN Laboratori Nazionali di Frascati, Frascati, Italy

L. Benussi, S. Bianco, F. Fabbri, D. Piccolo

INFN Sezione di Genova ^a, Università di Genova ^b, Genova, Italy

R. Ferretti^{a,b}, F. Ferro^a, M. Lo Vetere^{a,b}, E. Robutti^a, S. Tosi^{a,b}

INFN Sezione di Milano-Bicocca ^a, Università di Milano-Bicocca ^b, Milano, Italy

M.E. Dinardo^{a,b}, S. Fiorendi^{a,b}, S. Gennai^{a,2}, R. Gerosa^{a,b,2}, A. Ghezzi^{a,b}, P. Govoni^{a,b}, M.T. Lucchini^{a,b,2}, S. Malvezzi^a, R.A. Manzoni^{a,b}, A. Martelli^{a,b}, B. Marzocchi^{a,b,2}, D. Menasce^a, L. Moroni^a, M. Paganoni^{a,b}, D. Pedrini^a, S. Ragazzi^{a,b}, N. Redaelli^a, T. Tabarelli de Fatis^{a,b}

INFN Sezione di Napoli ^a, Università di Napoli 'Federico II' ^b, Università della Basilicata (Potenza) ^c, Università G. Marconi (Roma) ^d, Napoli, Italy

S. Buontempo^a, N. Cavallo^{a,c}, S. Di Guida^{a,d,2}, F. Fabozzi^{a,c}, A.O.M. Iorio^{a,b}, L. Lista^a, S. Meola^{a,d,2}, M. Merola^a, P. Paolucci^{a,2}

INFN Sezione di Padova ^a, Università di Padova ^b, Università di Trento (Trento) ^c, Padova, Italy

P. Azzi^a, N. Bacchetta^a, D. Bisello^{a,b}, A. Branca^{a,b}, R. Carlin^{a,b}, P. Checchia^a, M. Dall'Osso^{a,b}, T. Dorigo^a, U. Dosselli^a, M. Galanti^{a,b}, F. Gasparini^{a,b}, U. Gasparini^{a,b}, A. Gozzelino^a, K. Kanishchev^{a,c}, S. Lacaprara^a, M. Margoni^{a,b}, A.T. Meneguzzo^{a,b}, J. Pazzini^{a,b}, N. Pozzobon^{a,b}, P. Ronchese^{a,b}, F. Simonetto^{a,b}, E. Torassa^a, M. Tosi^{a,b}, P. Zotto^{a,b}, A. Zucchetta^{a,b}, G. Zumerle^{a,b}

INFN Sezione di Pavia ^a, Università di Pavia ^b, Pavia, Italy

M. Gabusi^{a,b}, S.P. Ratti^{a,b}, V. Re^a, C. Riccardi^{a,b}, P. Salvini^a, P. Vitulo^{a,b}

INFN Sezione di Perugia ^a, Università di Perugia ^b, Perugia, Italy

M. Biasini^{a,b}, G.M. Bilei^a, D. Ciangottini^{a,b,2}, L. Fanò^{a,b}, P. Lariccia^{a,b}, G. Mantovani^{a,b}, M. Menichelli^a, A. Saha^a, A. Santocchia^{a,b}, A. Spiezia^{a,b,2}

INFN Sezione di Pisa ^a, Università di Pisa ^b, Scuola Normale Superiore di Pisa ^c, Pisa, Italy

K. Androsov^{a,25}, P. Azzurri^a, G. Bagliesi^a, J. Bernardini^a, T. Boccali^a, G. Broccolo^{a,c}, R. Castaldi^a, M.A. Ciocci^{a,25}, R. Dell'Orso^a, S. Donato^{a,c,2}, F. Fiori^{a,c}, L. Foà^{a,c}, A. Giassi^a, M.T. Grippo^{a,25}, F. Ligabue^{a,c}, T. Lomtadze^a, L. Martini^{a,b}, A. Messineo^{a,b}, C.S. Moon^{a,26}, F. Palla^{a,2}, A. Rizzi^{a,b}, A. Savoy-Navarro^{a,27}, A.T. Serban^a, P. Spagnolo^a, P. Squillacioti^{a,25}, R. Tenchini^a, G. Tonelli^{a,b}, A. Venturi^a, P.G. Verdini^a, C. Vernieri^{a,c}

INFN Sezione di Roma ^a, Università di Roma ^b, Roma, Italy

L. Barone^{a,b}, F. Cavallari^a, G. D'imperio^{a,b}, D. Del Re^{a,b}, M. Diemoz^a, C. Jorda^a, E. Longo^{a,b}, E. Margaroli^{a,b}, P. Meridiani^a, F. Micheli^{a,b,2}, G. Organtini^{a,b}, R. Paramatti^a, S. Rahatlou^{a,b}, C. Rovelli^a, F. Santanastasio^{a,b}, L. Soffi^{a,b}, P. Traczyk^{a,b,2}

INFN Sezione di Torino ^a, Università di Torino ^b, Università del Piemonte Orientale (Novara) ^c, Torino, Italy

N. Amapane^{a,b}, R. Arcidiacono^{a,c}, S. Argiro^{a,b}, M. Arneodo^{a,c}, R. Bellan^{a,b}, C. Biino^a, N. Cartiglia^a, S. Casasso^{a,b,2}, M. Costa^{a,b}, A. Degano^{a,b}, N. Demaria^a, L. Finco^{a,b,2}, C. Mariotti^a, S. Maselli^a, E. Migliore^{a,b}, V. Monaco^{a,b}, M. Musich^a, M.M. Obertino^{a,c}, L. Pacher^{a,b}, N. Pastrone^a, M. Pelliccioni^a, G.L. Pinna Angioni^{a,b}, A. Potenza^{a,b}, A. Romero^{a,b}, M. Ruspa^{a,c}, R. Sacchi^{a,b}, A. Solano^{a,b}, A. Staiano^a, U. Tamponi^a

INFN Sezione di Trieste ^a, Università di Trieste ^b, Trieste, Italy

S. Belforte^a, V. Candelise^{a,b,2}, M. Casarsa^a, F. Cossutti^a, G. Della Ricca^{a,b}, B. Gobbo^a, C. La Licata^{a,b}, M. Marone^{a,b}, A. Schizzi^{a,b}, T. Umer^{a,b}, A. Zanetti^a

Kangwon National University, Chunchon, Korea

S. Chang, A. Kropivnitskaya, S.K. Nam

Kyungpook National University, Daegu, Korea

D.H. Kim, G.N. Kim, M.S. Kim, D.J. Kong, S. Lee, Y.D. Oh, H. Park, A. Sakharov, D.C. Son

Chonbuk National University, Jeonju, Korea

T.J. Kim, M.S. Ryu

Chonnam National University, Institute for Universe and Elementary Particles, Kwangju, Korea

J.Y. Kim, D.H. Moon, S. Song

Korea University, Seoul, Korea

S. Choi, D. Gyun, B. Hong, M. Jo, H. Kim, Y. Kim, B. Lee, K.S. Lee, S.K. Park, Y. Roh

Seoul National University, Seoul, Korea

H.D. Yoo

University of Seoul, Seoul, Korea

M. Choi, J.H. Kim, I.C. Park, G. Ryu

Sungkyunkwan University, Suwon, Korea

Y. Choi, Y.K. Choi, J. Goh, D. Kim, E. Kwon, J. Lee, I. Yu

Vilnius University, Vilnius, Lithuania

A. Juodagalvis

National Centre for Particle Physics, Universiti Malaya, Kuala Lumpur, Malaysia

J.R. Komaragiri, M.A.B. Md Ali

Centro de Investigacion y de Estudios Avanzados del IPN, Mexico City, Mexico

E. Casimiro Linares, H. Castilla-Valdez, E. De La Cruz-Burelo, I. Heredia-de La Cruz, A. Hernandez-Almada, R. Lopez-Fernandez, A. Sanchez-Hernandez

Universidad Iberoamericana, Mexico City, Mexico

S. Carrillo Moreno, F. Vazquez Valencia

Benemerita Universidad Autonoma de Puebla, Puebla, Mexico

I. Pedraza, H.A. Salazar Ibarguen

Universidad Autónoma de San Luis Potosí, San Luis Potosí, Mexico

A. Morelos Pineda

University of Auckland, Auckland, New Zealand

D. Krofcheck

University of Canterbury, Christchurch, New Zealand

P.H. Butler, S. Reucroft

National Centre for Physics, Quaid-I-Azam University, Islamabad, Pakistan

A. Ahmad, M. Ahmad, Q. Hassan, H.R. Hoorani, W.A. Khan, T. Khurshid, M. Shoaib

National Centre for Nuclear Research, Swierk, Poland

H. Bialkowska, M. Bluj, B. Boimska, T. Frueboes, M. Górski, M. Kazana, K. Nawrocki, K. Romanowska-Rybinska, M. Szleper, P. Zalewski

Institute of Experimental Physics, Faculty of Physics, University of Warsaw, Warsaw, Poland

G. Brona, K. Bunkowski, M. Cwiok, W. Dominik, K. Doroba, A. Kalinowski, M. Konecki, J. Krolikowski, M. Misiura, M. Olszewski

Laboratório de Instrumentação e Física Experimental de Partículas, Lisboa, Portugal

P. Bargassa, C. Beirão Da Cruz E Silva, P. Faccioli, P.G. Ferreira Parracho, M. Gallinaro, L. Lloret Iglesias, F. Nguyen, J. Rodrigues Antunes, J. Seixas, J. Varela, P. Vischia

Joint Institute for Nuclear Research, Dubna, Russia

S. Afanasiev, P. Bunin, M. Gavrilenko, I. Golutvin, I. Gorbunov, A. Kamenev, V. Karjavin, V. Konoplyanikov, A. Lanev, A. Malakhov, V. Matveev²⁸, P. Moisezenz, V. Palichik, V. Perelygin, S. Shmatov, N. Skatchkov, V. Smirnov, A. Zarubin

Petersburg Nuclear Physics Institute, Gatchina (St. Petersburg), Russia

V. Golovtsov, Y. Ivanov, V. Kim²⁹, P. Levchenko, V. Murzin, V. Oreshkin, I. Smirnov, V. Sulimov, L. Uvarov, S. Vavilov, A. Vorobyev, An. Vorobyev

Institute for Nuclear Research, Moscow, Russia

Yu. Andreev, A. Dermenev, S. Gninenko, N. Golubev, M. Kirsanov, N. Krasnikov, A. Pashenkov, D. Tlisov, A. Toropin

Institute for Theoretical and Experimental Physics, Moscow, Russia

V. Epshteyn, V. Gavrilov, N. Lychkovskaya, V. Popov, I. Pozdnyakov, G. Safronov, S. Semenov, A. Spiridonov, V. Stolin, E. Vlasov, A. Zhokin

P.N. Lebedev Physical Institute, Moscow, Russia

V. Andreev, M. Azarkin³⁰, I. Dremin³⁰, M. Kirakosyan, A. Leonidov³⁰, G. Mesyats, S.V. Rusakov, A. Vinogradov

Skobeltsyn Institute of Nuclear Physics, Lomonosov Moscow State University, Moscow, Russia

A. Belyaev, E. Boos, V. Bunichev, M. Dubinin³¹, L. Dudko, A. Gribushin, V. Klyukhin, O. Kodolova, I. Lokhtin, S. Obraztsov, M. Perfilov, S. Petrushanko, V. Savrin

State Research Center of Russian Federation, Institute for High Energy Physics, Protvino, Russia

I. Azhgirey, I. Bayshev, S. Bitioukov, V. Kachanov, A. Kalinin, D. Konstantinov, V. Krychkine, V. Petrov, R. Ryutin, A. Sobol, L. Tourtchanovitch, S. Troshin, N. Tyurin, A. Uzunian, A. Volkov

University of Belgrade, Faculty of Physics and Vinca Institute of Nuclear Sciences, Belgrade, Serbia

P. Adzic³², M. Ekmedzic, J. Milosevic, V. Rekovic

Centro de Investigaciones Energéticas Medioambientales y Tecnológicas (CIEMAT), Madrid, Spain

J. Alcaraz Maestre, C. Battilana, E. Calvo, M. Cerrada, M. Chamizo Llatas, N. Colino, B. De La Cruz, A. Delgado Peris, D. Domínguez Vázquez, A. Escalante Del Valle, C. Fernandez Bedoya, J.P. Fernández Ramos, J. Flix, M.C. Fouz, P. Garcia-Abia, O. Gonzalez Lopez, S. Goy Lopez, J.M. Hernandez, M.I. Josa, E. Navarro De Martino, A. Pérez-Calero Yzquierdo, J. Puerta Pelayo, A. Quintario Olmeda, I. Redondo, L. Romero, M.S. Soares

Universidad Autónoma de Madrid, Madrid, Spain

C. Albajar, J.F. de Trocóniz, M. Missiroli, D. Moran

Universidad de Oviedo, Oviedo, Spain

H. Brun, J. Cuevas, J. Fernandez Menendez, S. Folgueras, I. Gonzalez Caballero

Instituto de Física de Cantabria (IFCA), CSIC-Universidad de Cantabria, Santander, Spain

J.A. Brochero Cifuentes, I.J. Cabrillo, A. Calderon, J. Duarte Campderros, M. Fernandez, G. Gomez, A. Graziano, A. Lopez Virto, J. Marco, R. Marco, C. Martinez Rivero, F. Matorras, F.J. Munoz Sanchez, J. Piedra Gomez, T. Rodrigo, A.Y. Rodríguez-Marrero, A. Ruiz-Jimeno, L. Scodellaro, I. Vila, R. Vilar Cortabitarte

CERN, European Organization for Nuclear Research, Geneva, Switzerland

D. Abbaneo, E. Auffray, G. Auzinger, M. Bachtis, P. Baillon, A.H. Ball, D. Barney, A. Benaglia, J. Bendavid, L. Benhabib, J.F. Benitez, P. Bloch, A. Bocci, A. Bonato, O. Bondu, C. Botta, H. Breuker, T. Camporesi, G. Cerminara, S. Colafranceschi³³, M. D'Alfonso, D. d'Enterria, A. Dabrowski, A. David, F. De Guio, A. De Roeck, S. De Visscher, E. Di Marco, M. Dobson, M. Dordevic, B. Dorney, N. Dupont-Sagorin, A. Elliott-Peisert, G. Franzoni, W. Funk, D. Gigi, K. Gill, D. Giordano, M. Girone, F. Glege, R. Guida, S. Gundacker, M. Guthoff, J. Hammer, M. Hansen, P. Harris, J. Hegeman, V. Innocente, P. Janot, K. Kousouris, K. Krajczar, P. Lecoq,

C. Lourenço, N. Magini, L. Malgeri, M. Mannelli, J. Marrouche, L. Masetti, F. Meijers, S. Mersi, E. Meschi, F. Moortgat, S. Morovic, M. Mulders, L. Orsini, L. Pape, E. Perez, A. Petrilli, G. Petrucciani, A. Pfeiffer, M. Pimiä, D. Piparo, M. Plagge, A. Racz, G. Rolandi³⁴, M. Rovere, H. Sakulin, C. Schäfer, C. Schwick, A. Sharma, P. Siegrist, P. Silva, M. Simon, P. Sphicas³⁵, D. Spiga, J. Steggemann, B. Stieger, M. Stoye, Y. Takahashi, D. Treille, A. Tsirou, G.I. Veres¹⁷, N. Wardle, H.K. Wöhri, H. Wollny, W.D. Zeuner

Paul Scherrer Institut, Villigen, Switzerland

W. Bertl, K. Deiters, W. Erdmann, R. Horisberger, Q. Ingram, H.C. Kaestli, D. Kotlinski, U. Langenegger, D. Renker, T. Rohe

Institute for Particle Physics, ETH Zurich, Zurich, Switzerland

F. Bachmair, L. Bäni, L. Bianchini, M.A. Buchmann, B. Casal, N. Chanon, G. Dissertori, M. Dittmar, M. Donegà, M. Dünser, P. Eller, C. Grab, D. Hits, J. Hoss, W. Luster, B. Mangano, A.C. Marini, M. Marionneau, P. Martinez Ruiz del Arbol, M. Masciovecchio, D. Meister, N. Mohr, P. Musella, C. Nägeli³⁶, F. Nessi-Tedaldi, F. Pandolfi, F. Pauss, L. Perrozzi, M. Peruzzi, M. Quittnat, L. Rebane, M. Rossini, A. Starodumov³⁷, M. Takahashi, K. Theofilatos, R. Wallny, H.A. Weber

Universität Zürich, Zurich, Switzerland

C. Amsler³⁸, M.F. Canelli, V. Chiochia, A. De Cosa, A. Hinzmann, T. Hreus, B. Kilminster, C. Lange, B. Millan Mejias, J. Ngadiuba, D. Pinna, P. Robmann, F.J. Ronga, S. Taroni, M. Verzetti, Y. Yang

National Central University, Chung-Li, Taiwan

M. Cardaci, K.H. Chen, C. Ferro, C.M. Kuo, W. Lin, Y.J. Lu, R. Volpe, S.S. Yu

National Taiwan University (NTU), Taipei, Taiwan

P. Chang, Y.H. Chang, Y.W. Chang, Y. Chao, K.F. Chen, P.H. Chen, C. Dietz, U. Grundler, W.-S. Hou, K.Y. Kao, Y.F. Liu, R.-S. Lu, E. Petrakou, Y.M. Tzeng, R. Wilken

Chulalongkorn University, Faculty of Science, Department of Physics, Bangkok, Thailand

B. Asavapibhop, G. Singh, N. Srimanobhas, N. Suwonjandee

Cukurova University, Adana, Turkey

A. Adiguzel, M.N. Bakirci³⁹, S. Cerci⁴⁰, C. Dozen, I. Dumanoglu, E. Eskut, S. Girgis, G. Gokbulut, Y. Guler, E. Gurpinar, I. Hos, E.E. Kangal, A. Kayis Topaksu, G. Onengut⁴¹, K. Ozdemir, S. Ozturk³⁹, A. Polatoz, D. Sunar Cerci⁴⁰, B. Tali⁴⁰, H. Topakli³⁹, M. Vergili, C. Zorbilmez

Middle East Technical University, Physics Department, Ankara, Turkey

I.V. Akin, B. Bilin, S. Bilmis, H. Gamsizkan⁴², B. Isildak⁴³, G. Karapinar⁴⁴, K. Ocalan⁴⁵, S. Sekmen, U.E. Surat, M. Yalvac, M. Zeyrek

Bogazici University, Istanbul, Turkey

E.A. Albayrak⁴⁶, E. Gülmez, M. Kaya⁴⁷, O. Kaya⁴⁸, T. Yetkin⁴⁹

Istanbul Technical University, Istanbul, Turkey

K. Cankocak, F.I. Vardarli

National Scientific Center, Kharkov Institute of Physics and Technology, Kharkov, Ukraine

L. Levchuk, P. Sorokin

University of Bristol, Bristol, United Kingdom

J.J. Brooke, E. Clement, D. Cussans, H. Flacher, J. Goldstein, M. Grimes, G.P. Heath, H.F. Heath,

J. Jacob, L. Kreczko, C. Lucas, Z. Meng, D.M. Newbold⁵⁰, S. Paramesvaran, A. Poll, T. Sakuma, S. Seif El Nasr-storey, S. Senkin, V.J. Smith

Rutherford Appleton Laboratory, Didcot, United Kingdom

K.W. Bell, A. Belyaev⁵¹, C. Brew, R.M. Brown, D.J.A. Cockerill, J.A. Coughlan, K. Harder, S. Harper, E. Olaiya, D. Petyt, C.H. Shepherd-Themistocleous, A. Thea, I.R. Tomalin, T. Williams, W.J. Womersley, S.D. Worm

Imperial College, London, United Kingdom

M. Baber, R. Bainbridge, O. Buchmuller, D. Burton, D. Colling, N. Cripps, P. Dauncey, G. Davies, M. Della Negra, P. Dunne, W. Ferguson, J. Fulcher, D. Futyan, G. Hall, G. Iles, M. Jarvis, G. Karapostoli, M. Kenzie, R. Lane, R. Lucas⁵⁰, L. Lyons, A.-M. Magnan, S. Malik, B. Mathias, J. Nash, A. Nikitenko³⁷, J. Pela, M. Pesaresi, K. Petridis, D.M. Raymond, S. Rogerson, A. Rose, C. Seez, P. Sharp[†], A. Tapper, M. Vazquez Acosta, T. Virdee, S.C. Zenz

Brunel University, Uxbridge, United Kingdom

J.E. Cole, P.R. Hobson, A. Khan, P. Kyberd, D. Leggat, D. Leslie, I.D. Reid, P. Symonds, L. Teodorescu, M. Turner

Baylor University, Waco, USA

J. Dittmann, K. Hatakeyama, A. Kasmi, H. Liu, T. Scarborough

The University of Alabama, Tuscaloosa, USA

O. Charaf, S.I. Cooper, C. Henderson, P. Rumerio

Boston University, Boston, USA

A. Avetisyan, T. Bose, C. Fantasia, P. Lawson, C. Richardson, J. Rohlf, J. St. John, L. Sulak

Brown University, Providence, USA

J. Alimena, E. Berry, S. Bhattacharya, G. Christopher, D. Cutts, Z. Demiragli, N. Dhingra, A. Ferapontov, A. Garabedian, U. Heintz, G. Kukartsev, E. Laird, G. Landsberg, M. Luk, M. Narain, M. Segala, T. Sinthuprasith, T. Speer, J. Swanson

University of California, Davis, Davis, USA

R. Breedon, G. Breto, M. Calderon De La Barca Sanchez, S. Chauhan, M. Chertok, J. Conway, R. Conway, P.T. Cox, R. Erbacher, M. Gardner, W. Ko, R. Lander, M. Mulhearn, D. Pellett, J. Pilot, F. Ricci-Tam, S. Shalhout, J. Smith, M. Squires, D. Stolp, M. Tripathi, S. Wilbur, R. Yohay

University of California, Los Angeles, USA

R. Cousins, P. Everaerts, C. Farrell, J. Hauser, M. Ignatenko, G. Rakness, E. Takasugi, V. Valuev, M. Weber

University of California, Riverside, Riverside, USA

K. Burt, R. Clare, J. Ellison, J.W. Gary, G. Hanson, J. Heilman, M. Ivova Rikova, P. Jandir, E. Kennedy, F. Lacroix, O.R. Long, A. Luthra, M. Malberti, M. Olmedo Negrete, A. Shrinivas, S. Sumowidagdo, S. Wimpenny

University of California, San Diego, La Jolla, USA

J.G. Branson, G.B. Cerati, S. Cittolin, R.T. D'Agnolo, A. Holzner, R. Kelley, D. Klein, J. Letts, I. Macneill, D. Olivito, S. Padhi, C. Palmer, M. Pieri, M. Sani, V. Sharma, S. Simon, M. Tadel, Y. Tu, A. Vartak, C. Welke, F. Würthwein, A. Yagil

University of California, Santa Barbara, Santa Barbara, USA

D. Barge, J. Bradmiller-Feld, C. Campagnari, T. Danielson, A. Dishaw, V. Dutta, K. Flowers,

M. Franco Sevilla, P. Geffert, C. George, F. Golf, L. Gouskos, J. Incandela, C. Justus, N. Mccoll, J. Richman, D. Stuart, W. To, C. West, J. Yoo

California Institute of Technology, Pasadena, USA

A. Apresyan, A. Bornheim, J. Bunn, Y. Chen, J. Duarte, A. Mott, H.B. Newman, C. Pena, M. Pierini, M. Spiropulu, J.R. Vlimant, R. Wilkinson, S. Xie, R.Y. Zhu

Carnegie Mellon University, Pittsburgh, USA

V. Azzolini, A. Calamba, B. Carlson, T. Ferguson, Y. Iiyama, M. Paulini, J. Russ, H. Vogel, I. Vorobiev

University of Colorado at Boulder, Boulder, USA

J.P. Cumalat, W.T. Ford, A. Gaz, M. Krohn, E. Luiggi Lopez, U. Nauenberg, J.G. Smith, K. Stenson, S.R. Wagner

Cornell University, Ithaca, USA

J. Alexander, A. Chatterjee, J. Chaves, J. Chu, S. Dittmer, N. Eggert, N. Mirman, G. Nicolas Kaufman, J.R. Patterson, A. Ryd, E. Salvati, L. Skinnari, W. Sun, W.D. Teo, J. Thom, J. Thompson, J. Tucker, Y. Weng, L. Winstrom, P. Wittich

Fairfield University, Fairfield, USA

D. Winn

Fermi National Accelerator Laboratory, Batavia, USA

S. Abdullin, M. Albrow, J. Anderson, G. Apollinari, L.A.T. Bauerdick, A. Beretvas, J. Berryhill, P.C. Bhat, G. Bolla, K. Burkett, J.N. Butler, H.W.K. Cheung, F. Chlebana, S. Cihangir, V.D. Elvira, I. Fisk, J. Freeman, Y. Gao, E. Gottschalk, L. Gray, D. Green, S. Grünendahl, O. Gutsche, J. Hanlon, D. Hare, R.M. Harris, J. Hirschauer, B. Hooberman, S. Jindariani, M. Johnson, U. Joshi, B. Klima, B. Kreis, S. Kwan[†], J. Linacre, D. Lincoln, R. Lipton, T. Liu, J. Lykken, K. Maeshima, J.M. Marraffino, V.I. Martinez Outschoorn, S. Maruyama, D. Mason, P. McBride, P. Merkel, K. Mishra, S. Mrenna, S. Nahn, C. Newman-Holmes, V. O'Dell, O. Prokofyev, E. Sexton-Kennedy, S. Sharma, A. Soha, W.J. Spalding, L. Spiegel, L. Taylor, S. Tkaczyk, N.V. Tran, L. Uplegger, E.W. Vaandering, R. Vega Morales⁵², R. Vidal, A. Whitbeck, J. Whitmore, F. Yang

University of Florida, Gainesville, USA

D. Acosta, P. Avery, P. Bortignon, D. Bourilkov, M. Carver, D. Curry, S. Das, M. De Gruttola, G.P. Di Giovanni, R.D. Field, M. Fisher, I.K. Furic, J. Hugon, J. Konigsberg, A. Korytov, T. Kypreos, J.F. Low, K. Matchev, H. Mei, P. Milenovic⁵³, G. Mitselmakher, L. Muniz, A. Rinkevicius, L. Shchutska, M. Snowball, D. Sperka, J. Yelton, M. Zakaria

Florida International University, Miami, USA

S. Hewamanage, S. Linn, P. Markowitz, G. Martinez, J.L. Rodriguez

Florida State University, Tallahassee, USA

T. Adams, A. Askew, J. Bochenek, B. Diamond, J. Haas, S. Hagopian, V. Hagopian, K.F. Johnson, H. Prosper, V. Veeraraghavan, M. Weinberg

Florida Institute of Technology, Melbourne, USA

M.M. Baarmand, M. Hohmann, H. Kalakhety, F. Yumiceva

University of Illinois at Chicago (UIC), Chicago, USA

M.R. Adams, L. Apanasevich, D. Berry, R.R. Betts, I. Bucinskaite, R. Cavanaugh, O. Evdokimov, L. Gauthier, C.E. Gerber, D.J. Hofman, P. Kurt, C. O'Brien, I.D. Sandoval Gonzalez, C. Silkworth, P. Turner, N. Varelas

The University of Iowa, Iowa City, USA

B. Bilki⁵⁴, W. Clarida, K. Dilsiz, M. Haytmyradov, J.-P. Merlo, H. Mermerkaya⁵⁵, A. Mestvirishvili, A. Moeller, J. Nachtman, H. Ogul, Y. Onel, F. Ozok⁴⁶, A. Penzo, R. Rahmat, S. Sen, P. Tan, E. Tiras, J. Wetzel, K. Yi

Johns Hopkins University, Baltimore, USA

I. Anderson, B.A. Barnett, B. Blumenfeld, S. Bolognesi, D. Fehling, A.V. Gritsan, P. Maksimovic, C. Martin, J. Roskes, U. Sarica, M. Swartz, M. Xiao, C. You

The University of Kansas, Lawrence, USA

P. Baringer, A. Bean, G. Benelli, C. Bruner, J. Gray, R.P. Kenny III, D. Majumder, M. Malek, M. Murray, D. Noonan, S. Sanders, J. Sekaric, R. Stringer, Q. Wang, J.S. Wood

Kansas State University, Manhattan, USA

I. Chakaberia, A. Ivanov, K. Kaadze, S. Khalil, M. Makouski, Y. Maravin, L.K. Saini, N. Skhirtladze, I. Svintradze

Lawrence Livermore National Laboratory, Livermore, USA

J. Gronberg, D. Lange, F. Rebassoo, D. Wright

University of Maryland, College Park, USA

A. Baden, A. Belloni, B. Calvert, S.C. Eno, J.A. Gomez, N.J. Hadley, R.G. Kellogg, T. Kolberg, Y. Lu, A.C. Mignerey, K. Pedro, A. Skuja, M.B. Tonjes, S.C. Tonwar

Massachusetts Institute of Technology, Cambridge, USA

A. Apyan, R. Barbieri, W. Busza, I.A. Cali, M. Chan, L. Di Matteo, G. Gomez Ceballos, M. Goncharov, D. Gulhan, M. Klute, Y.S. Lai, Y.-J. Lee, A. Levin, P.D. Luckey, C. Paus, D. Ralph, C. Roland, G. Roland, G.S.F. Stephans, K. Sumorok, D. Velicanu, J. Veverka, B. Wyslouch, M. Yang, M. Zanetti, V. Zhukova

University of Minnesota, Minneapolis, USA

B. Dahmes, A. Gude, S.C. Kao, K. Klapoetke, Y. Kubota, J. Mans, S. Nourbakhsh, N. Pastika, R. Rusack, A. Singovsky, N. Tambe, J. Turkewitz

University of Mississippi, Oxford, USA

J.G. Acosta, S. Oliveros

University of Nebraska-Lincoln, Lincoln, USA

E. Avdeeva, K. Bloom, S. Bose, D.R. Claes, A. Dominguez, R. Gonzalez Suarez, J. Keller, D. Knowlton, I. Kravchenko, J. Lazo-Flores, F. Meier, F. Ratnikov, G.R. Snow, M. Zvada

State University of New York at Buffalo, Buffalo, USA

J. Dolen, A. Godshalk, I. Iashvili, A. Kharchilava, A. Kumar, S. Rappoccio

Northeastern University, Boston, USA

G. Alverson, E. Barberis, D. Baumgartel, M. Chasco, A. Massironi, D.M. Morse, D. Nash, T. Orimoto, D. Trocino, R.-J. Wang, D. Wood, J. Zhang

Northwestern University, Evanston, USA

K.A. Hahn, A. Kubik, N. Mucia, N. Odell, B. Pollack, A. Pozdnyakov, M. Schmitt, S. Stoynev, K. Sung, M. Velasco, S. Won

University of Notre Dame, Notre Dame, USA

A. Brinkerhoff, K.M. Chan, A. Drozdetskiy, M. Hildreth, C. Jessop, D.J. Karmgard, N. Kellams, K. Lannon, S. Lynch, N. Marinelli, Y. Musienko²⁸, T. Pearson, M. Planer, R. Ruchti, G. Smith, N. Valls, M. Wayne, M. Wolf, A. Woodard

The Ohio State University, Columbus, USA

L. Antonelli, J. Brinson, B. Bylsma, L.S. Durkin, S. Flowers, A. Hart, C. Hill, R. Hughes, K. Kotov, T.Y. Ling, W. Luo, D. Puigh, M. Rodenburg, B.L. Winer, H. Wolfe, H.W. Wulsin

Princeton University, Princeton, USA

O. Driga, P. Elmer, J. Hardenbrook, P. Hebda, S.A. Koay, P. Lujan, D. Marlow, T. Medvedeva, M. Mooney, J. Olsen, P. Piroué, X. Quan, H. Saka, D. Stickland², C. Tully, J.S. Werner, A. Zuranski

University of Puerto Rico, Mayaguez, USA

E. Brownson, S. Malik, H. Mendez, J.E. Ramirez Vargas

Purdue University, West Lafayette, USA

V.E. Barnes, D. Benedetti, D. Bortoletto, M. De Mattia, L. Gutay, Z. Hu, M.K. Jha, M. Jones, K. Jung, M. Kress, N. Leonardo, D.H. Miller, N. Neumeister, B.C. Radburn-Smith, X. Shi, I. Shipsey, D. Silvers, A. Svyatkovskiy, F. Wang, W. Xie, L. Xu, J. Zablocki

Purdue University Calumet, Hammond, USA

N. Parashar, J. Stupak

Rice University, Houston, USA

A. Adair, B. Akgun, K.M. Ecklund, F.J.M. Geurts, W. Li, B. Michlin, B.P. Padley, R. Redjimi, J. Roberts, J. Zabel

University of Rochester, Rochester, USA

B. Betchart, A. Bodek, R. Covarelli, P. de Barbaro, R. Demina, Y. Eshaq, T. Ferbel, A. Garcia-Bellido, P. Goldenzweig, J. Han, A. Harel, A. Khukhunaishvili, S. Korjenevski, G. Petrillo, D. Vishnevskiy

The Rockefeller University, New York, USA

R. Ciesielski, L. Demortier, K. Goulianos, C. Mesropian

Rutgers, The State University of New Jersey, Piscataway, USA

S. Arora, A. Barker, J.P. Chou, C. Contreras-Campana, E. Contreras-Campana, D. Duggan, D. Ferencek, Y. Gershtein, R. Gray, E. Halkiadakis, D. Hidas, S. Kaplan, A. Lath, S. Panwalkar, M. Park, R. Patel, S. Salur, S. Schnetzer, D. Sheffield, S. Somalwar, R. Stone, S. Thomas, P. Thomassen, M. Walker

University of Tennessee, Knoxville, USA

K. Rose, S. Spanier, A. York

Texas A&M University, College Station, USA

O. Bouhali⁵⁶, A. Castaneda Hernandez, R. Eusebi, W. Flanagan, J. Gilmore, T. Kamon⁵⁷, V. Khotilovich, V. Krutelyov, R. Montalvo, I. Osipenkov, Y. Pakhotin, A. Perloff, J. Roe, A. Rose, A. Safonov, I. Suarez, A. Tatarinov, K.A. Ulmer

Texas Tech University, Lubbock, USA

N. Akchurin, C. Cowden, J. Damgov, C. Dragoiu, P.R. Duderu, J. Faulkner, K. Kovitangoon, S. Kunori, S.W. Lee, T. Libeiro, I. Volobouev

Vanderbilt University, Nashville, USA

E. Appelt, A.G. Delannoy, S. Greene, A. Gurrola, W. Johns, C. Maguire, Y. Mao, A. Melo, M. Sharma, P. Sheldon, B. Snook, S. Tuo, J. Velkovska

University of Virginia, Charlottesville, USA

M.W. Arenton, S. Boutle, B. Cox, B. Francis, J. Goodell, R. Hirosky, A. Ledovskoy, H. Li, C. Lin, C. Neu, J. Wood

Wayne State University, Detroit, USA

C. Clarke, R. Harr, P.E. Karchin, C. Kottachchi Kankanamge Don, P. Lamichhane, J. Sturdy

University of Wisconsin, Madison, USA

D.A. Belknap, D. Carlsmith, M. Cepeda, S. Dasu, L. Dodd, S. Duric, E. Friis, R. Hall-Wilton, M. Herndon, A. Hervé, P. Klabbers, A. Lanaro, C. Lazaridis, A. Levine, R. Loveless, A. Mohapatra, I. Ojalvo, T. Perry, G.A. Pierro, G. Polese, I. Ross, T. Sarangi, A. Savin, W.H. Smith, D. Taylor, C. Vuosalo, N. Woods

†: Deceased

1: Also at Vienna University of Technology, Vienna, Austria

2: Also at CERN, European Organization for Nuclear Research, Geneva, Switzerland

3: Also at Institut Pluridisciplinaire Hubert Curien, Université de Strasbourg, Université de Haute Alsace Mulhouse, CNRS/IN2P3, Strasbourg, France

4: Also at National Institute of Chemical Physics and Biophysics, Tallinn, Estonia

5: Also at Skobeltsyn Institute of Nuclear Physics, Lomonosov Moscow State University, Moscow, Russia

6: Also at Universidade Estadual de Campinas, Campinas, Brazil

7: Also at Laboratoire Leprince-Ringuet, Ecole Polytechnique, IN2P3-CNRS, Palaiseau, France

8: Also at Joint Institute for Nuclear Research, Dubna, Russia

9: Also at Suez University, Suez, Egypt

10: Also at Cairo University, Cairo, Egypt

11: Also at Fayoum University, El-Fayoum, Egypt

12: Also at British University in Egypt, Cairo, Egypt

13: Now at Sultan Qaboos University, Muscat, Oman

14: Also at Université de Haute Alsace, Mulhouse, France

15: Also at Brandenburg University of Technology, Cottbus, Germany

16: Also at Institute of Nuclear Research ATOMKI, Debrecen, Hungary

17: Also at Eötvös Loránd University, Budapest, Hungary

18: Also at University of Debrecen, Debrecen, Hungary

19: Also at University of Visva-Bharati, Santiniketan, India

20: Now at King Abdulaziz University, Jeddah, Saudi Arabia

21: Also at University of Ruhuna, Matara, Sri Lanka

22: Also at Isfahan University of Technology, Isfahan, Iran

23: Also at University of Tehran, Department of Engineering Science, Tehran, Iran

24: Also at Plasma Physics Research Center, Science and Research Branch, Islamic Azad University, Tehran, Iran

25: Also at Università degli Studi di Siena, Siena, Italy

26: Also at Centre National de la Recherche Scientifique (CNRS) - IN2P3, Paris, France

27: Also at Purdue University, West Lafayette, USA

28: Also at Institute for Nuclear Research, Moscow, Russia

29: Also at St. Petersburg State Polytechnical University, St. Petersburg, Russia

30: Also at National Research Nuclear University "Moscow Engineering Physics Institute" (MEPhI), Moscow, Russia

31: Also at California Institute of Technology, Pasadena, USA

32: Also at Faculty of Physics, University of Belgrade, Belgrade, Serbia

33: Also at Facoltà Ingegneria, Università di Roma, Roma, Italy

-
- 34: Also at Scuola Normale e Sezione dell'INFN, Pisa, Italy
 - 35: Also at University of Athens, Athens, Greece
 - 36: Also at Paul Scherrer Institut, Villigen, Switzerland
 - 37: Also at Institute for Theoretical and Experimental Physics, Moscow, Russia
 - 38: Also at Albert Einstein Center for Fundamental Physics, Bern, Switzerland
 - 39: Also at Gaziosmanpasa University, Tokat, Turkey
 - 40: Also at Adiyaman University, Adiyaman, Turkey
 - 41: Also at Cag University, Mersin, Turkey
 - 42: Also at Anadolu University, Eskisehir, Turkey
 - 43: Also at Ozyegin University, Istanbul, Turkey
 - 44: Also at Izmir Institute of Technology, Izmir, Turkey
 - 45: Also at Necmettin Erbakan University, Konya, Turkey
 - 46: Also at Mimar Sinan University, Istanbul, Istanbul, Turkey
 - 47: Also at Marmara University, Istanbul, Turkey
 - 48: Also at Kafkas University, Kars, Turkey
 - 49: Also at Yildiz Technical University, Istanbul, Turkey
 - 50: Also at Rutherford Appleton Laboratory, Didcot, United Kingdom
 - 51: Also at School of Physics and Astronomy, University of Southampton, Southampton, United Kingdom
 - 52: Also at Université Paris-Sud, Orsay, France
 - 53: Also at University of Belgrade, Faculty of Physics and Vinca Institute of Nuclear Sciences, Belgrade, Serbia
 - 54: Also at Argonne National Laboratory, Argonne, USA
 - 55: Also at Erzincan University, Erzincan, Turkey
 - 56: Also at Texas A&M University at Qatar, Doha, Qatar
 - 57: Also at Kyungpook National University, Daegu, Korea